DETERMINING WATER DEPTHS FROM SURFACE IMAGES USING BOUSSINESQ EQUATIONS

by

SHUBHRA K. MISRA, ANDREW B. KENNEDY
AND JAMES T. KIRBY

THIS RESEARCH WAS SUPPORTED BY THE
OFFICE OF NAVAL RESEARCH
AWARD NO. N00014-97-1-0283

RESEARCH REPORT NO. CACR-00-01
JANUARY, 2000

CENTER FOR APPLIED COASTAL RESEARCH
OCEAN ENGINEERING LABORATORY
UNIVERSITY OF DELAWARE
NEWARK, DE 19716

TABLE OF CONTENTS

Chapter

LIST OF FIGURES

ABSTRACT

This thesis describes an algorithm developed to estimate water depths from remotely sensed images of the water surface. A one-dimensional depth inversion routine applicable to non-breaking waves is developed using extended Boussinesq equations. Using spatial maps of surface elevation lagged in time, underlying depth estimates and particle orbital velocities are obtained. Assuming the availability of only orbital velocities instead of surface elevations, a parallel inversion method is developed to calculate the bathymetry and surface elevation. In all cases, synthetic input data is used. Computations to generate input data are done using a fully nonlinear time-dependent Boussinesq model (FUNWAVE), and snapshots lagged in time are saved as discretized profiles of either surface elevations or wave orbital velocities. Wave conditions including purely monochromatic and groupy waves are simulated in the model.

A least squares method is formulated to estimate wave phase speed from the time-lagged images. Spatial correlation methods are also analyzed and their advantages and disadvantages in calculating wave celerity are discussed. Mean flow effects are included in the inversion algorithm to account for currents. For this, input data is obtained from a fully nonlinear Boussinesq model in which initial current profiles can be specified.

Calculated depths obtained using the inversion routine are compared to initial depths used to generate the synthetic images. A comparison of estimated and computed water particle kinematics is also presented. The algorithm is seen to work well for both linearized and fully nonlinear Boussinesq equations. The inversion model predicts underlying water depths for various wave conditions to reasonable accuracy. An analysis of the possible sources of errors is presented and steps for their minimization are suggested. For monochromatic waves in the presence of weak currents, the modified algorithm (including mean flow effects) is seen to make marked improvements over the original formulation. Further extension of the present inversion method to two horizontal dimensions, the inclusion of wave breaking and the effects of strong currents and validation with field data are discussed.

Chapter 1

INTRODUCTION

The nearshore region of an ocean or sea is perhaps the most dynamically active area considered in the study of hydrodynamic and other related coastal processes. Even to a casual observer on the beach, the highly chaotic nature of the wave field close to the coast is evidence enough of the complex nature of the problem. The physical variable which often dominates the cause of such variability in the observable behavior of the water surface is the water depth. The bed topography near the coast is itself always in a state of change due to an active interaction between sediment transport and hydrodynamic processes. An accurate knowledge of the ocean floor, particularly in the nearshore region and over various spatial and temporal scales, is thus very important in understanding such a complex interactive regime.

Traditional surveying methods of quantifying the depth are inherently labour intensive as they involve manual deployment of expensive instruments over the area of interest. Even with the availability of sophisticated and accurate depth measuring devices like sonic altimeters and global positioning satellite (GPS) units, the surveying process still remains costly in terms of both time and money. It is thus not feasible to use these methods to cover large spatial distances. A detailed study of the variation of the bathymetry in time is also difficult to obtain. Wave breaking and strong currents near the shore make in-situ measurements of the bathymetry a hazardous task. Moreover, marine fouling, water turbidity and suspended sediments limit the operation time scales of such instruments.

Since there already exists quite a significant amount of understanding of the hydrodynamic coupling between the water depth and the wave kinematics, methods which would determine the ocean bathymetry from remotely sensed images of the water surface are likely candidates for further development. With the progressively increasing accuracy and availability of remotely sensed radar and video images, depth inversion, as it is commonly referred to in literature, has become one of the most promising tools in this area of research.

1.1 Depth inversion

In practically all problems associated with water wave mechanics, the water depth is assumed to be a known variable. The problem statement usually involves predicting how the water mass would behave when subject to various forcing mechanisms such as gravity, surface wind stresses, etc. There exists a direct interaction between the water depth and the water particle kinematics and dynamics of the wave propagating over the particular bathymetry. Water depth is an important parameter in influencing the kinematic and dynamic behavior of a wave. Wave shoaling, refraction, diffraction and energy dissipation due to wave breaking are only some of the direct physical effects evident in a wave train as it propagates over a changing bottom. The regular or forward solution thus evaluates wave response to changes in depth, either spatial or temporal or both. A large percentage of coastal engineering problems study wave dynamics over a known or assumed bathymetry, either analytically generated or constructed from in-situ measurements. Numerous numerical models have also been developed, which require initial wave conditions and then estimate wave transformation and wave induced currents over complex topographies.

Depth inversion on the other hand does precisely the opposite task from a hydrodynamic point of view. It is assumed that information about some of the dynamics and/or kinematics of the wave is known. The problem remains to find the water depth which would have caused that particular observable disturbance in the wave field. This inversion is made possible by knowledge of the physical laws which couple the available wave data (such as wave heights, orbital velocities, phase speed etc) with the unknown depth. Several innovative depth inversion methods have been developed to evaluate bathymetry from surface wave information. These can broadly be classified into two approaches - Spatial inversion and time and frequency domain inversion.

1.2 Time and frequency domain inversion

Depth inversion in the time or frequency domain essentially involves taking time stacks of discretized surface elevation or particle velocity data, in one or two horizontal dimensions, and then inferring the unknown depth by using either some kind of physical functional dependence on one other (like the dispersion relationship) or hydrodynamic equations governing wave propagation (such as the mass conservation and momentum equations).

Very recently, Kennedy *et al.* (1999) have used a fully nonlinear time dependent Boussinesq model(FUNWAVE) as a tool for inversion. The model contains the fully nonlinear extended Boussinesq equations developed by Wei *et al.* (1995), and further modified by Kennedy *et al.* (2000) and Chen *et al.* (2000) to include the effects of wave breaking, run-up and wave-induced current effects. They assume that time lagged spatial maps of both the surface wave height and orbital velocities are available (the best case scenario in the context of data availability using remote sensing techniques) as inputs to their algorithm for inverting depth. Synthetic data comprising previous model generated outputs is used in place of remotely sensed data, such as those obtained from video or radar units. An analytic depth is used to run the FUNWAVE model with a specified initial wave climate. Since the model has a time-stepping algorithm, two snapshots of surface elevation and particle velocities, separated in time (a fraction of the input wave period) are stored. The first image is then used to initialize the inversion routine (based on the same extended Boussinesq equations as in FUNWAVE) with an assumed depth. A flat bed was used in all their test cases as the starting depth estimate. The model is then run forward in time to the time step when the second image was saved, and local phase speeds are calculated using spatial cross-correlation techniques over the entire spatial domain. The computed phase speed is compared to the true value of phase speed obtained from the given second image. Based on the phase speed mismatch between the two images, the depth is updated. Let the subscript 1 denote variables calculated for assumed depths, and m the optimal or *"true"* values obtained from the previously saved data (the second image). h and C denote the local water depth and wave celerity respectively, and g is the acceleration due to gravity. Then the relations

$$C_1 = \sqrt{gh_1} \tag{1.1}$$

$$C_m = \sqrt{gh_m} \tag{1.2}$$

give the result

$$h_m = h_1(\frac{C_m}{C_1})^2 \tag{1.3}$$

The optimal or true depth (h_m) can thus be related to the assumed depth (h_1) through the ratio of estimated (C_1) and true (C_m) phase speeds. Based on the phase speed mismatch, the depth is iteratively updated, and the final converged water depths showed good agreements with analytic depths for shallower water. For deeper water, convergence was achieved when the exponent in the ratio of phase speeds in (1.3) was raised from 2 to 4. It was pointed out by the authors that since absolute values of phase speeds are not required, but only the ratio of the two, biased correlation methods proved suitable to estimate phase speeds. Local phase speeds were obtained by subdividing the image into smaller finite windows, about 3 wavelengths in the direction of dominant wave travel. The window size was decreased when the depth iterations started to converge. Parabolic interpolation methods were utilized to determine the cross-correlation matrix peak to sub-grid accuracy. Two dimensional cubic B-splines were used to interpolate the depth across the entire domain. To remove the ambiguity in the direction of wave travel (positive and negative phase speeds), a time lag between images of a third of the wave period or less proved to work well, and stable convergence was achieved. Plane slope test cases were run in intermediate water depth range, with additional test cases comprised of the Berkhoff shoal topography and a bar and channel topography with strong currents and wave breaking on the bar and coastline. Though the bar amplitude was under-predicted, overall depths were predicted accurately. The smaller estimate of the bar amplitude was ascribed to strong wave breaking over the bar (which had been observed in their plane slope tests to be a cause for over-prediction of depth) as well as their limited spatial resolution of the bar geometry (the bar dimensions were on the order of a wavelength, compared to a window size three times that size). Wave irregularity and multi-directionality (in the shoal case) led to a decrease in accuracy.

A novel method was developed to account for possible errors in measured surface elevations or velocities (which led to the inclusion of spurious waves in the Boussinesq model). These hypothetical errors were shown to directly affect the computation of wave phase speed through cross-correlations, which in turn translated to errors in the inverse bathymetry. Based on the observation that the elevation and velocities of waves traveling in the positive x- direction have identical phase, while the phases are opposite for a wave traveling in the negative x-direction, the spurious waves were eliminated from the computations. Significant improvements were noticed in the estimated bathymetry in deeper depths when the errors were accounted for and the algorithm suitably modified.

There were several advantages to this algorithm over previous inversion methods. Current and wave breaking effects were incorporated into the inversion routine. Errors in available data were accounted for, and, as the depth inversion was done over a 2-D horizontal domain and verified to be accurate for the Berkhoff shoal case (which serves as a representative test for validating numerical wave models), it is a practical tool for inverting bathymetries over the entire surf zone. However, the assumption that both surface elevations and particle velocities be available for inversion is a possible drawback, since remotely sensed measurements of both these variables is indeed scarce as yet in either theory or practice. The model used side walls and other boundary conditions, such as a minimum depth at the on-shore end of the domain, which are not natural. Performing the fully time-dependent Boussinesq inversion was burdensome in terms of computational time.

A much simpler precursor to the above method was developed by Dalrymple *et al.* (1998), who used Hilbert transforms to estimate phase speeds from surface maps of wave elevation. Gradients of the phase structure were then calculated to determine the wave number. A big disadvantage of this method was the assumption that wave period be known accurately. The linear dispersion relationship

$$\omega^2 = gk \tanh(kh) \tag{1.4}$$

was then used to invert depth. Here, ω is the wave frequency $\omega = \frac{2\pi}{T}$, T the wave period, k is the wave number $k = \frac{2\pi}{L}$, L the wavelength, h is the local water depth and g the acceleration due to gravity.

Fourier smoothing techniques were applied to remove unnatural oscillations in the depth estimate. For spectral sea states, another method was developed using lag-correlation techniques. Using Fourier analysis of sequential images taken at short intervals of time, wave number spectra and associated phase speeds were determined. The spectrum was assumed to be constant over a spatial map approximately two peak wavelengths long. Auto-correlation and cross-correlation matrices were calculated from the images, and estimates of wavelength and phase speed were respectively obtained. The extension to two horizontal dimensions was made possible by a maximum entropy method, which used 2-D fast Fourier transforms (FFTs) to find wave number spectra. The assumed depth was iterated until the cross-correlation function from the maximum entropy function best matched the measured function. Over-predictions of depth were observed, which were accounted to nonlinearity (strong focusing effects took place behind the shoal test case) and/or window size effects on correlation estimates.

Depth inversion with nearshore field data has till now not been extensively researched, probably because of the lack of good quality and reliable remotely sensed data. There exists the difficult problem of quantifying quite a few unknown parameters which would make remotely sensed images translatable to physical variables such as water surface elevation or particle velocities. This is one of the principal reasons that most researchers have utilized synthetically constructed data to perform their depth inversions. One of the few attempts at inverting depth based on field data was done by Stockdon (1998). Video images were collected at field sites located in Duck, North Carolina and Agate beach, Oregon. Using digital video cameras, time stacks of pixel intensities at various cross-shore and long-shore arrays were stored. A linear Modulation Transfer Function (MTF) was used to provide spectral representations of relative amplitudes and phase information between the input signal and the output. In the frequency domain,

$$G(f) = M(f)X(f) \tag{1.5}$$

where $X(f)$ is the input signal and $G(f)$ is the output, related by the linear transfer function $M(f)$, and f denotes the frequency component of the signal. After collecting the pixel intensity time series over a single cross-shore array and multiple long-shore arrays, smoothing was done with high pass (to get rid of low frequency information) and low pass (to remove noise) filters. An average spectrum was calculated over all the cross-shore locations. The spectral peak of this average spectrum then indicated the incident frequency with a prescribed frequency band width to represent incoming waves. The spectral peak was calculated as

$$f_{cm} = \frac{\sum_i S_i f_i}{\sum_i S_i} \tag{1.6}$$

where the subscript cm denotes the center of mass of the spectrum and i the individual frequency component. The cross-shore wave number was then estimated using a complex empirical orthogonal function (CEOF) analysis of data collected from the cross-shore arrays. The phase function and the amplitudes were determined in terms of the eigenvalues of the cross-spectral matrix. The first mode or complex eigenvector (which represents the majority of the data variability) is given as

$$\Lambda = a(x) + ib(x) \tag{1.7}$$

where i is the imaginary number $i = \sqrt{-1}$. The phase $\Theta(x)$ and the amplitude $A(x)$ are then given at each cross-shore pixel location by

$$A(x) = \sqrt{a(x)^2 + b(x)^2} \tag{1.8}$$

$$\Theta(x) = \tan^{-1} \frac{b(x)}{a(x)} \tag{1.9}$$

The cross-shore component of the wavenumber $k(x)$, is then given by

$$k(x) = \frac{d\Theta}{dx} \tag{1.10}$$

Once the wave number and frequency have been obtained, the linear dispersion relationship was used to invert the depth. Depths were significantly over-predicted in shallow water and under-predicted in deep water. The errors were ascribed to the simple shallow water formulation of phase speed (which neglected frequency and amplitude dispersion effects), and the analysis of the video signal or the subsequent phase speed extraction (neglecting the effects of surface drift currents, the undertow and rip currents).

Radar images of the ocean surface have also interested researchers as feasible data to invert the bathymetry. Synthetic Aperture Radar (SAR), Interferometric SAR (INSAR) and X-Band radars can provide high-resolution images, which have been used to extract wave information such as wave phase speeds. Dugan *et al.* (1996) have used airborne imaging systems to collect sequential ocean surface maps, and, using 3-D frequency-wavenumber spectra and the linear dispersion relation, have inverted depth. Bell (1999) has demonstrated the usefulness of a sequence of marine X-band radar images to invert shallow water bathymetry (the radar provided 144 seconds of data from 64 images, with a time interval of 2.25 seconds). The inversion algorithm he used is essentially the linear dispersion relationship, with the phase speed and the time period estimated from cross-correlation and frequency spectra analysis respectively. A slight modification to the wave celerity calculation was the inclusion of the whole time stack of images instead of just a single pair. Detailed comparisons between true and estimated depths could not be made because of lack of independent depth data. Due to possible ambiguities in the determination of the frequency and cross-correlation peaks, the implementation of a simplified inversion algorithm and the neglect of mean flow and nonlinear effects, the inversion results were only qualitatively representative of the true bathymetry.

1.3 Spatial inversion

Linear inversion techniques though simple in implementation have severe disadvantages in their application to shallow water regions. Amplitude dispersion effects and nonlinear wave properties modify the wave characteristics significantly as the waves shoal on entering shallower depths. Grilli (1998) devised two depth inversion algorithms (DIAs) to include amplitude and frequency dispersion effects in shallow water, when estimating depth from remotely sensed data. His computations were done on a fully nonlinear model based on potential flow theory and the boundary element method. The properties of shoaling periodic regular waves on monotonic and mildly sloping beach profiles were investigated and their properties used to invert depth. The inversion was thus in one horizontal dimension and the waves were assumed to be long-crested in the long-shore direction, the x-axis being the cross-shore direction. Each individual crest and trough of a shoaling wave was independently identified and tracked in space in time. Envelopes of wave height, $H(x)$ were thus obtained. The phase speed distribution over the domain was estimated from

$$C(x) = \frac{dx_c(t)}{dt} \tag{1.11}$$

where $x_c(t)$ is the instantaneous crest location for the particular wave. A mean wavelength was also calculated geometrically by averaging over the crest to crest wavelength $L_c(x)$ and the wavelength measured between successive troughs $L_t(x)$.

$$L(x) = \frac{L_c(x) + L_t(x)}{2} \tag{1.12}$$

Once wave celerity and wavelength are known, the time period (T) of the wave is calculated ($T = \frac{L(x)}{C(x)}$). Data from previous model runs was used to relate the wave celerity at an unknown depth to deep water wave characteristics involving empirically determined coefficients. Linear wave theory was used to interpolate the empirical relation for small incident wave steepness and shallower depths. These are then solved iteratively till the wave heights and the depths converge to some predetermined criterion.

A modified algorithm was developed for the case where only phase information was available and no surface elevation data was given. Using empirically fitted experimental data, a relationship between wave asymmetry (calculated from wave steepness), wave period and water depth is determined. This is then inverted through previously calculated wave period values, and an assumed depth is iterated till convergence is obtained. The estimated values of phase speed and water depths showed improvements over computed values from linear dispersion theory. Root mean square (RMS) errors for depth prediction were on the order of 1.7 - 3.6 % for the first algorithm and 2.1 - 5.7% for the second. These were significantly less than the linear theory results, which had RMS errors (14.6 - 20.5%) an order of magnitude higher.

There are disadvantages in such an inversion method, the primary one being the assumption of a monotonic and mildly varying slope. Bars and troughs are a common feature of interest close to the shoreline. The inability of the above method to account for such changes in topography places a limitation in its area of application. All test cases were done with periodic waves, where it was possible to geometrically determine the wave period. This would prove to be difficult for the case of groupy or random waves, in which several frequencies would be represented in one wave form, as is the case in the real sea state. Waves were only analyzed up to the breaking point and hence the inversion would be limited to the breaker line close to the shore and not inside the surf zone. The marked improvements over linear inversion predictions by the inclusion of nonlinear effects, however, demonstrate that any approach to depth inversion should inherently take into the complex nonlinear dynamics of wave propagation.

Chapter 2

PHASE SPEED ESTIMATION

Most of the depth inversion methods developed till date involve the calculation of the wave celerity from available information about either the phase structure or the kinematics of the wave. As can be seen from the dispersion relationship (1.4), the phase speed is a direct representation of the water depth. If linear and nonlinear amplitude dispersion effects are neglected, it is readily apparent from the shallow water approximation of the dispersion relation

$$C = \sqrt{gh} \tag{2.1}$$

that waves slow down with decreasing depth. The change in phase speed over space thus quantifies a corresponding change in depth. Measuring wave phase speeds has thus been historically the first and basic step towards inverting water depths. Fuchs (1953) devised a simple technique to measure the speed of a traveling water wave, by estimating visually the time taken for an identifiable feature on the wave train (e.g the wave crest) to cross a certain fixed distance. Similar methods were applied in airborne imaging of the sea surface to determine the celerity. Since then, more sophisticated in-situ tools and remote sensing techniques have been employed. Using cross-spectra data from spatially separated wave gauges perpendicular to the beach, Thornton and Guza (1982) developed an estimate of the cross-shore component of the phase speed as

$$C_x = \frac{2\pi f \delta x}{\phi(f)} \tag{2.2}$$

where δx is the spatial separation between the gauges, f is the frequency and $\phi(f)$ the cross-spectral value at that particular frequency.

Using video images of the surf zone in the field, Lippmann and Holman (1991) devised a method to estimate phase speeds of breaking waves. Using spatially separated pixel intensity time series, wave speeds and wave directionality were obtained by calculating the time it took for the wave to travel the distance between the two pixel locations. In the frequency domain, (2.2) was used to calculate the cross-shore phase speed. They hypothesized that this point calculation of celerity could be extended to required cross-shore distances by considering arrays of pixel locations. From a more recent and sophisticated data acquisition point of view, Dugan *et al.* (1996) used data collected from an airborne infrared system to estimate the ocean wave dispersion surface. Phase speeds were calculated from the 3-D frequency-wave number spectra constructed from the aerial snapshots of the water surface. Recently, several other simple but innovative techniques have been developed to estimate the local wave celerity from surface images.

2.1 Spatial correlations

In the video-based phase speed estimation discussed above, it is required that long time series of pixel intensity be available. It is certainly possible and easy to acquire such data when using a video camera, since automated cameras mounted on towers and focussed on the region of interest can be made to run for as long as desired and thereby provide continuous time stacks of images or pixel intensity. Airborne systems on the other hand can collect only snapshots of the water surface spaced in time, though radar units are capable of sampling the water surface at discrete but closely spaced time intervals. For spatially dense images separated in time (usually a fraction of a wave period), correlation formulas can be used to calculate local phase speed over the entire domain.

The spatial cross-correlation functions between two distinct stationary random processes $f(x)$ & $g(x)$ are defined as

$$R_{fg}(\xi) = E[f(x)g(x+\xi)] \tag{2.3}$$

$$R_{gf}(\xi) = E[g(x)f(x+\xi)] \tag{2.4}$$

where ξ is the *lag* between the two processes, and E denotes the *Expected value* or the *Statistical expectation of* and is defined as

$$E[f(x)] = \int_{-\infty}^{\infty} fp(f)df \tag{2.5}$$

$p(f)$ being the *probability density function* of $f(x)$. For stationary processes $f(x)$ and $g(x)$,

$$R_{fg}(\xi) = R_{gf}(-\xi) \tag{2.6}$$

but in general, R_{fg} & R_{gf} are not the same, and unlike the autocorrelation function, are not even in ξ. These integral correlation functions must be estimated using summations because only a finite length of data is available in discrete form in practice. An unbiased cross-correlation between two discrete finite vectors f and g whose length in space is N can be written as

$$R_{fg}(m) = \frac{1}{N-|m|} \sum_{n=0}^{N-|m|-1} f(n)g^*(n+m) \tag{2.7}$$

where m and n vary from 0 to N and are termed the spatial lags. The cross-correlation matrix is $2N+1$ in length, since it is calculated for positive (1 to $+N$), negative (-1 to $-N$) and zero lag. The phase speed is calculated by first identifying the lag at which the maximum or peak value occurs in the correlation matrix. The peak cross-correlation value can be thought of as the maximum overlap between

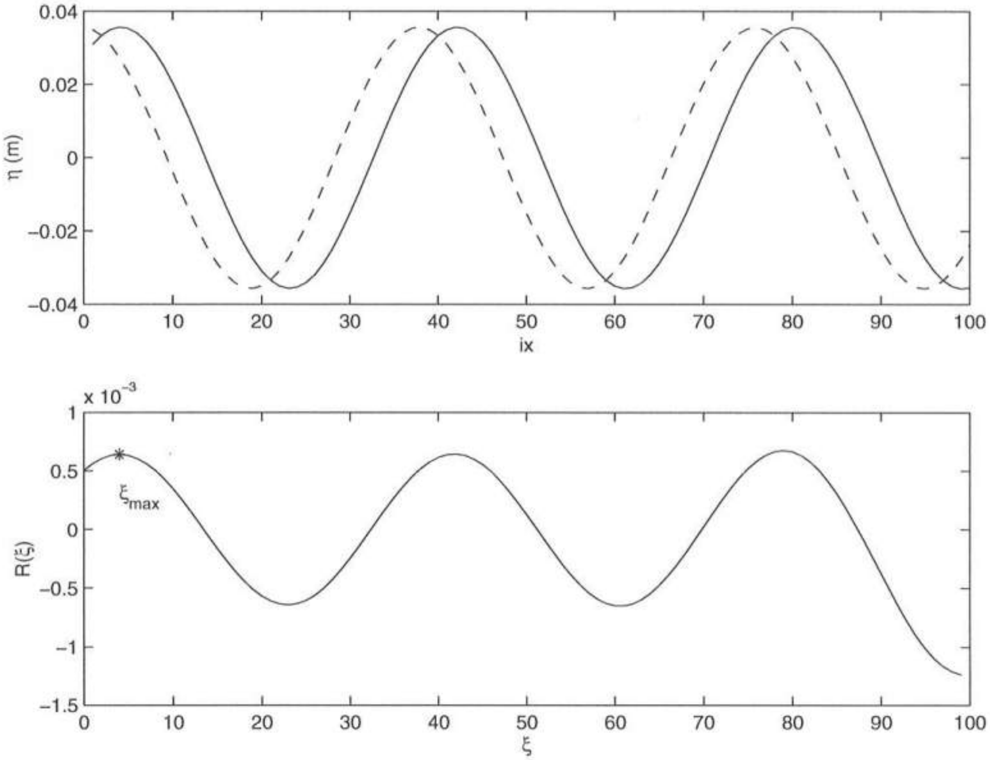

Figure 2.1: Top: Wave surface snapshots lagged in time. Bottom: Cross-correlation vector $R(\xi)$ calculated at varying spatial lags (ξ).

the two images when the two signals are slid over each other. When considered in the context of a moving waveform, the lag where the peak occurs (ξ_{max}) simply means the distance the wave has moved during the time interval separating the two snapshots (δt). The phase speed is then given by

$$C = \frac{\xi_{max}}{\delta t} \tag{2.8}$$

where both ξ_{max} and δt have been converted to physical units of distance and time respectively.

Figure 2.1 shows an example calculation of phase speed from two given images using spatial cross-correlations. The dashed and solid lines in the top panel are the surface elevation snapshots (the dashed line being the first image) of a propagating wave with an analytic phase speed $C_{exact} = 2m/s$, separated by a time interval $\delta t = 0.5s$. In the bottom panel is plotted the cross-correlation vector $R(\xi)$ against the spatial lag ξ. It should be noted that only half of the correlation vector (calculated at positive lags) has been plotted, since it is known that the wave is propagating in the positive $x-$ direction. The lag at the first cross-correlation peak (ξ_{max}) has been marked as an asterisk and $\xi_{max} = 4$. Since the x-grid spacing was 0.25m, in physical distance units, $\xi_{max} = 4 \text{ x } 0.25 = 1m$. The phase speed as calculated from (2.8) is thus $C_{est} = 2.0\text{m/s}$ which agrees with the analytic phase speed.

There are two conflicting requirements one faces while evaluating the phase speeds at discretized positions in the spatial domain using correlation functions. Ideally, one would get speed estimates at every point in the domain where surface data is available. This would provide the best spatial resolution and indication of changes in celerity over space. Cross-correlation calculations (because of the need for computational efficiency) inherently require the use of fast Fourier transforms (FFTs). The accuracy of Fourier transforms are directly proportional to the data length. A periodic data set or an infinitely long (which can be assumed to have an infinite period) record would recover the analytic result because of the harmonic nature of the Fourier expansion. Given two finite surface signals however, the aim is thus to determine the phase speed at closely spaced intervals in space, the separation being small enough to resolve spatial variations and large enough to get reasonable estimates from the cross-correlation vectors. The entire data is typically windowed by subdividing the entire domain using finite windows of length W. The window is shifted over the domain in small spatial shifts (ws) to get local estimates. The cross-correlation function for a given window is then given by

$$R_{fg}(\xi) = \frac{1}{W-\xi}\int_0^{W-\xi} f(x)g(x+\xi)dx \tag{2.9}$$

The effect of a finite window size on the phase speed estimate can be seen analytically by considering, for simplicity, two sinusoidal one-dimensional propagating waves slightly differing in their phases (which can be interpreted as two snapshots of a single waveform lagged in time by an amount δt). Let the two signals be : $f(x) = a\cos(kx), g(x) = a\cos(kx - \omega\delta t)$. The phase lag between the two images is thus $\omega\delta t$. The definition of the cross-correlation function is

$$\begin{aligned} R_{fg}(\xi) &= \frac{1}{W-\xi}\int_0^{W-\xi} a^2\cos(kx)\cos[k(x+\xi)-\omega\delta t] \\ &= \frac{a^2}{2(W-\xi)}[\frac{\sin(2kW-\omega\delta t-k\xi)+\sin(\omega\delta t-k\xi)}{2k} \\ &+ (W-\xi)\cos(\omega\delta t-k\xi)] \end{aligned} \tag{2.10}$$

To identify the lag at the cross-correlation peak (the maximum value of the cross-correlation vector), we differentiate $R_{fg}(\xi)$ with respect to the spatial lag ξ and equate it to zero.

This gives

$$\begin{aligned} \frac{dR_{fg}(\xi)}{d\xi} &= 0 \\ &= \frac{-k(W-\xi)\cos(2kW-\omega\delta t-k\xi)+\sin(2kW-\omega\delta t-k\xi)}{2k(W-\xi)^2} \\ &- \frac{k(W-\xi)\cos(\omega\delta t-k\xi)+\sin(\omega\delta t-k\xi)}{2k(W-\xi)^2} \\ &+ k\sin(\omega\delta t-k\xi) \end{aligned} \tag{2.11}$$

Let the lag at the peak be $\xi = \xi_{max}$ which can be obtained from the definition of the maximum spatial lag

$$C = \frac{\omega}{k} = \frac{\xi_{max}}{\delta t} \tag{2.12}$$

If we now substitute for $\xi = \xi_{max}$ in (2.11), we get

$$W = L[\frac{\delta t}{T} + \frac{(2n+1)}{4}] \tag{2.13}$$

where n is any integer. Choosing a window size and the other parameters given by (2.13), we would recover the exact analytic phase speed of the wave form. The expression (2.13), however, shows that, even for two perfectly sinusoidal signals, the window size is dependent upon the wavelength, the time-lag between the two signals, the time period of the wave and the integer n. This is an unfortunate result when applied to phase speed determination from two surface images for a variety of reasons. The wavelength and the wave period are not known a priori. Real surface images also will never contain purely monochromatic waves, and thus no unique period or length of the wave-train can be determined, even if methods be available to estimate the two. The determination of wavelengths from surface signals by auto-correlation functions runs into the same problem of choosing a window size, which in turn depends on the wavelength. The analytic results shown above were computed numerically for a sine and cosine wave form with a wave period $T = 8s$ and wave length $L = 40m$, which gives the true phase speed as $C_{exact} = 5.0m/s$. Two snapshots for each waveform were taken with a time interval $\delta t = \frac{T}{8} = 1$s. The spatial grid resolution was $dx = 1m$, which meant there were 40 points in a wavelength. The results for the estimated phase speed (C_{est}) for various window sizes (W) is shown in Figure 2.2.

The estimated celerities (the solid and dashed lines) plotted in Figure 2.2 have been determined from the correlation matrices to sub-grid accuracy by an analytic parabolic interpolation around the peak. The smallest window size shown here is slightly larger than the wavelength. Window sizes smaller than the wavelength have been seen to result in large errors, though theoretically W can be made as small as desired. The calculated phase speed recovers the true value only at window sizes defined by (2.13), which are plotted as *. The error for a window size which is twice the wave length ($W = 2L$) is approximately 10 %, with the error decreasing as the window size increases. The sine and cosine wave forms if taken together

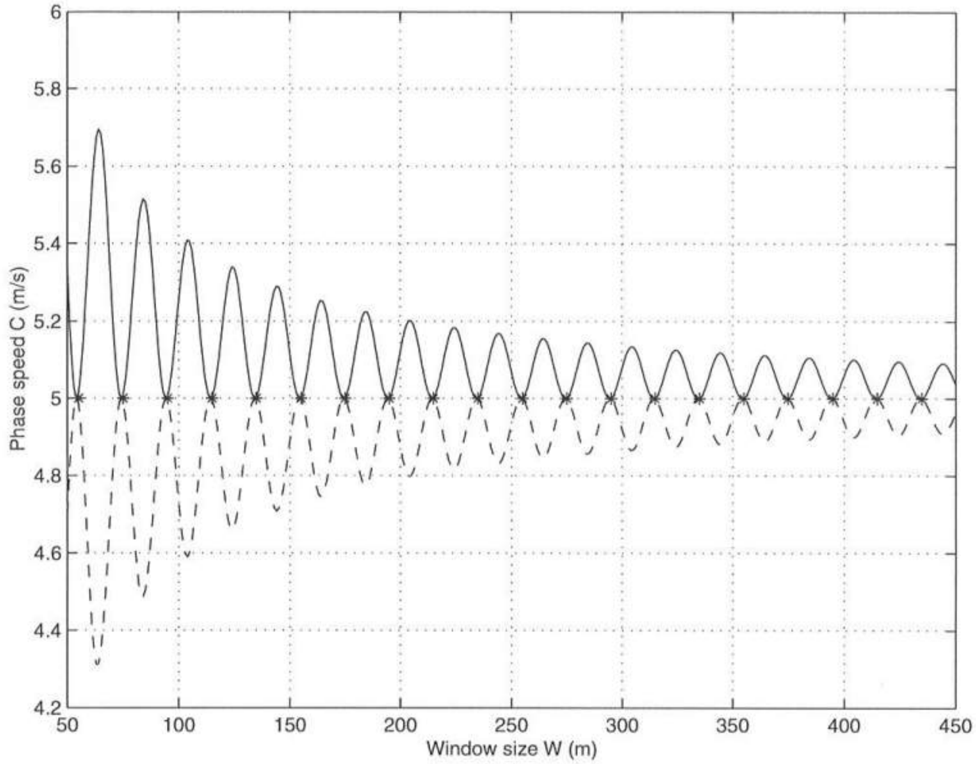

Figure 2.2: Effect of window size on estimation of phase speed by cross-correlation method. Solid line : Estimated phase speed (C_{est}) for a sine wave signal, Dashed line : Estimated phase speed (C_{est}) for a cosine wave signal, * : Analytically determined window sizes for $n = 2$, $n = 3$,..., $n = 21$ from (2.13)

would average out their respective errors. Spatial cross-correlations have been used by Kennedy *et al.* (1999) in two horizontal dimensions to calculate wave directionality and phase speeds, and good agreements have been reported for irregular wave conditions.

Figure 2.3 shows example calculations for a monochromatic wave ($H = 0.05m, T = 4.369s$) propagating over a plane slope (slope = 1:30). The top panel shows two snapshots of surface elevation at a time-lag of $\delta t = 0.5s$, the dashed line

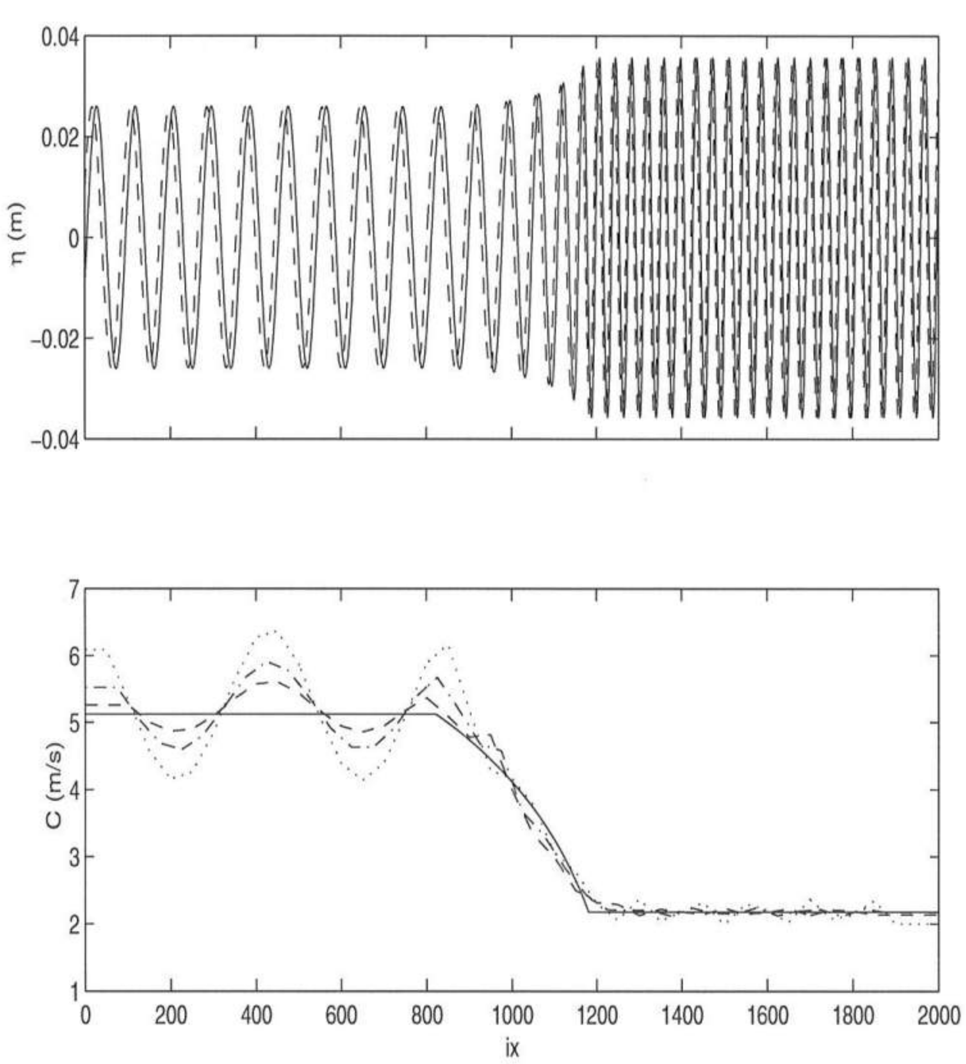

Figure 2.3: Estimation of phase speed by cross-correlations for a wave propagating over a plane slope. Top: Surface images, Bottom: Analytic (-) and estimated phase speeds for window sizes $W_1 = 25m$ (.), $W_2 = 37.5m$ (-.) $W_3 = 50m$ (- -)

being the first image in time. The surface images are obtained from the Boussinesq model FUNWAVE by solving linearized versions of Nwogu's equations (See Wei *et al.* (1995) for a detailed description). The model grid spacings were $dx = 0.25m$ and $dt = 0.02s$. The deep water depth was $3.5m$ ($kh = 0.98$) and the shallow region was $0.5m$ ($kh = 0.33$). The waves were thus propagating in intermediate water depth. The images were collected at a time spacing $\delta t = 2.0s$. The window size for the cross-correlation method was arbitrarily chosen at $W_1 = 25m$. In terms of numerical grid points (shown as ix in Figure 2.3) the size of the window W_1 extends from ix to $ix+100$. The dash-dot line is $W_2 = 37.5m$ (ix to $ix+150$) and the dashed line is $W_3 = 50m$ (ix to $ix + 200$). The deep water wavelength was $L_0 = 22.43m$ and in shallow water the wavelength was $L_{sh} = 9.50m$. The window shift for all the windows was constant at 12.5m. Linear interpolation was done to evaluate the phase speed at every point in the domain. The cross-correlation estimates are compared to the analytic phase speed (the solid line). To calculate the analytic phase speed for the given bathymetry, Nwogu's linear dispersion relation was used.

$$C^2 = gh[\frac{1 - (\alpha + (1/3))(kh)^2}{1 - \alpha(kh)^2}] \tag{2.14}$$

where $\alpha = 0.39$.

In the shallower depths, where the wavelength decreases and the wave slows down, the phase speed estimates are reasonably accurate irrespective of window size. This is because at that depth, even the smallest window ($W_1 = 25m$) is almost three times the wavelength ($L_{sh} = 9.50m$). As was shown earlier, the absolute error in the estimate phase speed decreases with an increasing window size. Another reason for smaller errors in the shallower depths is that the wave phase speed in shallow water is independent of wavelength and is only a function of the local depth (2.1). The dependence of window size on wavelength thus becomes less and less important as the wave propagates into shallower water. In deeper water, it can be seen that as the window size increases, the error in the cross-correlation estimate of phase speed also decreases, but still is relatively much larger than in shallower water. The stronger dependence of the window size on the wavelength in the deeper region is also obvious from the large oscillations in the estimated phase speed.

2.2 Least squares estimation

To avoid the pitfalls mentioned in the previous method, a simple least squares based method was developed to calculate phase speeds from two time lagged surface images. Let η_1 and η_2 be the given images. If the waveform is a perfect sinusoid, the spatial shift which would minimize the error between the two images, divided by the time-lag, would then give us the phase speed of the entire wave. Since real ocean surface data consists of multiple waves with different frequencies, propagating over a changing topography, local phase speeds have to be estimated.

We use finite windows as before to subsample the given image. Being based upon purely geometric arguments, the window size does not depend on any of the as yet undetermined wave parameters like the wavelength or time period. The only concerns are spatial resolution (which would decrease with increasing W) and providing enough wave information within the window. The problem of a loss in spatial resolution arising from a large window size can only be minimized by sacrificing wave information within the window, as would be the case for a window size smaller than the local wavelength.

Figure 2.4 (top) shows the wave images (for a purely sinusoidal propagating wave) considered before for the cross-correlation case, with all parameters remaining the same. The bottom plot shows the least square error plotted against the spatial lags (which determine the overlap between the two images). Let η_3 and η_4 be the windowed data from the two images η_1 and η_2, and each be W grid points in length. In physical distance, the window size is therefore $(W-1)dx$, where the grid spacing

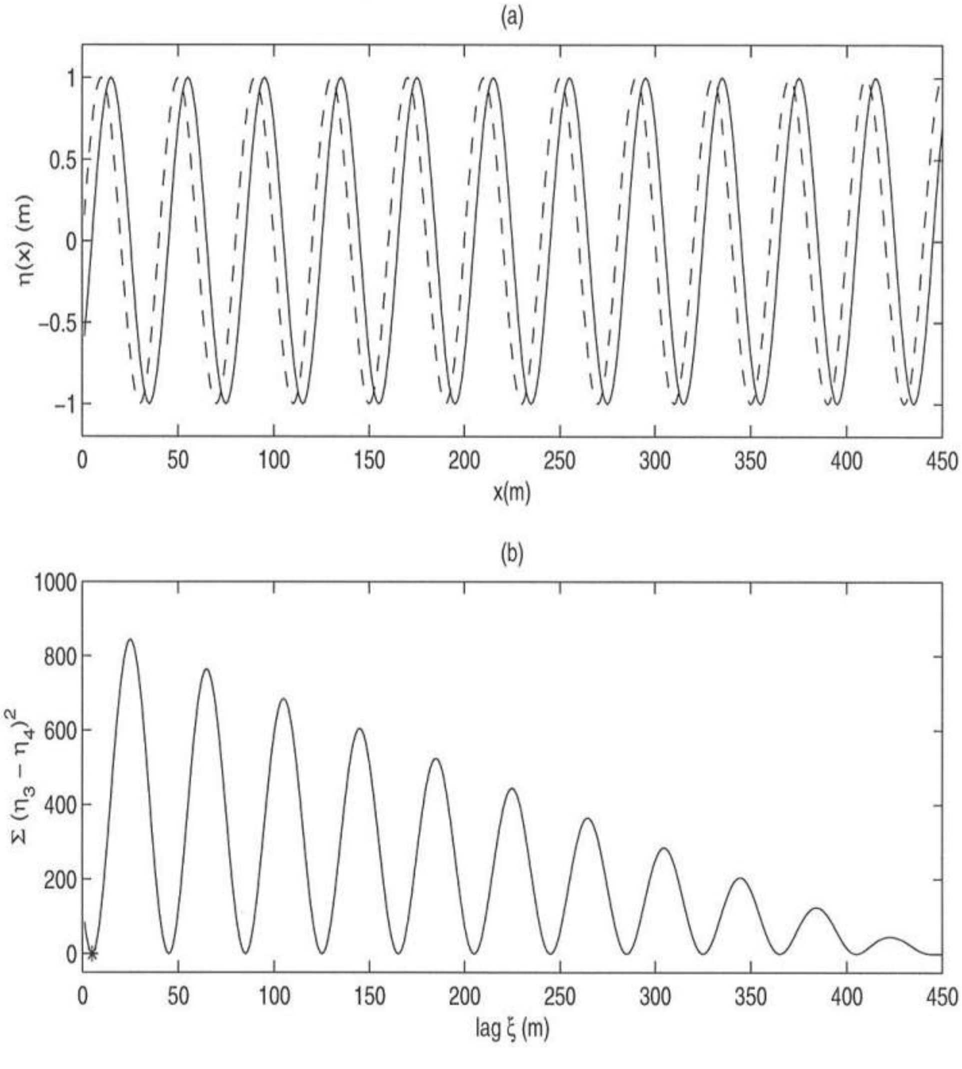

Figure 2.4: Top: Spatial maps of surface elevation separated in time. Bottom: Least squares error between the two images as a function of spatial lag.

dx is in physical units of distance. The least squares error at a spatial lag ξ is defined as

$$Err(\xi) = \sum[(\eta_3(1:W-\xi))^2 - (\eta_4(1+\xi:W))^2] \tag{2.15}$$

The error can be seen to trail off as the lags increase, since less and less of the two images is available for comparison. As the spatial lags increase, the amount of wave information for the two images also decreases. The first minimum in the error vector is marked as a * in the plot, which occurs at a lag ξ_{min}= 5. Since the time lag between the two images (δt) is 1 sec, and the spatial resolution (dx) equal to 1 m the phase speed calculated from (2.16)

$$C = \frac{(\xi_{min} dx)}{\delta t} \tag{2.16}$$

is 5.0 m/s, which agrees with the analytic phase speed. ξ_{min} has been multiplied here by dx to convert the numerical grid position for the minimum lag to a physical distance.

The effect of window size on celerity calculations using least squares is plotted in Figure 2.5. Considering the same wave parameters and images as in the cross-correlation case, the analytic phase speed (solid line) is plotted along with the estimated speed (dashed line) for various window sizes. It is to be noted that the window size plotted along the x-axis is a physical quantity. It is essentially the same as in (2.15), since here $dx = 1.0$. The error can be observed to decrease as W increases, with the maximum error at the smallest window size about 0.2 % which is almost two orders of magnitude smaller than that for the cross-correlation method for the same window size. The oscillations in the least squares error as well as the estimated phase speed are due to the strictly periodic nature of the input signal, but are not a cause for major concern since the amplitude of the oscillations are small and within acceptable error margins.

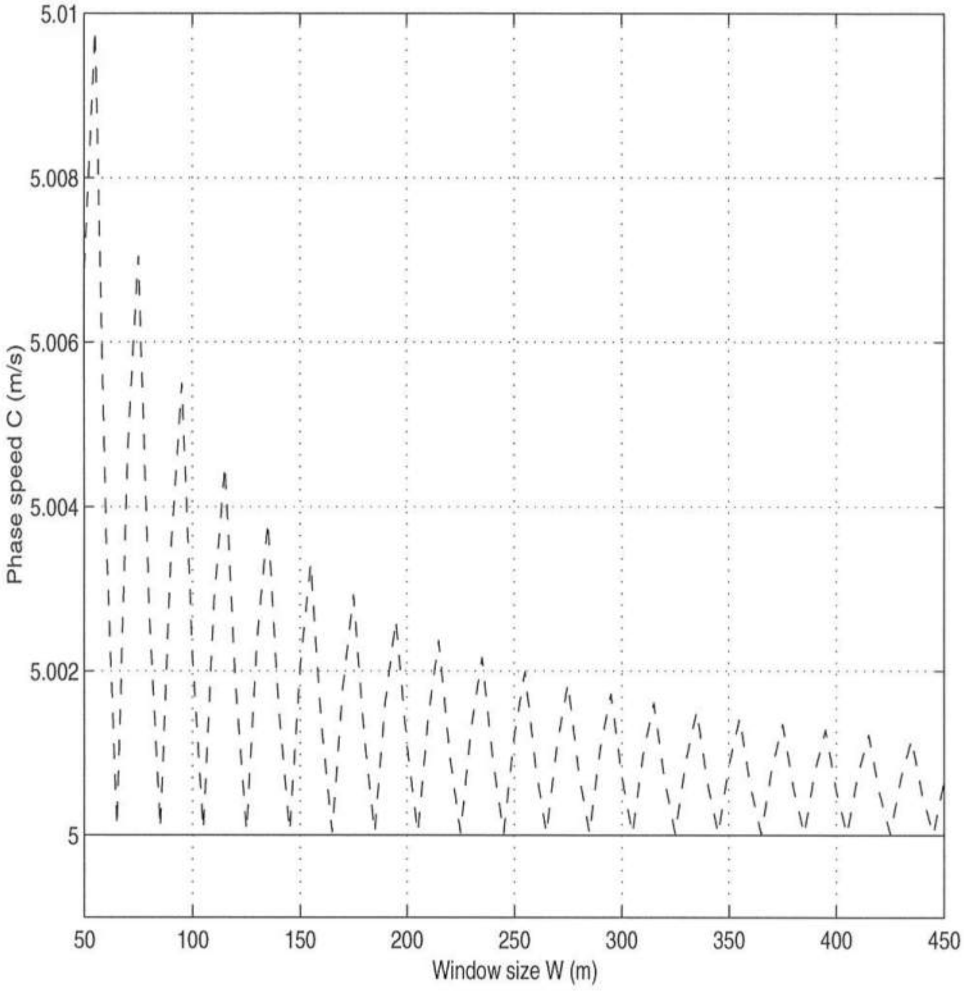

Figure 2.5: Effect of window size on estimation of phase speed by least squares method. Analytic phase speed (–), Least squares estimate of phase speed (- -)

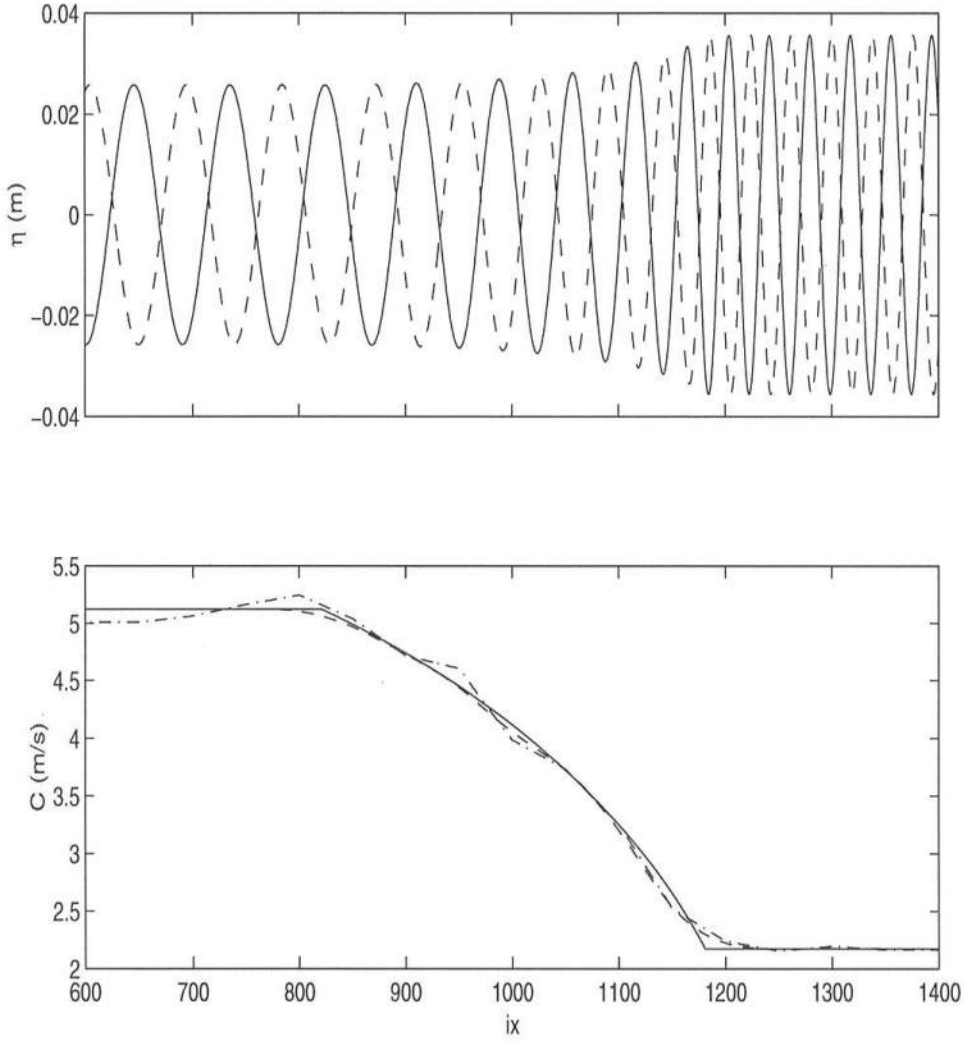

Figure 2.6: Top: Wave surface snapshots generated in FUNWAVE with linearized equations. Bottom: Comparison of linear analytic (-) and estimated phase speeds : Cross-correlation(-.), Least squares(- -). $W = 25m$

To compare the phase speeds obtained by the cross-correlation and least square method, calculations were done for the plane slope test case discussed in section 2.1 with the wave and model parameters remaining the same. The dashed line in the top panel of Figure 2.6 shows the first image and the solid line the second image recorded after a time interval $\delta t = 2.0s$. The images are the same as in Figure 2.3 (top panel), but are truncated here on either side of the slope to show a more detailed comparison of the true and estimated phase speeds. In the bottom panel are plotted the cross-correlation phase speed estimate (the dash-dot line), the least squares estimate (the dashed line), and the linear analytic phase speed (solid line). The window size for both estimates was $W = 25m$, and the window shift was 12.5m. The analytic phase speed is predicted accurately by the least squares method (the dashed line is almost indistinguishable from the solid line) except at sharp changes in bathymetry (the land-ward and seaward toes of the slope), where the large and finite window size smears the corresponding sharp change in phase speed. Linear interpolation is used through the rest of this study based on the ease and simplicity of implementation and the reasonable accuracy of results. The cross-correlation estimate as is expected, shows larger errors in the deeper depths.

Figure 2.7 shows the phase speed estimated by the least squares method for the same wave, but from velocity data instead of surface elevation data. As a comparison both the estimated phase speeds are plotted along with the analytic speed. There is hardly any difference between the two estimates. Spatial maps of either surface elevation or particle velocity data could thus be used to predict the celerity variation in space.

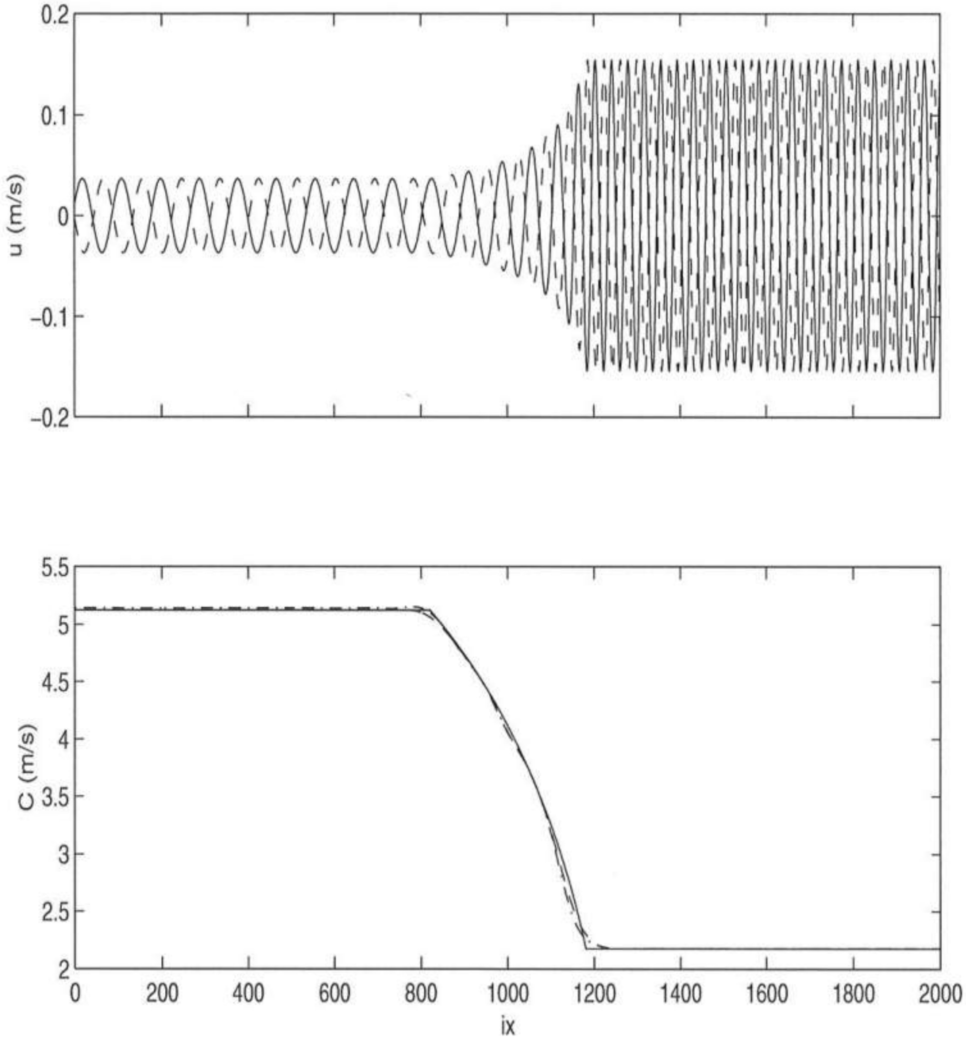

Figure 2.7: Top: Snapshots of particle velocities generated in FUNWAVE using linearized equations. Bottom: Comparison of linear analytic(-) and estimated phase speeds - From surface elevation data (- -), From particle velocity data (-.)

Chapter 3

MATHEMATICAL FORMULATION

Linear or Airy wave theory, in describing wave propagation, is severely restricted to a very narrow of wave conditions. The linear approximation states that the ratio of wave height (H) to wavelength (L), the wave steepness parameter or the wave slope ($\epsilon = ka$) be small, i.e, $\epsilon << 1$, where a is the wave amplitude and k is the wavenumber ($k = \frac{2\pi}{L}$). Small amplitude waves are also characterized by the relative wave height ($\delta = a/h$) where h is the local water depth. Waves with $\epsilon << 1$ and $\delta << 1$ are thus called small amplitude or linear waves. When ϵ or $\delta \sim O(1)$, the waves are called nonlinear waves owing to the large value of the scaled wave amplitude. It is known that as waves approach from deeper water onto shallower depths, the wave height increases in accordance with the decreasing water depth. This phenomenon is known as shoaling and is derived from energy conservation principles and geometric arguments (Snell's law). Linear shoaling theory however, significantly under-predicts the wave heights close to the beach.

As wave nonlinearity increases, and the limits of linear approximation are crossed, large and unnatural discrepancies begin to show up between observations and theory. These errors are because linear theory does not include the generation of higher harmonics associated with the fundamental wave, and which change the shoaling wave profile, giving it sharper peaks and broader troughs. There are several other nonlinear phenomena which cannot even be predicted by linear wave theory. In the deep ocean on the other hand, where wave elevations are very small compared to their length, Airy theory provides a simple and reasonably accurate theory to model various wave properties. To extend the range of applicability beyond the linear limit, different wave theories have been developed by researchers, each having its own share of advantages and disadvantages, but all of which have their own domain of validity to within accepted levels of accuracy.

Two such wave theories or approximations to the exact solution of the water wave boundary value problem, are the shallow water wave theory and the Boussinesq equations. Since an accurate knowledge of depth is relatively of more importance in the shallow water regime, where the bottom topography undergoes frequent and large scale transformations, the depth inversion algorithms developed here are based on the above two wave theories. The shallow water equations, owing to their simplicity are investigated first and the methodology extended to the more widely applicable extended Boussinesq equations.

In the present inversion method, it is assumed that two surface images (either spatial maps of surface elevation or particle velocity) lagged in time are given. All computations are done in one horizontal dimension (the x direction). The images are obtained from time-dependent models where discrete time stepping allows for the storage of spatially dense images of elevation or velocities at separate instances of time. The inversion model however requires the available hydrodynamic information to be dense in space and not in time. The linearized wave equation is used to replace all the time derivatives in the model equations by spatial derivatives, and hence arrive at what will be called the time independent depth inversion equations.

3.1 Wave equation

The linearized frictionless long wave equations of motion are given by

$$\frac{\partial u}{\partial t} = -g\frac{\partial \eta}{\partial x} \tag{3.1}$$

$$\frac{\partial v}{\partial t} = -g\frac{\partial \eta}{\partial y} \tag{3.2}$$

For a horizontal bottom, upon cross-differentiating the above to eliminate u and v, we arrive at the second order wave equation

$$C^2(\frac{\partial^2 \eta}{\partial x^2} + \frac{\partial^2 \eta}{\partial y^2}) = \frac{\partial^2 \eta}{\partial t^2} \tag{3.3}$$

where $C = \sqrt{gh}$ is the shallow water phase speed.

For a periodic progressive wave form traveling in the positive $x-$ direction, $\eta = a\cos(kx - \omega t)$

$$\frac{\partial \eta}{\partial t} = \omega a \sin(kx - \omega t) = -\frac{\omega}{k}\frac{\partial \eta}{\partial x} = -C\frac{\partial \eta}{\partial x} \tag{3.4}$$

The wavenumber k and the frequency ω are implicitly assumed to be independent of space (x) and time (t) respectively. This essentially states that the change in position, in time, of a particle on the wave is equivalent to its spatial change in a frame of reference moving with the speed of the wave. The functional dependency is called the first order wave equation. Similarly, for a wave traveling in the negative $x-$ direction, $\eta = a\cos(kx + \omega t)$, the wave equation is

$$\frac{\partial \eta}{\partial t} = -\omega a \sin(kx + \omega t) = \frac{\omega}{k}\frac{\partial \eta}{\partial x} = C\frac{\partial \eta}{\partial x} \tag{3.5}$$

The first and second order wave equations are used to transform the time-dependent governing equations into the time-independent depth inversion equations to be used in the depth inversion algorithm by replacing the time derivatives with the spatial derivatives ($\frac{\partial}{\partial t} \longrightarrow C\frac{\partial}{\partial x}, \frac{\partial^2}{\partial t^2} \longrightarrow C^2\frac{\partial^2}{\partial x^2}$)

3.2 Linearized shallow water equations

In one horizontal dimension ($x-$ direction), the linearized continuity equation or the mass equation is given as

$$\frac{\partial \eta}{\partial t} + \frac{\partial (hu)}{\partial x} = 0 \tag{3.6}$$

The momentum equation is

$$\frac{\partial u}{\partial t} + g\frac{\partial \eta}{\partial x} = 0 \tag{3.7}$$

If we consider the wave to be propagating in the positive $x-$ direction, using (3.4) we can replace the time derivatives with the spatial derivatives and arrive at the shallow water depth inversion mass and momentum equations

$$-C\frac{\partial \eta}{\partial x} + \frac{\partial (hu)}{\partial x} = 0 \tag{3.8}$$

$$-C\frac{\partial u}{\partial x} + g\frac{\partial \eta}{\partial x} = 0 \tag{3.9}$$

If we now integrate along $x-$ (assuming that C is locally constant, i.e $\frac{\partial C}{\partial x} = 0$) we get,

$$-C\eta + hu = A \tag{3.10}$$

$$-Cu + g\eta = B \tag{3.11}$$

where A and B are arbitrary integration constants. If we consider pure wave propagation without mean flow effects, then $A = B = 0$, since motion vanishes in the absence of a wave. The case of non-zero values of the constants are discussed later in section 3.5, where depth-uniform steady currents will be included into the inversion algorithm.

3.3 Boussinesq equations

Standard Boussinesq models, in their derivation, assume that nonlinearity and dispersion are small but not negligible, i.e $O(\mu^2) = O(\delta) < 1$. This approximation to the long wave model thus includes an additional dispersive term. Ursell (1953) defined a parameter, the Ursell number U_r, as the ratio of nonlinearity to dispersion effects ($U_r = \delta/\mu^2$), which determines the validity of each model. If U_r is of $O(1)$, nonlinearity and dispersion are of the same order and the Boussinesq model is more valid than the shallow water model, though still being limited to relatively shallow water areas. On the other hand, if $U_r >> 1$, then the shallow water model should be used.

The extended Boussinesq equations as derived by Madsen *et al.* (1991) and Madsen and Sørensen (1992) included third order terms in the standard Boussinesq momentum equations, and changed the linear dispersive and shoaling properties in intermediate water. The linear dispersion is expressed by a rational polynomial expansion (the Padé approximant) instead of a Taylor series expansion. By using the horizontal velocities at a reference water depth (z_α) as the dependent variables, Nwogu (1993) derived the extended Boussinesq equations with improved linear dispersion properties. He obtained the optimum value for the coefficient $\alpha = 0.39$, and the reference water depth of $z_\alpha = -0.531h$.

To extend the range of validity of the above modifications further, Wei *et al.* (1995) developed the fully nonlinear extended Boussinesq equations. Based on perturbation expansions, the velocity potential is expanded in a power series, where the dependent variable is the potential at a reference depth. All the nonlinear terms in the expansion are kept in the equations of motion. The resulting equations improve the linear dispersion properties and other nonlinear properties such as wave shoaling. The fully nonlinear time dependent equations have been programmed into a high order numerical model based on finite differences, called FUNWAVE, developed at the University of Delaware. Wave breaking, run-up and wave-induced currents have been included into the original algorithm by Chen *et al.* (2000) and Kennedy *et al.* (2000). The dimensional model equations are

$$\eta_t = E(\eta, u, v) + \gamma E_2(\eta, u, v) + f(x, y, t) \tag{3.12}$$

$$[U(u)]_t = F(\eta, u, v) + [F_1(v)]_t + \gamma[F_2(\eta, u, v) + F^t(\eta, u_t, v_t)] + F_{br} + F_b + F_{sp} \tag{3.13}$$

$$[V(v)]_t = G(\eta, u, v) + [G_1(u)]_t + \gamma[G_2(\eta, u, v) + G^t(\eta, u_t, v_t)] + G_{br} + G_b + G_{sp} \tag{3.14}$$

where $\eta(x, y, t)$ is the surface elevation, $u(x, y, t)$ and $v(x, y, t)$ are the horizontal particle velocities at the reference water depth $z = z_\alpha$ in the x and y directions respectively. γ is a control parameter determining the nonlinearity of the equations to be used in the model, i.e, fully nonlinear($\gamma = 1$) and weakly nonlinear ($\gamma = 0$). The other quantities are defined as

$$U = u + h[b_1 h u_{xx} + b_2 (hu)_{xx}] \tag{3.15}$$

$$V = v + h[b_1 h v_{yy} + b_2 (hv)_{yy}] \tag{3.16}$$

$$\begin{aligned} E = & -[(h+\eta)u]_x - [(h+\eta)v]_y \\ & -\{a_1 h^3 (u_{xx} + v_{xy}) + a_2 h^2 [(hu)_{xx} + (hv)_{xy}]\}_x \\ & -\{a_1 h^3 (u_{xy} + v_{yy}) + a_2 h^2 [(hu)_{xy} + (hv)_{yy}]\}_y \end{aligned} \tag{3.17}$$

$$F = -g\eta_x - (u u_x + v u_y) \tag{3.18}$$

$$G = -g\eta_y - (u v_x + v v_y) \tag{3.19}$$

$$F_1 = -h[b_1 h v_{xy} + b_2 (hv)_{xy}] \tag{3.20}$$

$$G_1 = -h[b_1 h u_{xy} + b_2 (hu)_{xy}] \tag{3.21}$$

The higher order dispersive terms are defined as

$$\begin{aligned} E_2 &= -\{[a_1 h^2 \eta + \frac{1}{6}\eta(h^2 - \eta^2)](u_{xx} + v_{xy})\}_x \\ &\quad -\{[a_2 h \eta - \frac{1}{2}\eta(h + \eta)][(hu)_{xx} + (hv)_{xy}]\}x \\ &\quad -\{[a_1 h^2 \eta + \frac{1}{6}\eta(h^2 - \eta^2)](u_{xy} + v_{yy})\}_y \\ &\quad -\{[a_2 h \eta - \frac{1}{2}\eta(h + \eta)][(hu)_{xy} + (hv)_{yy}]\}y \end{aligned} \tag{3.22}$$

$$\begin{aligned} F_2 &= -\{\frac{1}{2}(z_\alpha^2 - \eta^2)[u(u_x + v_y)_x + v(u_x + v_y)_y]\}_x \\ &\quad -\{(z_\alpha - \eta)[u[(hu)_x + (hv)_y]_x + v[(hu)_x + (hv)_y]_y]\}_x \\ &\quad -\frac{1}{2}\{[(hu)_x + (hv)_y + \eta(u_x + v_y)]^2\}_x \end{aligned} \tag{3.23}$$

$$\begin{aligned} G_2 &= -\{\frac{1}{2}(z_\alpha^2 - \eta^2)[u(u_x + v_y)_x + v(u_x + v_y)_y]\}_y \\ &\quad -\{(z_\alpha - \eta)[u[(hu)_x + (hv)_y]_x + v[(hu)_x + (hv)_y]_y]\}_y \\ &\quad -\frac{1}{2}\{[(hu)_x + (hv)_y + \eta(u_x + v_y)]^2\}_y \end{aligned} \tag{3.24}$$

$$F^t = \{\frac{1}{2}\eta^2[(u_t)_x + (v_t)_y] + \eta[[h(u_t)]_x + [h(v_t)]_y]\}_x \tag{3.25}$$

$$G^t = \{\frac{1}{2}\eta^2[(u_t)_x + (v_t)_y] + \eta[[h(u_t)]_x + [h(v_t)]_y]\}_y \tag{3.26}$$

F_{br} and G_{br} denote the wave breaking terms, F_b and G_b the terms due to bottom friction and F_{sp} and G_{sp} are the sponge layer terms in the x and y directions respectively. $f(x, y, t)$ is the source function term used to generate waves internally in the model.

$$a_1 = \frac{1}{2}\beta^2 - \frac{1}{6}, a_2 = \beta + \frac{1}{2}, b_1 = \frac{1}{2}\beta^2, b_2 = \beta \tag{3.27}$$

where $\beta = \frac{z_\alpha}{h} = -0.531$.

3.4 Nwogu's linearized equations

Nwogu's weakly nonlinear Boussinesq equations in one horizontal dimension (x) are found by setting $\gamma = 0$ in (3.12-3.13). If we disregard the wave breaking, bottom friction, sponge layer and source function terms, linearize the resulting equations, replace the time derivatives with the space derivatives, and integrate along x as above, we arrive at the linearized time independent mass and momentum inversion equations

$$C\eta = hu + a_1 h^3 u_{xx} + a_2 h^2 (hu)_{xx} \tag{3.28}$$

$$\frac{g\eta}{C} = u + h[b_1 h u_{xx} + b_2 (hu)_{xx}] \tag{3.29}$$

where the parameters a_1,a_2,b_1,and b_2 are dimensionless parameters previously defined in (3.27).

3.5 Fully nonlinear extended Boussinesq equations

Starting with the fully nonlinear extended equations of Wei *et al.* (1995) and proceeding in a similar fashion, but keeping all the nonlinear terms, we get the fully nonlinear inversion equations. The mass equation is

$$\frac{C\eta}{h+\eta} = Pu + Qu_x + Ru_{xx} \tag{3.30}$$

where

$$\begin{aligned} P &= 1 + (-\frac{\eta}{2} + a_2 h) h_{xx} \\ Q &= 2(-\frac{\eta}{2} + a - 2h_x) \\ R &= a_1 h^2 + \frac{\eta(h-\eta)}{6} + (-\frac{\eta}{2} + a_2 h) h \end{aligned}$$

The momentum equation is

$$Lu + Mu_x + Nu_{xx} = S - g\eta \tag{3.31}$$

where

$$
\begin{aligned}
L &= 1 + b_2 h h_{xx} \\
M &= 2b_2 h h_x - \eta h_x \\
N &= h^2 b_1 + b_2 h^2 - \frac{\eta^2}{2} - \eta h \\
S &= [-\frac{u^2}{2} - \{\frac{1}{2}(z_\alpha^2 - \eta^2) u u_{xx}\} - \{(z_\alpha - \eta)[u(hu)_{xx}]\} \\
&- \frac{1}{2}\{[(hu)_x + \eta u_x]^2\} - g\eta]\frac{1}{C}
\end{aligned}
$$

where all the nonlinear convective terms have been collected in S.

3.6 Including mean flow effects

The inversion equations derived above cannot account for current effects, since the integration constants involving the mean flow quantities were neglected. Wave transformation such as shoaling and wave breaking and the associated nonlinear effects in shallow water gives rise to several mean flow effects such as changes in the mean water level (setup and setdown) and in velocities, giving rise to currents (undertow, rip currents and mean drifts). Tidal currents may also be present near river mouths and estuaries, which would modify the mean levels of the water mass and change its velocity profile. The wave phase speed is also Doppler shifted by the presence of a mean current. With respect to a stationary frame of reference, the wave would appear to travel faster on a following current and slower on an opposing current. This shift in the phase speed would be inferred as a corresponding (but spurious) change in the bathymetry in the present depth inversion algorithm. Any inversion procedure to determine the correct underlying bathymetry near the coast has thus to take into account the effect of currents.

The mean of a wave quantity, say $\zeta(x,t)$, is usually calculated by time averaging (or wave averaging) over a wave period, and is defined mathematically as

$$\overline{\zeta(x)} = \int_{t}^{t+T} \zeta(x,t)dt \tag{3.32}$$

In one horizontal dimension (x), the nonlinear shallow water equations, after replacing the time derivatives with the spatial derivatives, can be integrated along x to arrive at

$$-C\eta_1 + [u_1(h+\eta_1)] = A_1 \tag{3.33}$$

$$-Cu_2 + \frac{{u_2}^2}{2} + g\eta_2 = B_1 \tag{3.34}$$

where the subscripts 1 and 2 denote quantities in the mass and momentum equations respectively. This convention will be followed throughout the rest of this thesis. We can split the total surface elevation and orbital velocity into a pure wave part and a wave averaged part

$$\eta = \eta_w + \overline{\eta}, u = u_w + \overline{u} \tag{3.35}$$

where w denotes the oscillatory part and the over bar $-$, the mean part of a quantity. Substituting in the mass and momentum equations (and dropping the subscripts 1 and 2 at present), we get

$$-C(\eta_w + \overline{\eta}) + u_w(h + \eta_w + \overline{\eta}) + \overline{u}h + \overline{u\eta} + \overline{u}\eta_w = A \tag{3.36}$$

$$-C(\overline{u} + u_w) + (\frac{\overline{u}^2 + {u_w}^2}{2} + \overline{u}u_w) + g\overline{\eta} + g\eta_w = B \tag{3.37}$$

The integration constants A and B can be determined by considering the case when waves are absent, in which case

$$A = \overline{u_1(h+\eta_1)} \tag{3.38}$$

$$B = \frac{\overline{u_2}^2}{2} + g\overline{\eta_2} \tag{3.39}$$

It is obvious that when mean flows are present, the integration constants cannot be neglected. Consider the case when total velocity data is available but not given separately as wave and current parts. The elevation and depth are unknown. The mean flow is a time averaged quantity by definition, but since time series of velocity data are not available (only spatial information at two time instances is given), we calculate the current from the total velocity by locally averaging in space over each individual wavelength. This would be exact for a strictly periodic wave in space and time. The first approximation in this formulation is thus to assume that the spatial variation of current can be obtained by averaging the total velocity over the local wavelength (which also changes in space). The local wavelengths similarly are obtained by a zero crossing method for calculating $\overline{\eta}$. To calculate $\overline{u}$, zero crossing positions could not be identified because the total velocity at times remained either positive or negative over large distances (more than the local wavelength). The local wavelength was instead defined as the distance between two successive crest positions in the velocity map. After calculating the mean quantities $\overline{u}$ and $\overline{\eta}$, the wave part of the elevation and velocity is calculated by subtracting from the total variable,

$$u_w = u - \overline{u}, \eta_w = \eta - \overline{\eta} \tag{3.40}$$

If both the elevation and velocity variables are provided as data, A and B can be evaluated from (3.38-3.39) using an assumed h and then an iterative procedure can be developed till the depth converges. However, with the availability of only one kind of data, two more approximations can be made to solve (3.36-3.37) including mean flow effects. Let us consider the case when only total velocity is available and the current is assumed to be time invariant and depth uniform. It is obvious that A and B cannot be determined, since $\overline{\eta}$ is unknown, and so is h. We assume that

$$\overline{\eta}_1 \approx \overline{\eta}_2 \approx 0 \tag{3.41}$$

and so $A = \overline{u}_1 h$ and $B = \frac{\overline{u}_2{}^2}{2}$. It is still difficult to calculate A, since the depth h is unknown. To overcome the above difficulties, we formulate the problem in a slightly different manner. Since (3.36 - 3.37) involve both the wave and mean parts of the variables (because of which $A_1 \neq 0$ and $B_1 \neq 0$), we formulate the corresponding equations valid only for the pure wave part

$$-C_0 \eta_{1_w} + u_{1_w}(h + \eta_{1_w}) = 0 \tag{3.42}$$

$$-C_0 u_{2_w} + \frac{{u_{2_w}}^2}{2} + g\eta_{2_w} = 0 \tag{3.43}$$

where $C = C_0 + \overline{u}$, is the Doppler shifted phase speed. The equations above are the same nonlinear shallow water inversion equations (3.33-3.34), but are exact when solving for pure wave motion (when the integration constants can be set to zero). It is to be noted that A_1 and B_1 have not been neglected but cancel out with the mean quantities in the mass and momentum equations. The phase speed C_0 in (3.42-3.43) is the corrected phase speed which could be obtained in two different ways. It could be estimated from the spatial maps of the pure wave part of the total velocity, or by subtracting the Doppler shift effect, which is essentially the current, from the phase speed estimated from the total velocity images. The mean velocity found by averaging spatially over a local wavelength is subtracted from the total velocity and the pure wave part is substituted into the above equations.

If on the other hand, mean flows are present and only surface elevation data is given in the form of spatially dense images, the determination of the pure wave quantities remains ambiguous. The mean currents cannot be determined from elevation data and neither can they be neglected in favor of the mean water level changes. The present modification for mean flow effects to the inversion method can thus only be performed with total velocity data.

Chapter 4

INVERSION ALGORITHM

The estimation of local phase speeds from spatially discrete information in the form of surface elevation or particle velocity has been formulated in chapter 2. Since the available information is dense in space, but known only at two separate time instances, we have developed the time-indendent inversion equations in chapter 3. In this chapter we describe how the inversion equations can be solved with given surface data and computed phase speeds, to estimate the unknown depth and the particle kinematics. Consider the time independent linearized shallow water inversion equations as derived in section 3.2

$$-C\eta_1 + hu_1 = 0 \tag{4.1}$$

$$-Cu_2 + g\eta_2 = 0 \tag{4.2}$$

where the integration constants have been neglected. Let us begin by assuming that only surface elevation data (η) is available and no information about velocities is given. The depth inversion problem remains to estimate the true depth (h) from given surface elevation data and calculated phase speed C. The ratio of the mass and momentum equation velocities is

$$\frac{u_1}{u_2} = \frac{C^2}{gh}\frac{\eta_1}{\eta_2} \tag{4.3}$$

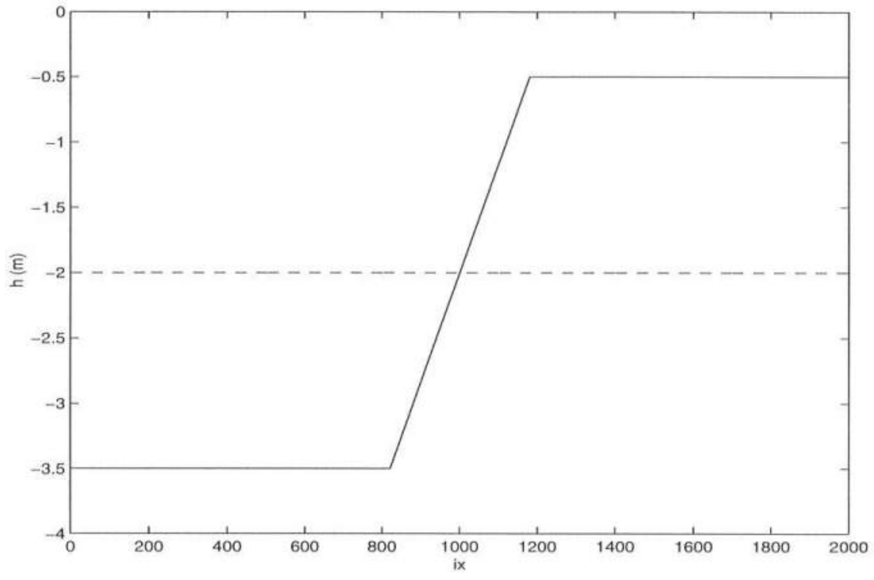

Figure 4.1: Assumed depth h_0 (- -) compared to the actual depth h (-)

The first step in the inversion algorithm is to assume a starting depth, and in every case considered here, a flat bottom of arbitrary depth throughout the domain is fixed as a first guess. Let this be denoted as h_0. Figure 4.1 shows both the assumed depth and the actual depth plotted against the grid position in the x-direction (ix). Since the grid spacing dx is $0.25m$, in physical units, $ix = n$ corresponds to a distance of $(n-1)dx$ from the origin. This discretization and notation will be followed throughout the rest of this thesis. The flat bed here is taken to be somewhere between the maximum and minimum actual depths. We then substitute the elevation data into the mass and momentum equations so that $\eta_1 = \eta_2 = \eta$. This essentially means that the data from a single image is substituted into both the mass and momentum equations. The computed phase speed is expressed in terms of the shallow water depth as $C^2 = gh_{sh}$, where the shallow water depth (h_{sh}) is the first estimate in the inversion. C is calculated from the given true surface elevation data and is hence a correct representation of the true depth, and therefore, the first estimate of depth (h_{sh}) would be incorrect. On substituting for C in terms of h_{sh} into (4.3) we get

$$\frac{u_1}{u_2} = \frac{h_{sh}}{h_0} \tag{4.4}$$

If the assumed depth (h_0) is less than h_{sh}, then $u_1 > u_2$. Figure 4.2 shows the mismatch in the velocities calculated from the mass and momentum equations. It can be seen that wherever the assumed depth is less than the shallow water depth, u_1 is greater than u_2 and vice versa. At a grid position of about $ix = 1000$ where $h_0 = h_{sh}$, the velocities are also equal. A new estimate of depth (h_{new}), which in the first iteration is the shallow water depth ($h_{new} = h_{sh}$), would be given (based on this velocity mismatch) as

$$h_{new} = h_0 \frac{u_1}{u_2} \tag{4.5}$$

The depth is iteratively updated until the ratio of velocities calculated from the mass and momentum equations approaches unity and the estimated depth iterate approaches the true depth ($h_{new} \rightarrow h$).

Consider the parallel inversion case, when only particle velocity (u) is given over the domain. The surface elevation η and depth h are unknown quantities. From (4.3), the ratio of elevations from the two equations on eliminating the phase speed, is

$$\frac{\eta_1}{\eta_2} = \frac{h_0}{h_{sh}} \tag{4.6}$$

where $u_1 = u_2 = u$. If the assumed depth is less than the shallow water depth (the first estimate), η_1 is also less than η_2 and where the assumed depth is greater than

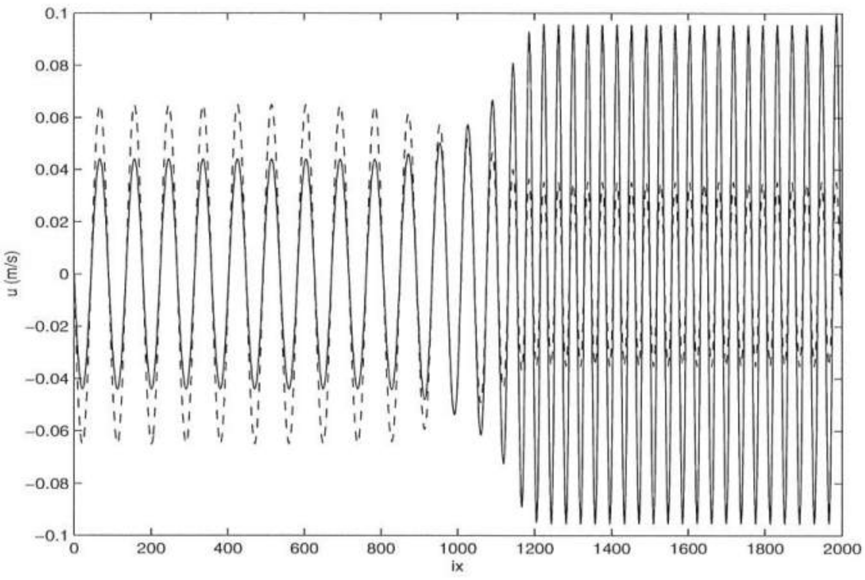

Figure 4.2: Velocities calculated for the first estimate of depth ($h_{new} = h_{sh}$). $u_1(--)$ and $u_2(-)$

the shallow water depth, η_1 is greater than η_2. Starting from a flat bed, a new depth estimate can thus be obtained from

$$h_{new} = h_0 \frac{\eta_2}{\eta_1} \tag{4.7}$$

As before, the depth is updated till the ratio of surface elevations approaches unity.

4.1 Linearized inversion equations

The linearized inversion equations based on Nwogu's linearized extended Boussinesq equations are

$$\eta_1 = \frac{hu_1 + a_1 h^3 u_{1xx} + a_2 h^2 (hu_1)_{xx}}{C} \tag{4.8}$$

$$\eta_2 = \frac{\{u_2 + h[b_1 h u_{2xx} + b_2 (hu_2)_{xx}]\}C}{g} \tag{4.9}$$

Based on the type of data availability, we can differentiate two separate cases. CASE I, when only surface elevation data (η) is given and the velocity and depth are unknown quantities, and CASE II, when only particle velocity data (u) is given, the elevation and depth being unknown.

Let us first consider the mathematically simpler CASE II. The right hand side of both the mass and momentum equations can be calculated (the depth h though being an assumed quantity, is known) by substitution of the variables and their derivatives. Central finite differences are used to calculate the derivatives. η_1 and η_2 are calculated over the entire spatial domain by solving the two equations. It is to be noted that u_1 and u_2 here do not represent the data from two separate images. The subscripts are merely used to differentiate the variable in the mass and momentum equations. Although the phase speed C is calculated from the two given velocity images (say u_{01} and u_{02}), either image (u_{01} or u_{02}) can be used as given data for both u_1 and u_2. The actual inversion (as opposed to the least squares estimation of phase speed) is thus performed with only one image and the final converged estimated elevation profile compared to that particular image data. The domain is subdivided through finite size windows of size W. The window is shifted across the domain over discrete distances to calculate a new estimate of depth

$$h_{new}(j) = h_{old}(j)\left(\frac{\sum_{i=j-W/2}^{i=j+W/2}|\eta_2(i)|}{\sum_{i=j-W/2}^{i=j+W/2}|\eta_1(i)|}\right)^{\beta} \tag{4.10}$$

where β is a kind of shallowness parameter, similar to the one used by Kennedy *et al.* (1999) in their depth updating algorithm. $\beta = 1$ leads to the shallow water estimate of the depth as would be obtained from (4.7). The effect of the shallowness parameter in the convergence of the depth iterates is discussed in the next chapter. i and j denote spatial grid positions. $h_{old} = h_0$ and $h_{new} = h_{sh}$ in the first iteration of depth. W is the window size over which the summation is done and has to be approximately on the order of a wavelength to reduce numerical noise and provide enough wave information within the window. The absolute values of the surface elevation are taken to prevent cancellation from positive and negative values within a wavelength, which would cause the ratio to take on unnaturally large values. Instead of the modulus, the squares of the surface elevation can also be used with no perceptible changes in results. The summation is therefore done over $W+1$ grid points, and is defined at the center of the grid at $i=j$. These point estimates are then linearly interpolated and extrapolated to the boundaries, to get a depth estimate over the entire domain.

The mismatch in surface elevations calculated from the two equations is also used as a convergence criterion to stop the iteration process. The total error over the entire domain is defined as

$$\epsilon = \sum_{i=1}^{i=N} \{ \left| \ |\eta_1(i)| - |\eta_2(i)| \ \right| \} \tag{4.11}$$

where N is the total number of grid points in the domain. Theoretically, the true value of the error, when the iterated depth converges to its final value, should be $\epsilon = 0$. But because of approximations in the solution, such as a linear interpolation over the domain, the mass and momentum equations cannot be solved to give exact values of the elevations. The error ϵ therefore always is a finite nonzero quantity. Since a minimum error also cannot be predefined (because the true surface elevation is an unknown quantity), the iteration is terminated when the error approaches a constant value within a predefined arbitrary tolerance. Figure 4.3 shows the total mismatch between the calculated surface elevations summed over the domain, plotted against the number of iterations for the linearized case. Based on previous model runs, the maximum number of iterations for this case was fixed at 9. The error drops to its minimum constant value after about 5 to 6 iterations. The algorithm thus converges to a final depth and surface elevation estimate very quickly.

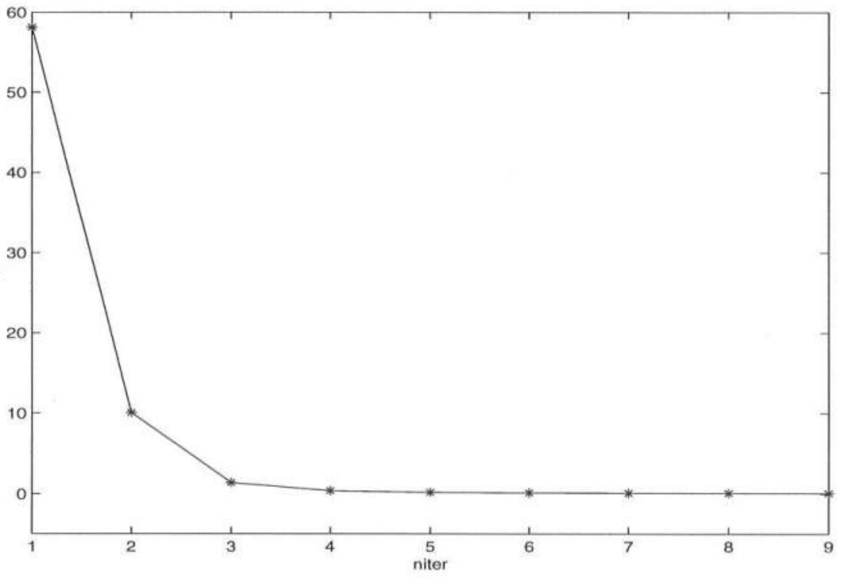

Figure 4.3: The total mismatch of surface elevations (ϵ) at successive iterations (niter) in the linearized inversion case.

A parallel inversion method (CASE I) was developed, assuming the availability of only surface elevation data. The inversion problem reduces to solving the mass and momentum equations for $u(x)$ and $h(x)$. The linearized inversion equations (4.8-4.9) can be recast in the following manner

$$u_1[h + a_2 h^2 h_{xx}] + u_{1x}[a_2 h^2 2h_x] + u_{1xx}[(a_1 + a_2)h^3] = C\eta_1 \tag{4.12}$$

$$u_2[1 + b_2 h h_{xx}] + u_{2x}[2b_2 h h_x] + u_{2xx}[(b1 + b_2)h^2] = \frac{g\eta_2}{C} \tag{4.13}$$

Since the true values of the surface elevation are given ($\eta_1 = \eta_2 = \eta$) and C is calculated from the given surface images, the right hand side of both the equations is known. On using centralized finite differences for the derivatives in the unknowns u_1 and u_2, the linearized mass and momentum equations become tridiagonal in the unknowns u_1 and u_2 respectively, and are solved using a tridiagonal matrix solver. Tridiagonal solvers require boundary values to be specified for the unknown, which here are the unknown particle velocities u_1 and u_2. We therefore arbitrarily set the values $u_1(1) = u_1(N) = 0$ and $u_2(1) = u_2(N) = 0$. This approximation has been seen to affect computations marginally near the boundaries and does not propagate into the domain. A new estimate of depth is obtained as

$$h_{new}(j) = h_{old}(j)\left(\frac{\sum_{i=j-W/2}^{i=j+W/2} |u_1(i)|}{\sum_{i=j-W/2}^{i=j+W/2} |u_2(i)|}\right)^{\beta} \tag{4.14}$$

The mismatch in velocities calculated from the mass and momentum equations is used as a convergence criterion, and the total error is defined as

$$\epsilon = \sum_{i=1}^{i=N} \{ |\ |u_1(i)| - |u_2(i)|\ | \} \tag{4.15}$$

The iteration is similarly terminated when ϵ approaches a constant value.

4.2 Fully nonlinear inversion equations

Let us consider CASE II first, when only velocity data is available. The mass equation can be written as

$$P_1\eta_1 + Q_1\eta_1^2 + R_1\eta_1^3 = S_1 \tag{4.16}$$

$$\begin{aligned}
P_1 &= [u_1 - C + a_1 h^2 u_{1xx} + \frac{h^2 u_{1xx}}{6} - \frac{h(hu_1)_{xx}}{2} + a_2 h (hu_1)_{xx}] \\
Q_1 &= [-\frac{(hu_1)_{xx}}{2}] \\
R_1 &= [-\frac{u_{1xx}}{6}] \\
S_1 &= [-a_1 h^3 u_{1xx} - hu_1 - a_2 h^2 (hu_1)_{xx}]
\end{aligned}$$

Dividing throughout by R_1 and collecting all terms on the left hand side gives

$$\eta_1^3 + Q_2\eta_1^2 + P_2\eta_1 + S_2 = 0 \tag{4.17}$$

where $Q_2 = \frac{Q_1}{R_1}$, $P_2 = \frac{P_1}{R_1}$ and $S_2 = \frac{S_1}{R_1}$. Equation (4.17) is a cubic equation in the unknown η_1 and has analytic solutions which can be found in any standard mathematics text. The momentum equation can be written as

$$P_3\eta_2 + Q_3\eta_2^2 = S_3 \tag{4.18}$$

$$\begin{aligned}
P_3 &= g - u_2(hu_2)_{xx} + (hu_2)_x u_{2x} + Ch_x u_{2x} + Chu_{2xx} \\
Q_3 &= -\frac{u_2 u_{2xx} + {u_{2x}}^2 + u_{2xx}C}{2} \\
S_3 &= C[u_2 + h^2 u_{2xx}(b_1 + b_2) + b_2 hh_{xx} u_2 + 2b_2 hh_x u_{2x}] \\
&- \frac{{u_2}^2}{2} - \frac{z_\alpha^2 u_2 u_{2xx}}{2} - z_\alpha u_2 (hu_2)_{xx} - \frac{{(hu_2)_x}^2}{2}
\end{aligned}$$

Dividing throughout by Q_3 and collecting all the terms on the left hand side, we get

$$\eta_2^2 + P_4\eta_2 + S_4 = 0 \tag{4.19}$$

where $P_4 = \frac{P_3}{Q_3}$ and $S_4 = \frac{S_3}{Q_3}$. The momentum equation (4.19) is quadratic in the unknown η_2 and has standard analytic solutions. Since there exists more than one solution for both the mass and momentum equations (the equations being cubic and quadratic), of which only one is the correct value, and since solving the mass equation involves evaluating complex quantities, a simpler solution procedure using Newton Raphson method was used. It was found, however, that solutions from either method for both the mass and momentum equations were the same. The Newton Raphson method requires an initial guess or a seed value, which in this case was provided by first solving the linearized mass and momentum equations (4.8 - 4.9), and then substituting the solution as an initial guess to solve (4.17) and

(4.19). The iteration of depth remained the same, based on the mismatch between the calculated values of η_1 and η_2.

The inversion procedure for CASE I can be formulated by rewriting (for convenience) the fully nonlinear inversion equations (4.17 and 4.19) in terms of the unknown velocities u_1 and u_2. The mass equation is

$$L_1 u_1 + M_1 u_{1x} + N_1 u_{1xx} = \frac{C\eta_1}{h+\eta_1} \tag{4.20}$$

$$\begin{aligned}
L_1 &= [1 + (-\frac{\eta_1}{2} + a_2 h) h_{xx}] \\
M_1 &= 2(-\frac{\eta_1}{2} + a_2 h) h_x \\
N_1 &= [a_1 h^2 + \frac{\eta_1 (h-\eta_1)}{6} + (-\frac{\eta_1}{2} + a_2 h) h]
\end{aligned}$$

The momentum equation is given by

$$L_2 u_2 + M_2 u_{2x} + N_2 u_{2xx} = \frac{K_2 - g\eta_2}{C} \tag{4.21}$$

$$\begin{aligned}
L_2 &= 1 + b_2 h^2 h_{xx} \\
M_2 &= 2 b_2 h h_x - \eta_2 h_x \\
N_2 &= h^2 (b_1 + b_2) - \frac{{\eta_2}^2}{2} - \eta_2 h \\
K_2 &= [-\frac{{u_2}^2}{2} - \{\frac{1}{2}(z_\alpha^2 - {\eta_2}^2) u_2 u_{2xx}\} - \{(z_\alpha - \eta_2)[u_2 (h u_2)_{xx}]\} \\
&- \frac{1}{2}\{[(h u_2)_x + \eta_2 u_{2x}]^2\}]
\end{aligned}$$

Since η_1, h and C are known quantities, the mass equation is tridiagonal in u_1 and can be solved using tridiagonal matrix solvers, where again the boundary values for u_1 and u_2 are set to zero. The left hand side of the momentum equation is also tridiagonal in u_2, but the term K_2 contains nonlinear convective terms involving the unknown u_2 itself. The momentum equations is thus solved iteratively. At the first iteration all the nonlinear terms in u_2 are neglected ($K_2 = 0$) and the following linear tridiagonal equation is solved for u_2

$$L_2 u_2 + M_2 u_{2x} + N_2 u_{2xx} = -g\eta_2 \tag{4.22}$$

The solution to (4.22) is used to calculate K_2. K_2 is then substituted into (4.21) to calculate the solution to the fully nonlinear equation. Based on the mismatch between u_1 and u_2, the depth is updated as before.

4.3 Modifications due to mean flow effects

The existing inversion methodology has to be modified to account for prescribed mean flows in the given data, in both the surface elevation and velocity maps. The synthetic input data is generated by specifying a constant volume flux (q) across the spatial domain in FUNWAVE. The depth uniform time invariant current is given by

$$U(x) = \frac{q_w}{h(x)} \tag{4.23}$$

where $h(x)$ is the spatially varying water depth and q_w is a constant volume flux per unit width (in the y-direction). Since the images to be generated had to be purely one dimensional, the width was fixed at unity throughout the domain. Due to the varying depth, the current U changes with x. A following or opposing current can be specified by choosing a positive or negative value for the volume flux respectively. Due to the current, there is also a depression in the mean water level which also varies spatially across the domain.

Consider the fully nonlinear mass and momentum inversion equations

$$L_1 u_1 + M_1 u_{1x} + N_1 u_{1xx} = \frac{C\eta_1}{h + \eta_1} + A \tag{4.24}$$

$$L_2 u_2 + M_2 u_{2x} + N_2 u_{2xx} = \frac{K_2 - g\eta_2}{C} + B \tag{4.25}$$

where A and B are the integration constants and the coefficients are the same as in (4.20-4.21). We can split the total variable into a pure wave and a mean part as

$$\eta_1 = \eta_{1w} + \overline{\eta_1} \tag{4.26}$$

and similarly for the other variables. The phase velocity C is the Doppler shifted speed due to the current

$$C = C_0 + U \tag{4.27}$$

We first neglect the integration constants, i.e $A = B = 0$. When the constants are put to zero, the inversion equations reduce to (4.8-4.9), when velocity data is given, and (4.12-4.13), when elevation data is given. Though the inversion equations are the same it is to be noted that the input data used in the above equations has mean flow quantities inherent in it and that the phase speed is Doppler shifted by the current. It is expected that the results will be in error, and they are discussed under CASE IIB in the next chapter.

The next step is to retain the integration constants in the inversion equations. We however do not directly evaluate A and B in terms of the mean quantities. Instead, the mean quantities are subtracted from the total given surface elevation or velocity data and the resulting pure wave data is used as input to the inversion model. As discussed before, we make the approximation that $\overline{\eta_1} = \overline{\eta_2} = 0$ and can invert the depth for the case when only velocity data is given. The inversion equations are thus reduced to

$$\eta_{1w}^3 + Q_2\eta_{1w}^2 + P_2\eta_{1w} + S_2 = 0 \tag{4.28}$$

$$\eta_{2w}^2 + P_4\eta_{2w} + S_4 = 0 \tag{4.29}$$

where the coefficients are the same as in (4.17) and (4.19) but involve only the pure wave part of the quantities. The rest of the inversion process remains essentially the same as before.

Chapter 5

RESULTS

The synthetic input data (in the form of time lagged spatial maps of surface elevation and orbital velocities) was generated by running the fully nonlinear time-dependent extended Boussinesq model FUNWAVE. By changing the value of γ, the nonlinearity control parameter in the model, model runs were performed for Nwogu's linearized equations ($\gamma = 0$) and the fully nonlinear extended Boussinesq equations of Wei *et al.* (1995) ($\gamma = 1$). The images were saved at specified time steps separated by a fraction of a wave period. Monochromatic and groupy wave conditions were simulated in the model. The phase speeds were calculated from the saved images using the least squares method. With an arbitrarily assumed flat bottom as the starting depth, inverted depths were calculated. The convergence of the depth estimates was determined by recording the error (ϵ) and the depth estimate at each iteration. Particle kinematics were computed after the inverted depth had converged.

The inversion tests are broadly divided into two sections. Results under the first section (CASE I) assume the availability of surface elevation data in the form of two spatial maps at two different time instances. The second section (CASE II) shows the inversion results with velocity data given in the same form. In each section, different input wave conditions are analyzed, and inversion is performed with both the linearized and nonlinear inversion equations. For the first section, along with depth estimates, the spatial variation of orbital velocities is also calculated and compared with the FUNWAVE results. Similarly, in the second section, estimated maps of surface elevation are compared to those obtained from FUNWAVE. The estimated phase speeds are compared to the analytic phase speed obtained from Nwogu's linearized dispersion relationship. Inverted depths are calculated in the presence of initially prescribed mean flows for monochromatic waves and for fully nonlinear equations with both surface elevation and velocity data.

5.1 Inversion with surface elevation data (CASE I)

Two different types of surface elevation data from the FUNWAVE model have been considered, one in which there were no prescribed mean flows (CASE IA), and the second in which an initial mean current was prescribed (CASE IB) in the model. Inversion for CASE IB is done with the inversion equations where the integration constants were neglected.

5.1.1 No prescribed mean flows in surface elevation data (CASE IA)

There were no prescribed mean flows in CASE IA, i.e $\overline{\eta} = 0$ and $U = 0$. We first discuss the linearized inversion results. A progressive monochromatic wave with wave height $H = 5cm$, wave period $T = 4.369s$ was allowed to propagate over a 1 : 30 plane slope. The deep water depth was $h_d = 3.5m$ and in the shallow region, the water depth was $h_s = 0.5m$. The model (FUNWAVE) grid spacing was $dx = 0.25m$ and the time step was $dt = 0.02s$. The total domain length was $nx = 3001$ (ix denotes the spatial grid location). Sponge layers of width 25 m and 50 m were applied on the seaward and shoreward boundaries respectively. The nonlinearity parameter in FUNWAVE was $\gamma = 0$. No wave breaking was observed as the wave propagated over the changing topography. The elevation and velocity maps were stored at six time steps $it1 = 20050$, $it2 = 20075$, $it3 = 25000$, $it4 = 25050$, $it5 = 30000$ and $it6 = 30100$. The first image was collected after about 400 waves

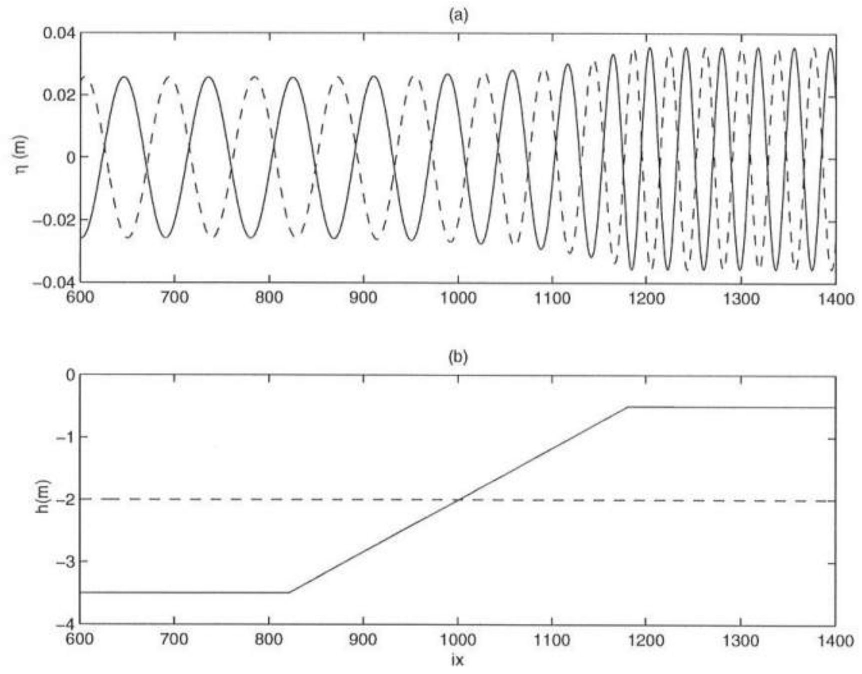

Figure 5.1: (a) Wave surface images for CASE IA generated in FUNWAVE with $\gamma = 0$ (b) Assumed(- -) and actual depth(-)

had been generated by the source function, which is much longer than that needed for the first few transient waves to die out. Steady state wave conditions had thus been reached before the data was recorded. The time lag between two consecutive images was varied to investigate possible effects on phase speed and depth estimation.

The top panel (a) in Figure 5.1 shows the two surface images. The dashed line is the image at $it5$ and the solid line is the later image at $it6$. The images are thus separated by $\delta t = 2.0s$ which is about half the wave period. The effect of time lag on the estimate of wave phase speed or the depth estimate in the monochromatic wave tests was negligible. However, in the groupy wave tests, the time separation between the images does affect both the speed and depth estimates markedly, and

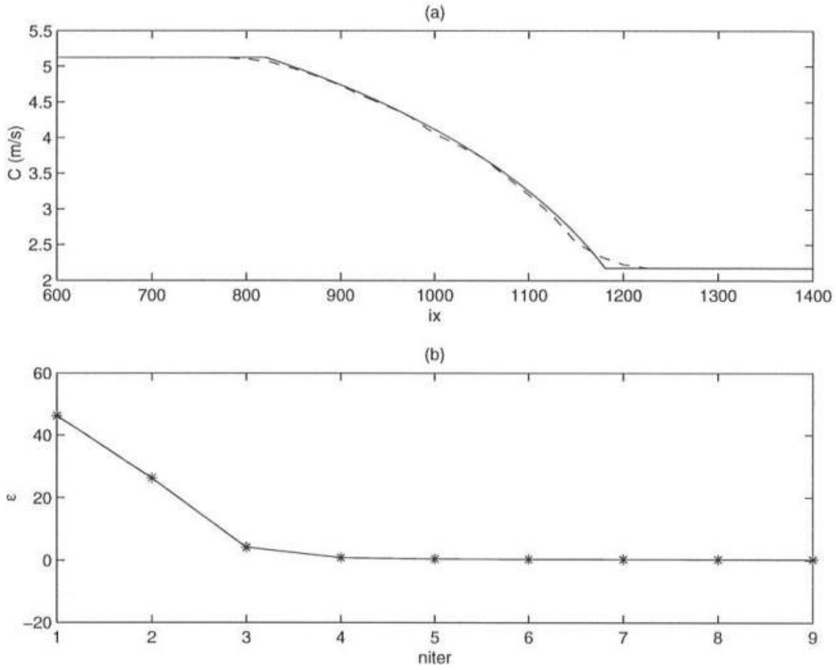

Figure 5.2: (a) Analytic (-) and estimated (- -) wave phase speed for CASE IA. (b) Total velocity mismatch (ϵ) at successive iterations (niter)

will be discussed later. The x-axis (ix) shows the spatial grid location and the y-axis shows the surface elevation. Even though FUNWAVE was run with a spatial domain of 3001 points, in all the inversion tests the domain has been truncated to get rid of the sponge layers and parts of the uninteresting flat regions on either side of the slope. In the bottom panel, the actual analytic depth used in FUNWAVE to generate the depths is plotted as the solid line. The dashed line shows the assumed depth, which in this case was a flat bottom of depth $h = 2.0m$.

The linear analytic phase speed (solid line) is plotted with the least square estimated phase speed (from the two surface images) in the top panel of Figure 5.2. The window size was $W = 25m$ (which in grid numbers, shown in the figures as ix, means ix to $ix + 100$, since the grid spacing was $\delta x = 0.25m$) and the window

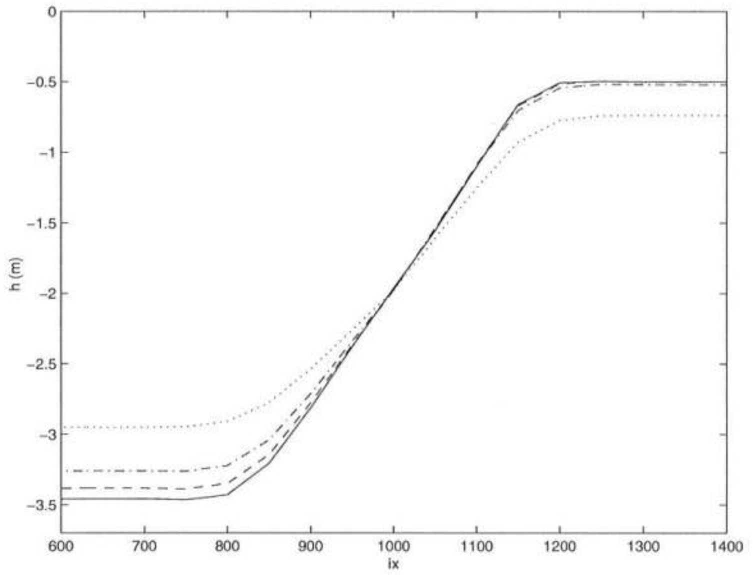

Figure 5.3: Estimated inversion depths for CASE IA, $\beta = 1.0$: niter=1(.), niter=2(-.), niter=3(- -), niter=5(–)

shift (ws) was $ws = 5m$, which means that the wave celerity was estimated at five equidistant points within a window. Linear interpolation was done to calculate the celerity variation over the whole domain. The analytic speed is estimated accurately except at the sharp corners in the bathymetry, because of the large finite window size. The bottom panel shows the absolute value of the velocity mismatch summed over the whole domain (ϵ), plotted against the iteration number in the inversion algorithm. Convergence is fast and the error decreases monotonically to its minimum value within about five iterations. No predefined tolerance values were set for a convergence criteria. Based on previous inversion tests, the maximum number of iterations was fixed at 9. This is somewhat of an overkill, since the iteration could be stopped without affecting the results, after about five iterations.

Figure 5.3 shows the estimated depth iterates for the particular iteration number. The shallowness parameter $\beta = 1.0$. The depth converges to its final value

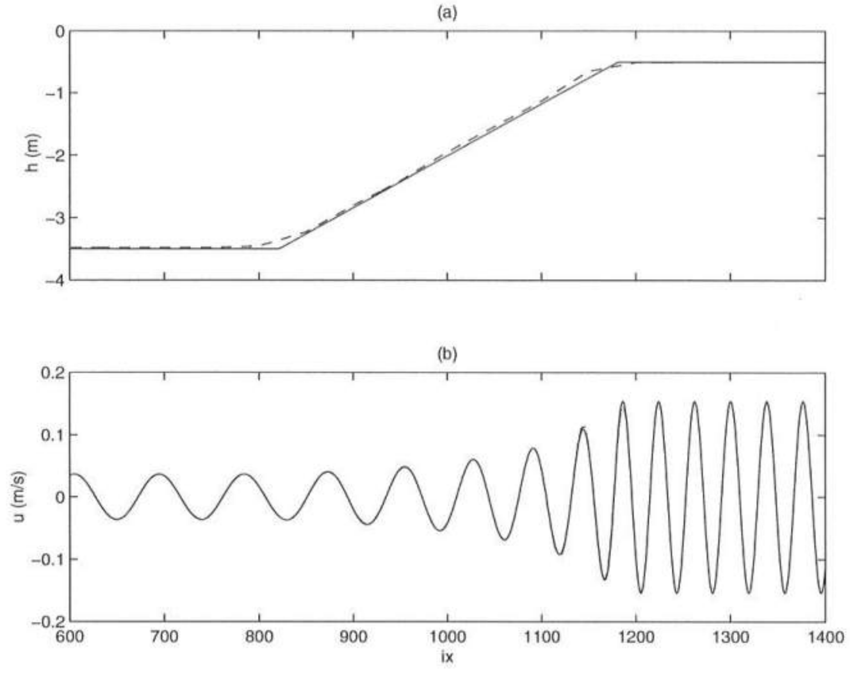

Figure 5.4: (a) Actual (–) and inverted depth (- -) for CASE IA. (b) Actual(–) and estimated velocities { u_1 (.), u_2 (- -) }

in the first couple of iterations. The dotted line is the first estimate calculated from the shallow water inversion equations. The velocity mismatch drives this shallow water estimate to its final converged value. The top panel of Figure 5.4 shows the final converged inverted depth compared to the actual or true depth.

The depth estimate agrees well with the analytic bathymetry except at the sharp corners. The smearing in phase speed translates to a corresponding loss in resolution in the inverted depth. From (4.1-4.2), for a given depth, we can see that an overprediction of phase speed leads to an overprediction in u_1 and an underprediction in u_2. Similarly, if the computed phase speed is smaller than the true phase speed, u_1 would be smaller than u and u_2 would be greater than u, where u is the true value of the particle velocity. This can be observed by comparing Figure 5.2 (top

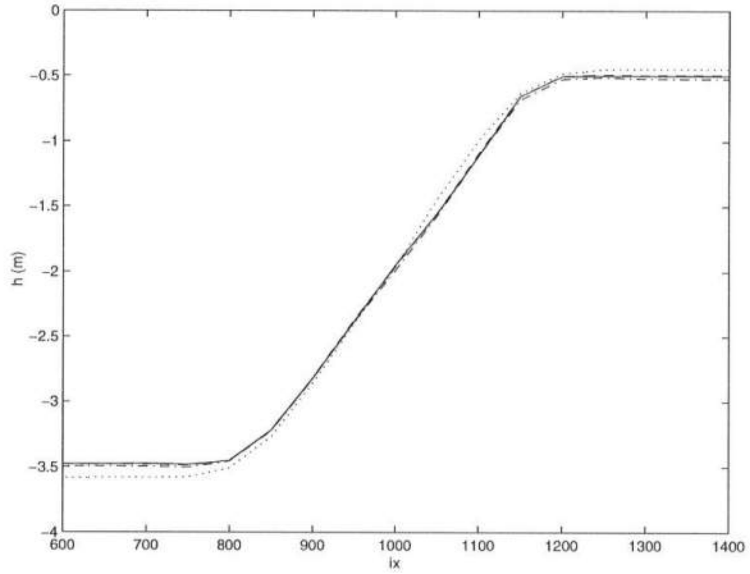

Figure 5.5: Inverted depths for CASE IA, $\beta = 1.5$: niter=1(.), niter=2(-.), niter=3(- -), niter=5(–)

panel) and Figure 5.4 (bottom panel) near the corners of the bottom slope. Also, from (4.5) it can be seen that a discrepancy in the computed velocities translates to a corresponding error in the inverted depth. For example, at the offshore toe of the slope, the phase speed is underpredicted, which leads to an underprediction of u_1 and a corresponding underprediction in depth. The comparison of actual and estimated velocities (from the mass equations (u_1) and the momentum equation (u_2)) shows that the velocity estimates are accurately predicted from the inversion equations. This additional ability of the present inversion methodology (to accurately predict the velocities, given surface elevation) can be used effectively in other inversion algorithms where both variables are required to estimate depth, but only one is available.

The shallowness parameter can be increased to accelerate convergence, as can be seen by comparing Figure 5.3 with Figure 5.5 where $\beta = 1.0$ and $\beta = 1.5$

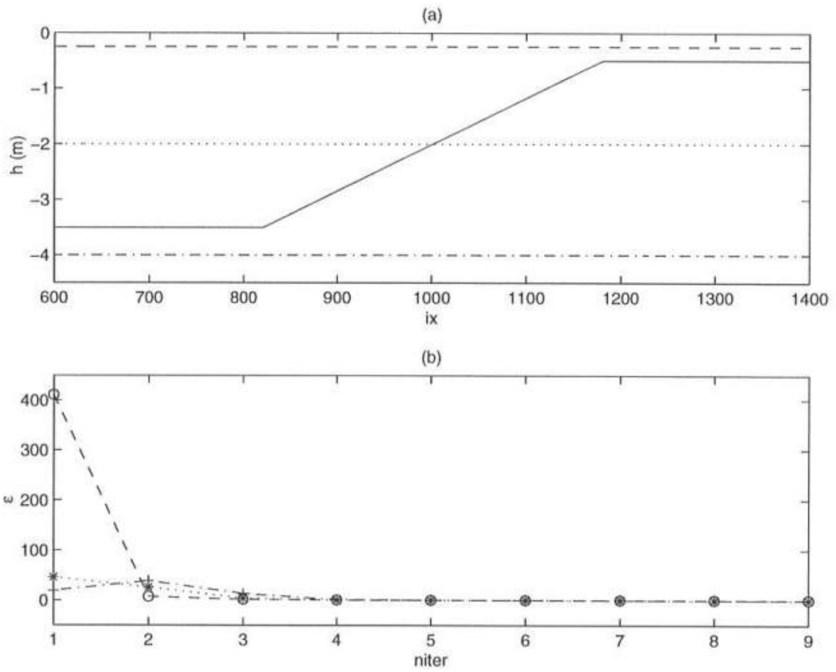

Figure 5.6: (a) Actual (–) and assumed depths for CASE IA : $h_{as}1(.)$, $h_{as}2(\text{-.})$, $h_{as}3(\text{- -})$. (b) Total velocity mismatch at successive iterations during inversion with the different assumed depths $h_{as}1(*)$, $h_{as}2(+)$ and $h_{as}3(\circ)$

respectively. An increased value of β seems to direct the depth iterates towards the true depth more quickly. However, the iteration has been observed to begin diverging at $\beta > 2.0$. For all the inversion cases, the shallowness parameter has been kept fixed at unity. A similar parameter was used by Kennedy *et al.* (1999) in their ratio of estimated and calculated phase speeds to update the estimated depths based on the phase speed mismatch.

The inversion methodology is based on the mismatch in velocities calculated from the mass and momentum inversion equations for an assumed depth. In the inversion case just discussed, the assumed depth (even though it was a flat bottom) was taken as an intermediate value between the minimum and maximum true depth

($h_{min} = 0.5m < h_0 = 2.0m < h_{max} = 3.5m$). The minimum and maximum values are not known a priori, and assuming an intermediate flat depth as the starting point for the inversion is thus impossible. Three different starting depths were considered, all of which were constant across the domain. In Figure 5.6 (a) are shown the three assumed depths along with the actual depth. The dashed line ($h_{as}3$) represents the assumed depth which was everywhere shallower than the actual depth, the dash-dot line ($h_0 2$) being deeper everywhere than the true depth and the dotted line ($h_0 1$) represents the case considered before. In the bottom panel is plotted the total velocity mismatch throughout the inversion for the different assumed starting depths. Except for the error at the first iteration of $h_0 1$ shown as circles (o), the convergence is uniform for all the three cases. This is evident from the depth and velocity estimates for inversion tests performed with the three different starting depths, shown in Figure 5.7. Only the velocity estimate from the mass equation (u_1) has been compared in the bottom panel. The estimated velocity from the momentum equation (u_2) is also independent of the starting depth. Any arbitrary depth can thus be used as a starting point for the inversion.

The same wave parameters used above for the linearized inversion, were used to simulate waves using the fully nonlinear equations in FUNWAVE ($\gamma = 1$). Surface images were saved 2 seconds apart and used to calculate phase speeds and estimate depths based on the fully nonlinear inversion equations. The model parameters remained the same. Figure 5.8 (a) shows the surface elevation maps, the dashed line being the first image, and the solid line being the image 2 seconds later. The effect of nonlinearity in the model equations can be seen in the modulation of the wave in the shallower flat region because of the interaction between the primary wave and the recurring harmonics. The wave shoals as it climbs up the slope and the nonlinear transformations modify the wave form. The bottom panel shows the actual and assumed depth. The linear analytic phase speed and the estimated phase

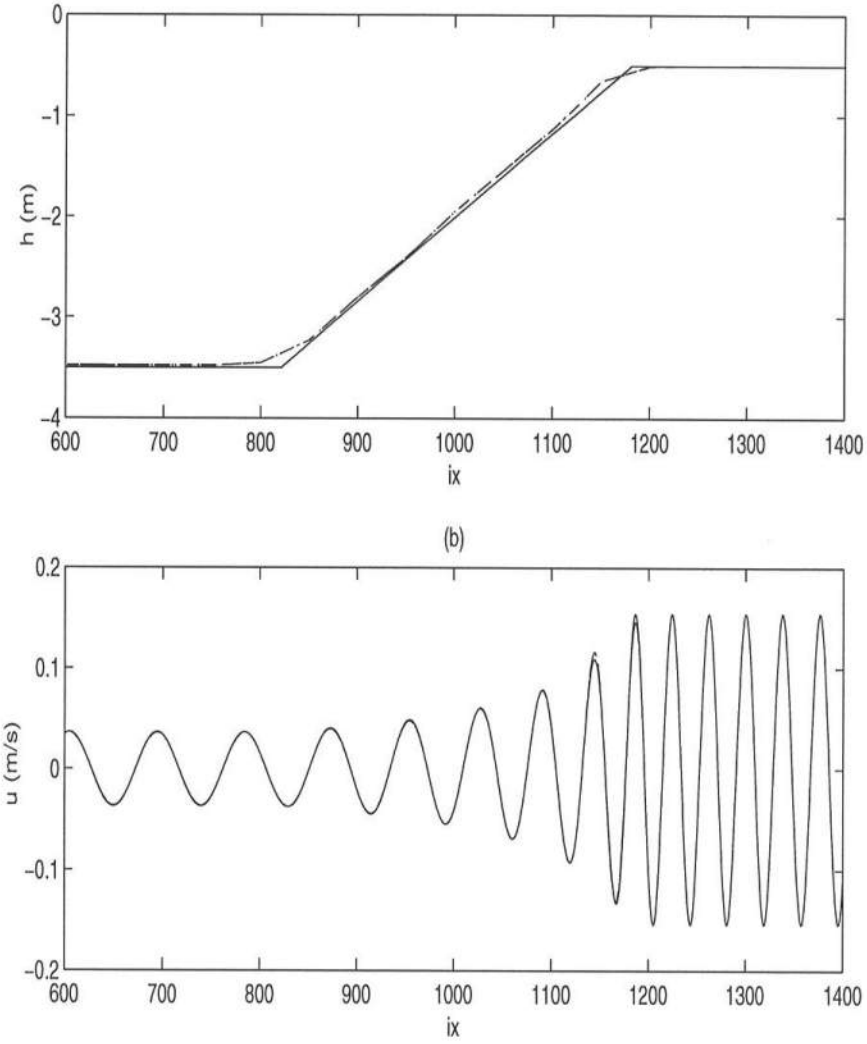

Figure 5.7: Actual (–) and estimated depths for CASE IA obtained with $h_0 1$(.), $h_0 2$(-.), $h_0 3$(- -). (b) Actual (–) and estimated velocities (u_1) with the different assumed depths

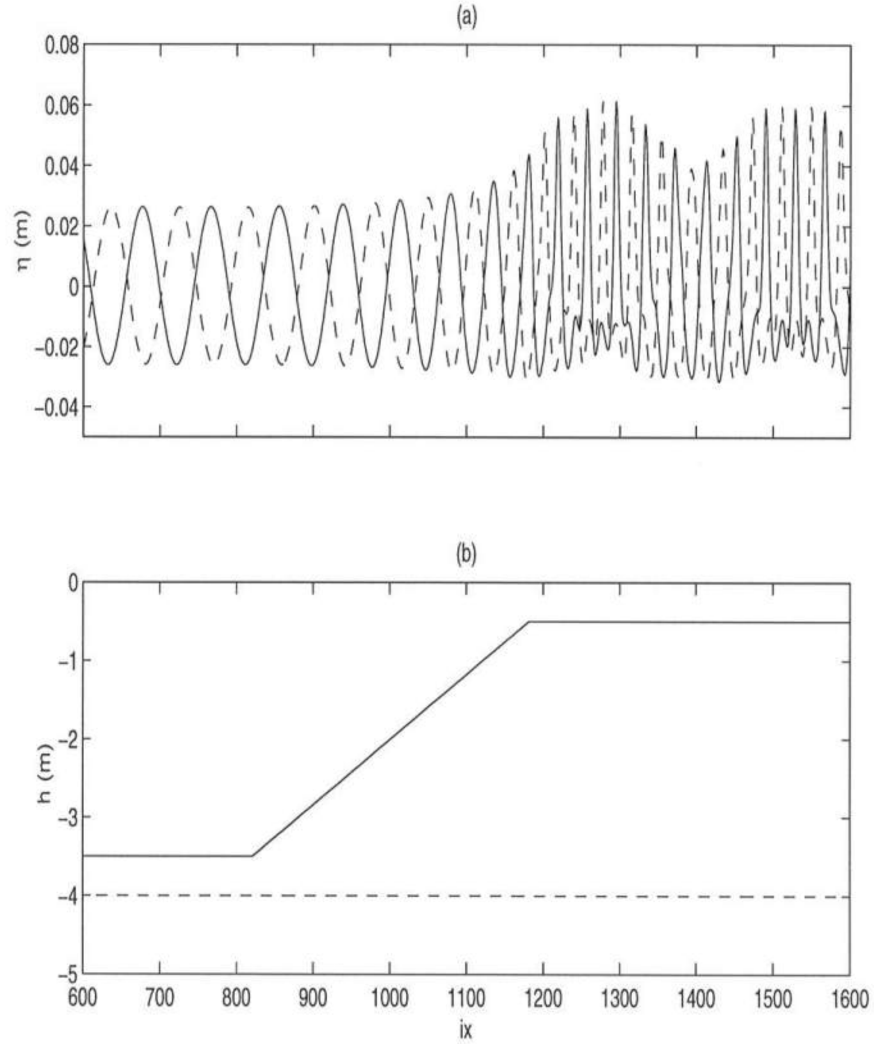

Figure 5.8: (a) Surface elevation images for CASE IA generated in FUNWAVE ($\gamma = 1$) (b) Actual (–) and assumed depth (- -)

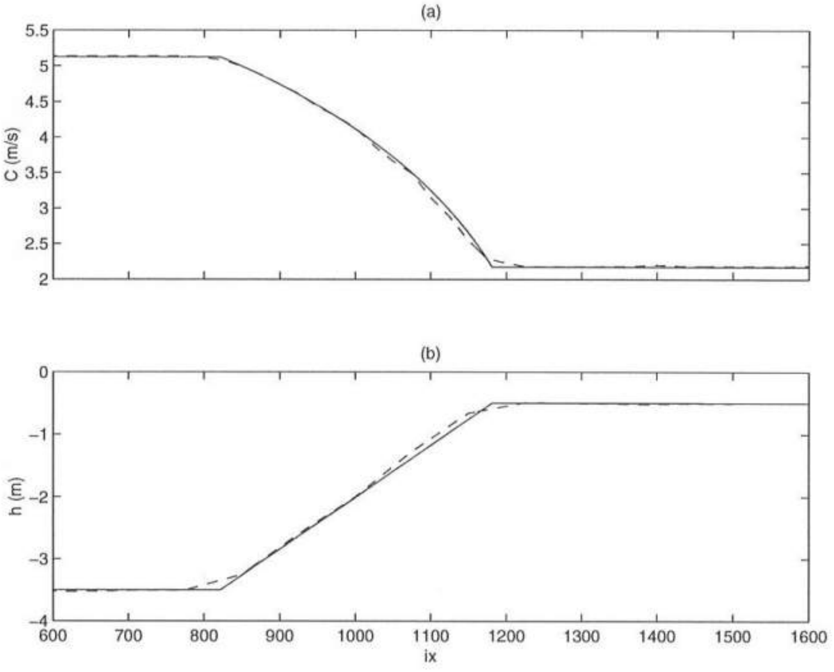

Figure 5.9: (a) Linear analytic (-) and estimated (- -) phase speeds. (b) Actual (–) and inverted (- -) depths.

speed are plotted in Figure 5.9 (a).

The window size was $W = 25m$, and the window shift was $ws = 6.25m$. The actual depth is seen to be estimated well by the fully nonlinear inversion, except at the toe and the shallower part of the slope. This error in the inverted depth can be explained as before by noting the discrepancies in the phase speed comparisons (Figure 5.9) and the velocity comparisons in Figure 5.11. The nonlinear inversion algorithm also converges very quickly within the first five iterations. The estimated depths at each iteration are shown in Figure 5.10 (b). Once the depth has converged, the corresponding particle velocities (at the final iteration) are evaluated from the nonlinear mass and momentum equations. The true and estimated velocities are plotted in Figure 5.11. The velocity from the mass equation is slightly overpredicted

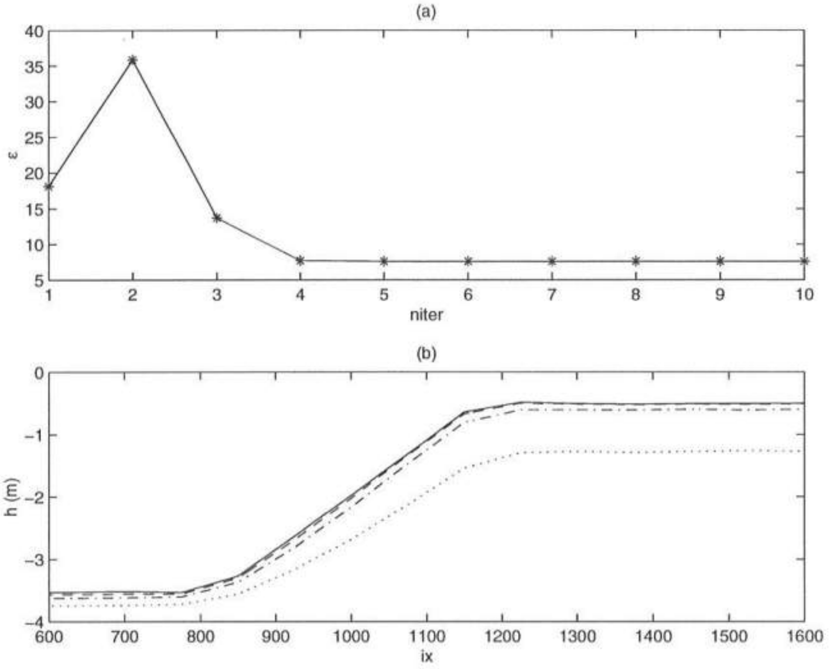

Figure 5.10: (a) Total velocity mismatch (ϵ) at successive iterations. (b) Inverted depth estimates at successive iterations : niter=1 (.), niter=2 (-.), niter=3 (- -), niter=5 (-)

and from the momentum equation slightly underpredicted in the shallower depths. This is due to the corresponding overprediction of phase speed, and which leads to an overprediction of depth at the shoreward toe of the slope.

To simulate groupy wave conditions, a time series generated from a TMA spectrum program was used as an input to FUNWAVE. The peak frequency ($f_p = \frac{1}{T_p}$) was 0.229 s^{-1}. The maximum frequency (f_{max}) was 0.40 s^{-1}. The significant wave height (H_s) was 0.05 m. The resulting time series and spectra are shown in Figure 5.12.

Two images were taken at $it1 = 30125$ and $it2 = 30175$ and are shown in the top panel in Figure 5.13. The images were generated in FUNWAVE with

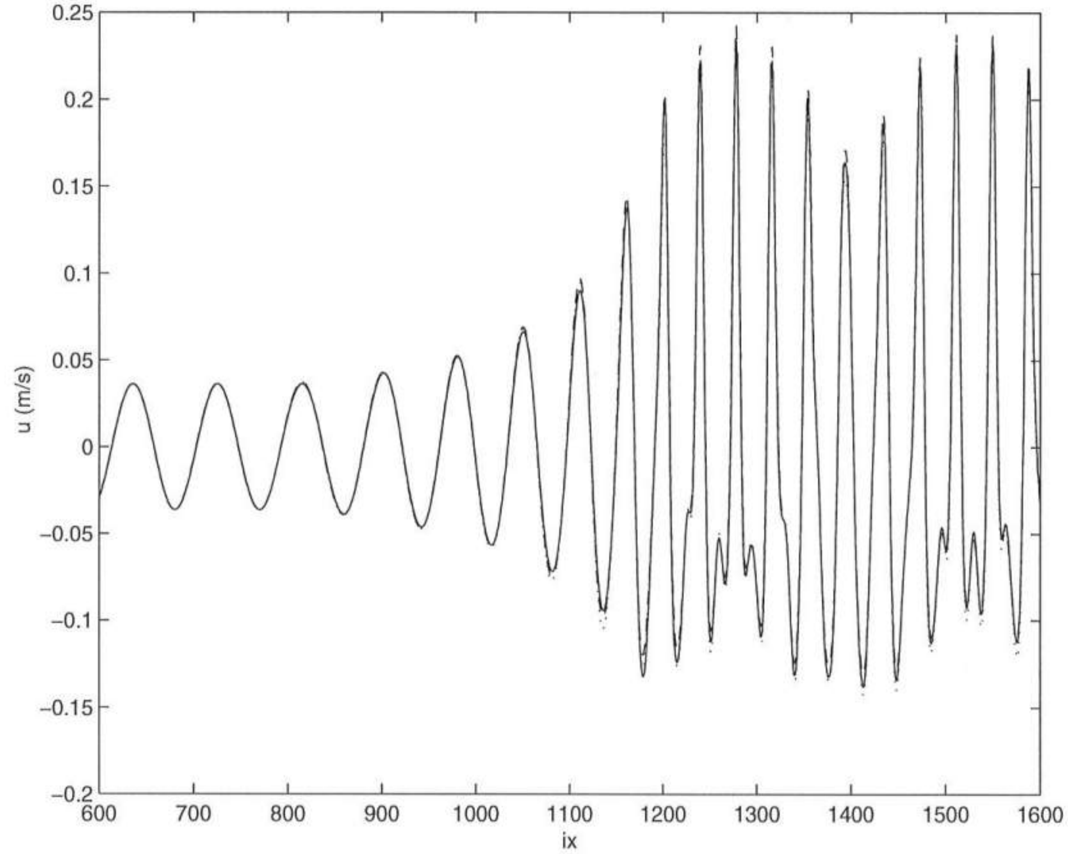

Figure 5.11: Actual(–) and estimated { $u_1(.)$, $u_2(\text{- -})$ } velocities for CASE IA with fully nonlinear inversion equations

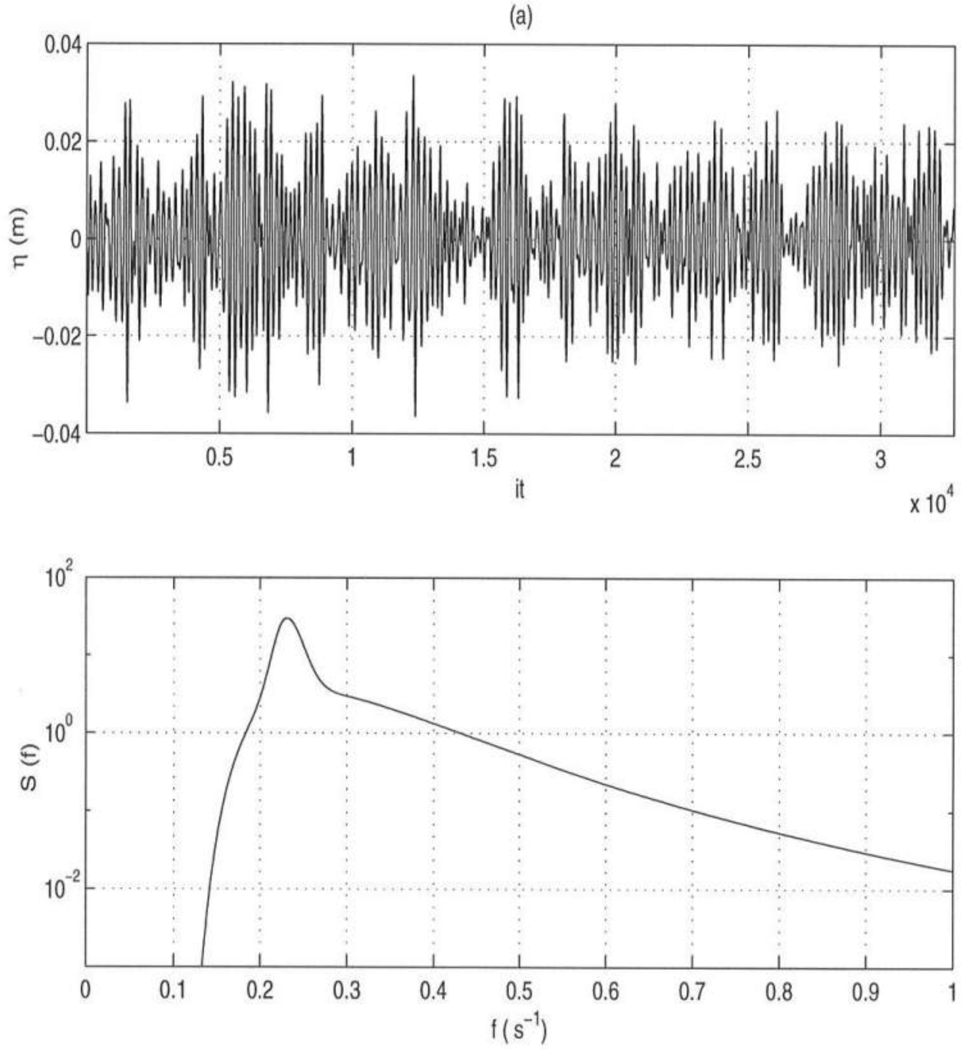

Figure 5.12: (a) Input time series in FUNWAVE, $\gamma = 0$ (b) Energy spectrum for the time series ($f_p = 0.229 s^{-1}$)

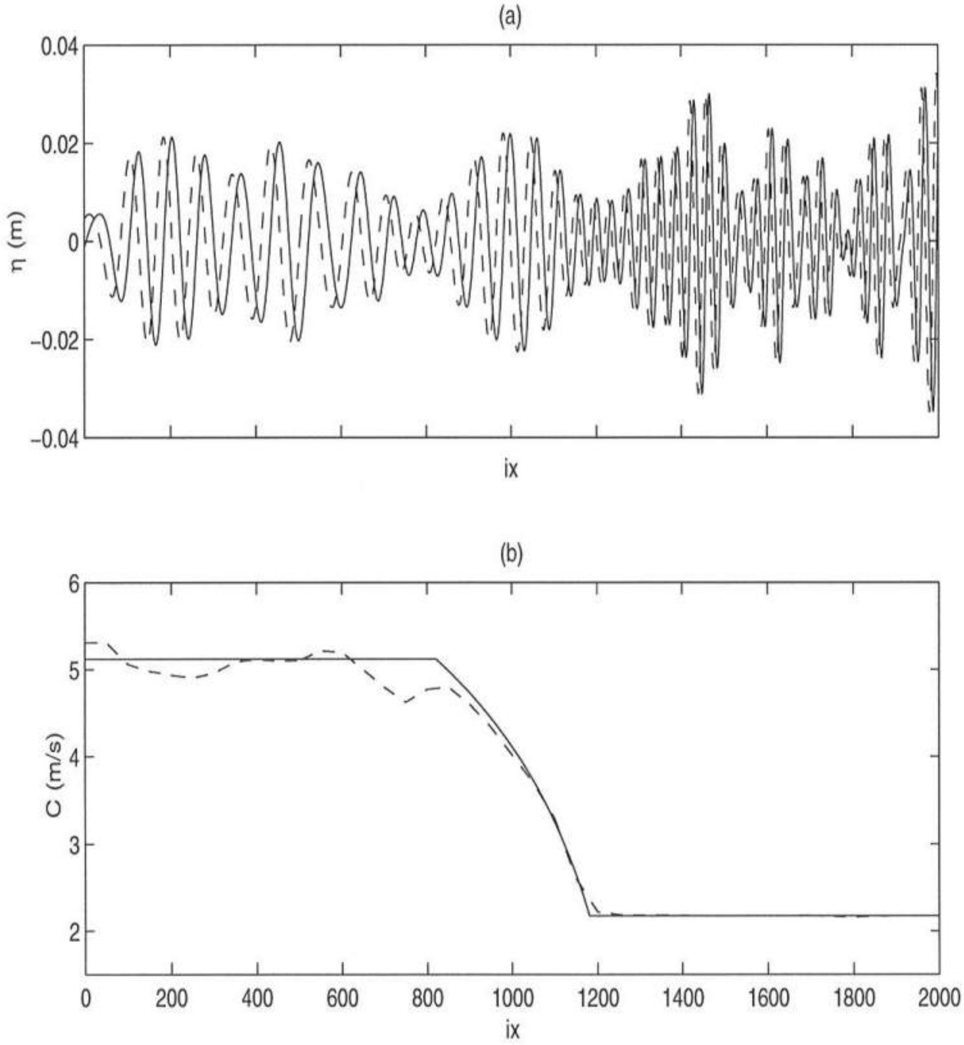

Figure 5.13: (a) Surface images generated in FUNWAVE from Nwogu's linearized equations (b) Linear analytic (-) and estimated (- -) phase speeds

Nwogu's linearized equations ($\gamma = 0$). The bottom panel shows a comparison of linear analytic and estimated phase speeds. It can be seen that in the deep water portion of the slope, the estimated speed deviates from the linear phase speed. There are several reasons for this discrepancy, which is related to the groupiness of the signal and is discussed in greater detail later. The phase speed and therefore the inverted depth estimate depend on the time instants the surface images are saved. Due to the incorrect representation of the phase speed by the least squares estimate, the final converged inverted depth (dashed line) as shown in Figure 5.14(a) also cannot predict the actual depth in deeper water. The estimates of particle velocities from the mass and momentum equations are however accurate and cannot be distinguished from the actual profile plotted in Figure 5.14 (b).

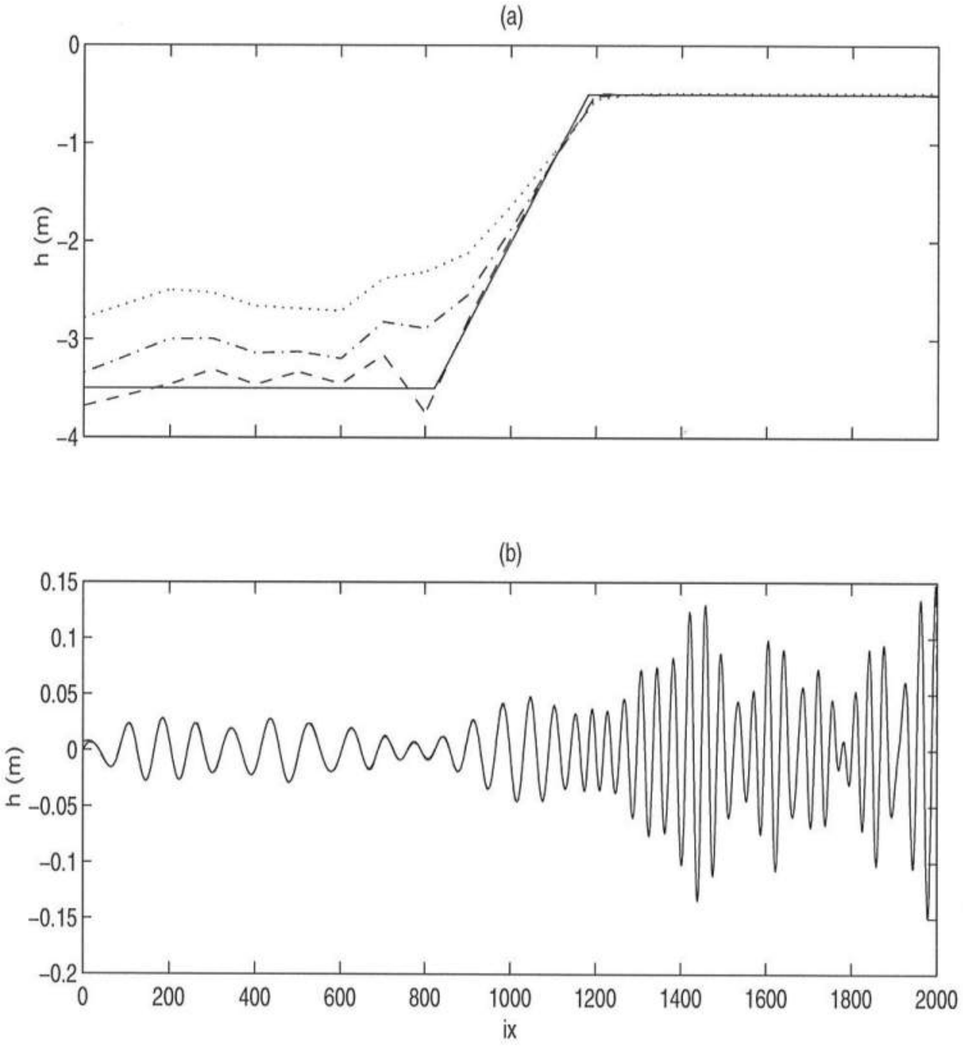

Figure 5.14: (a)Actual (–) and inverted depths from a single image : *niter*=1(.),*niter*=2(-.), Converged depth (–) (b)Actual(–) and estimated velocities ($u_1(.), u_2(--)$)

To investigate the effect of the groupiness of the signal on the errors in the phase speed estimate, the same time series as above was simulated in FUNWAVE to generate one hundred surface images. The first set of fifty images were saved at random time steps starting at $it_s = 20099$ and ending at $it_e = 29501$. There were thus fifty random images in a total time interval of 188.04 seconds. Each image in the second set of fifty images was collected one second after the corresponding image in the first set to simplify the phase speed calculation for each pair of images. The time interval between corresponding images in the two sets was thus constant at $\delta t = 1.0s$. The actual analytic depth and the assumed initial flat depth is shown in Figure 5.15(a).

The bottom panel shows the random time steps for the first set of images sorted in ascending order in time. Fifty estimates of phase speed were thus obtained from each pair of images and the results are shown in Figure 5.16. For each estimate of phase speed (from one pair of images), inverted depths were computed with both images of each pair. The depth estimates obtained from the first fifty images are shown in Figure 5.17 compared to the actual depth. It can be seen that all the inverted depths converge to the true depth in the shallower part, but are randomly distributed across the true value in the deeper portion of the depth and along the slope. The reasons for discrepancy in the deeper portion are discussed later. The inverted depths from the second set of fifty images are shown in Figure 5.18 and show the same features. The inverted depths obtained by averaging over the two sets of fifty estimated depths are plotted along with the true depth in Figure 5.19. The improvement in the predicted depth obtained by averaging can be seen by comparing the averaged depth to that obtained from a single image, as shown in Figure 5.20. It is expected that the error would decrease with an increased number of images considered for averaging. For irregular wave conditions also, a similar averaging would lead to better agreement with the actual depths and particle kinematics.

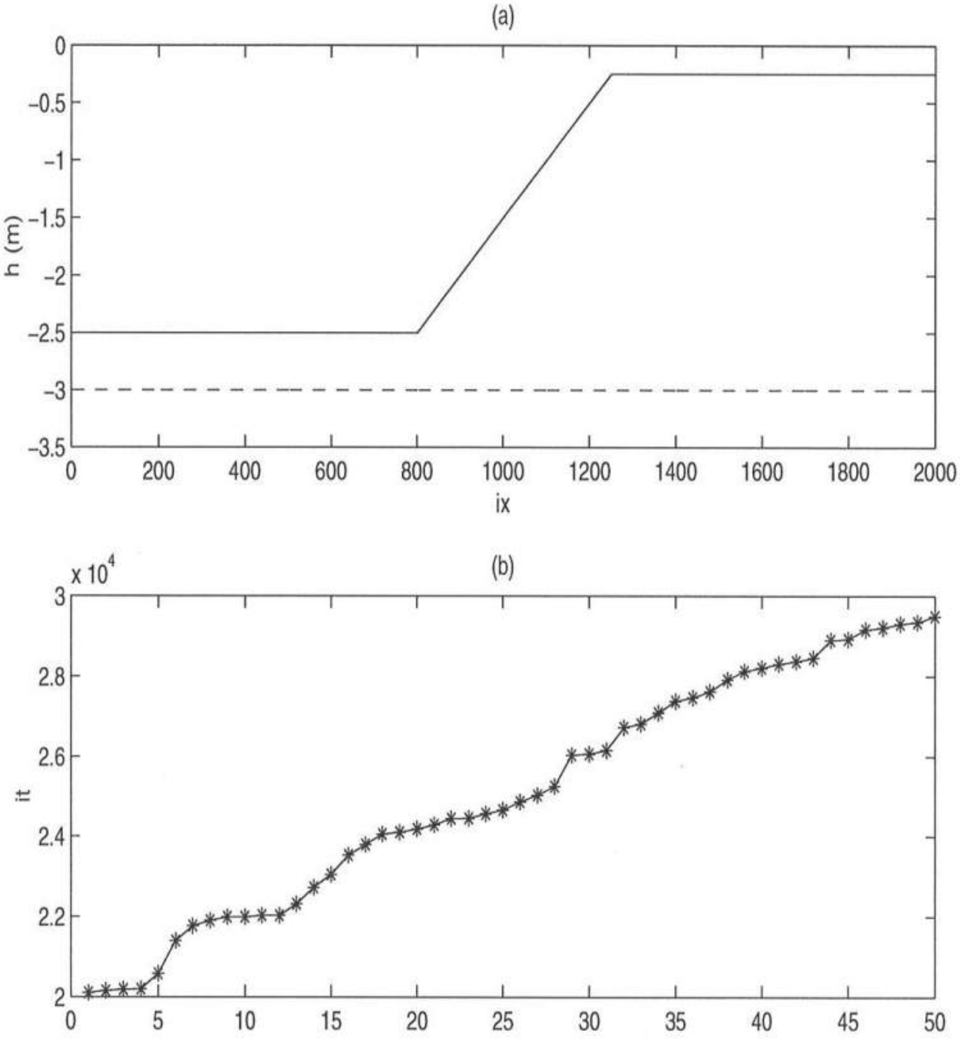

Figure 5.15: (a) Actual(–) and assumed initial depth(- -) (b) Random time steps used in FUNWAVE ($\gamma = 0$) to generate the first fifty images.

To explain the errors in the estimated phase speed, a simple wave group was numerically generated using two sinusoidal propagating wave forms with slightly differing wave frequencies. The carrier wave characteristics were $T = 4.369s$ and $H = 0.05m$. The wave group was allowed to propagate over different depths with $0.2317 \leq \mu \leq 4.225$, which ranged from shallow to deep water. Figure 5.21 shows three such wave groups. Two snapshots were taken of the propagating group for each case at a time interval $\delta t = \frac{T}{10}$ and the speed of each individual peak and crest in the wave form calculated by calculating the distance each peak or crest moves and then dividing that distance by δt.

Figure 5.22 shows the computed speed for each extremum in the wave group plotted along-with the carrier wave speed (solid line). The x-axis shows the surface elevation extremum number in the group. Consider the shallowest water group where $\mu = 0.797$ which is plotted in panel (a) in Figure 5.21. The first peak occurs at an extremum number $N = 1$ and the node in the wave group is close to $N = 10$ for this case. It can be seen from the dotted line in Figure 5.22, that as we approach the node of the wave group ($N = 10$) from either side, the estimated speed deviates from the carrier speed. This error is maximum close to the node, i.e, at $N = 10$ for the shallowest case and $N = 6$ for the deeper water case where the error is more than 20 % of the carrier speed. This is due to the modulation of the wave form which causes a slope in the wave envelope and which increases towards the node. Another point to note is that the error between the carrier phase speed and the computed value increases as we go from shallow to deeper water, which can be seen from the difference between the dotted and dashed lines from the corresponding solid lines in Figure 5.22. The error at the respective node increases from 7 % to 20 %. This explains the large and random errors in the estimated phase speeds seen in the groupy waves case (Figure 5.16) in the deeper part of the depth. Each time we evaluate the phase speed close to a node of the wave form, the estimate is in error.

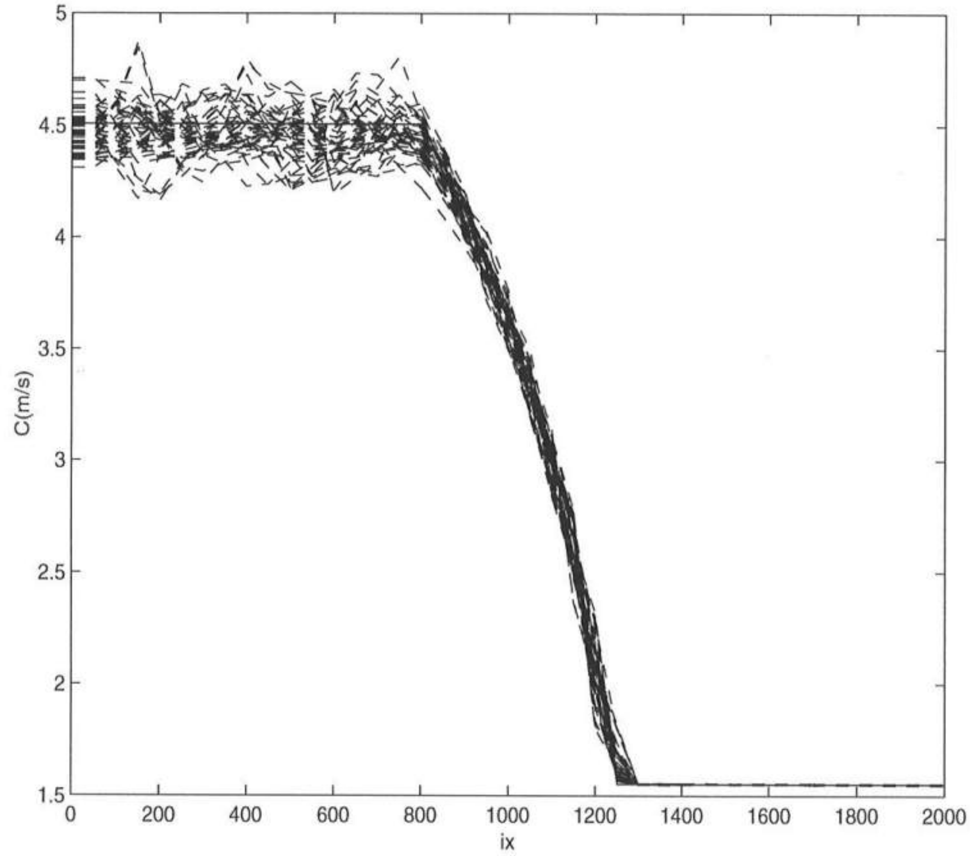

Figure 5.16: Linear analytic (–) and phase speeds estimated (- -) for each pair of images saved at the random time intervals

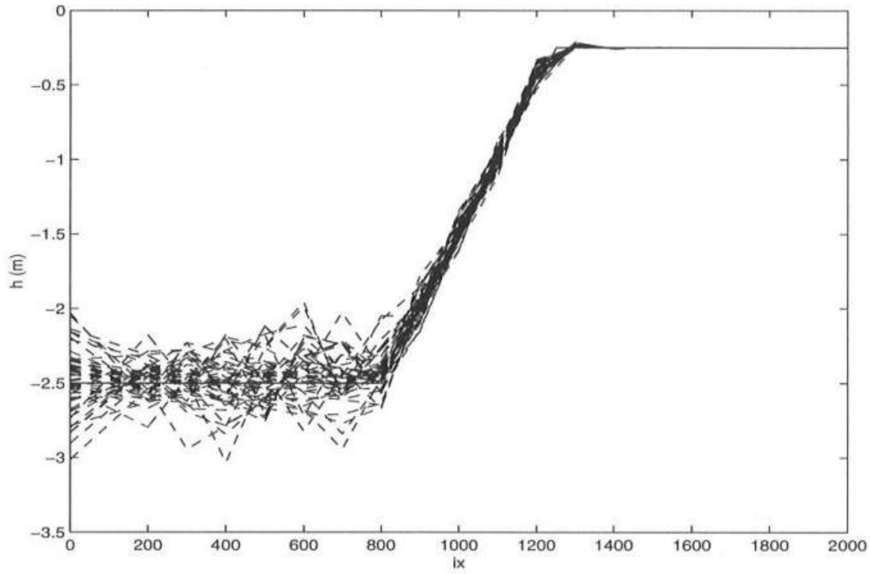

Figure 5.17: Actual(–) and estimated depths from the first set of fifty images

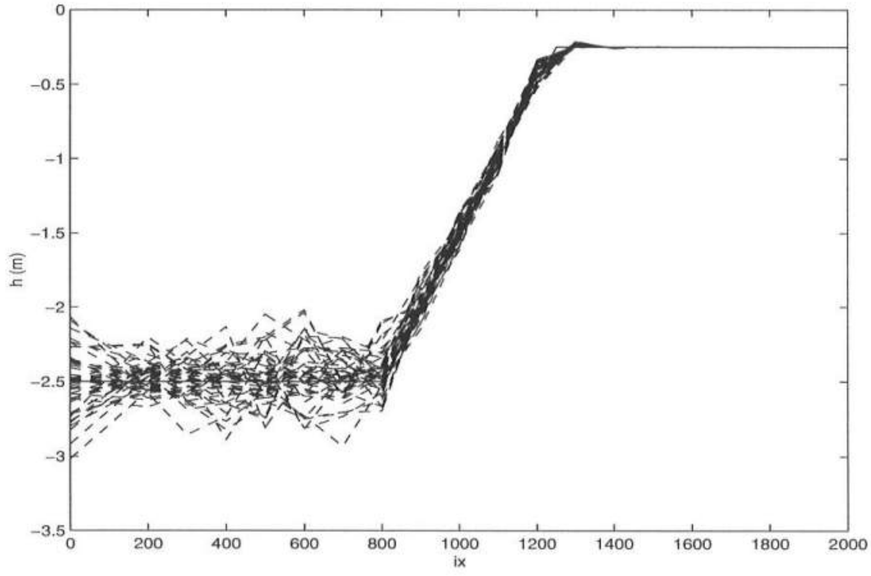

Figure 5.18: Actual(–) and estimated depths from the second set of fifty images

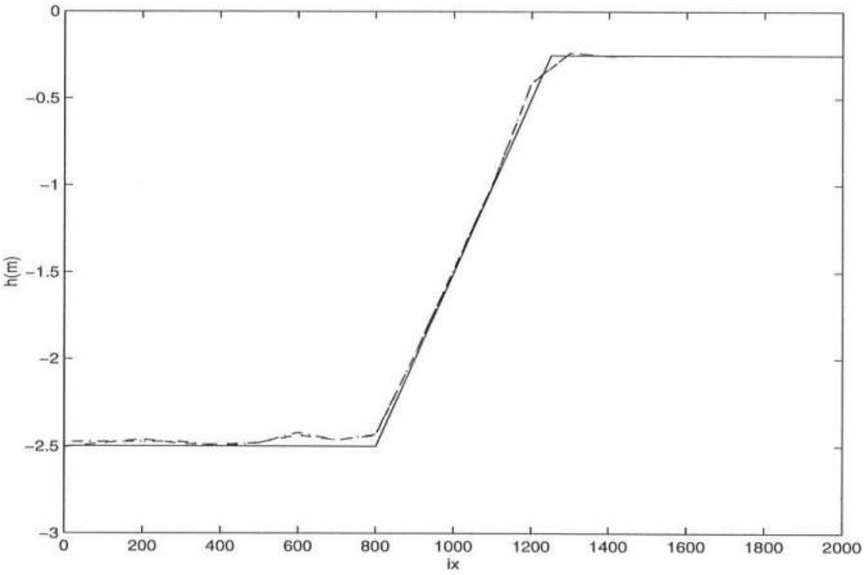

Figure 5.19: Actual(–) and estimated depth averaged over first set of images(-.) and estimated depth averaged over second set of images (–)

As demonstrated, this error can only be minimized by averaging over a large set of images. In the shallower part of the depth, the waves in the group are propagating at speeds independent of individual frequencies and are dependent only on the local water depth. The errors in the estimated phase speed are thus small.

5.1.2 With mean flows present in surface elevation data (CASE IB)

We now consider CASE IB, where mean flows were present in the input data (spatial maps of surface elevation) and where the integration constant were neglected in the inversion equations. This test case thus demonstrates the errors in the estimated phase speed and inverted depth by not accounting for mean flow effects during inversion. A constant volume flux ($q = 0.1m^3/s$) was specified. The resulting current and mean water level variations are shown in Figure 5.23. The current is constant over the flat regions of the slope and reaches its maximum value

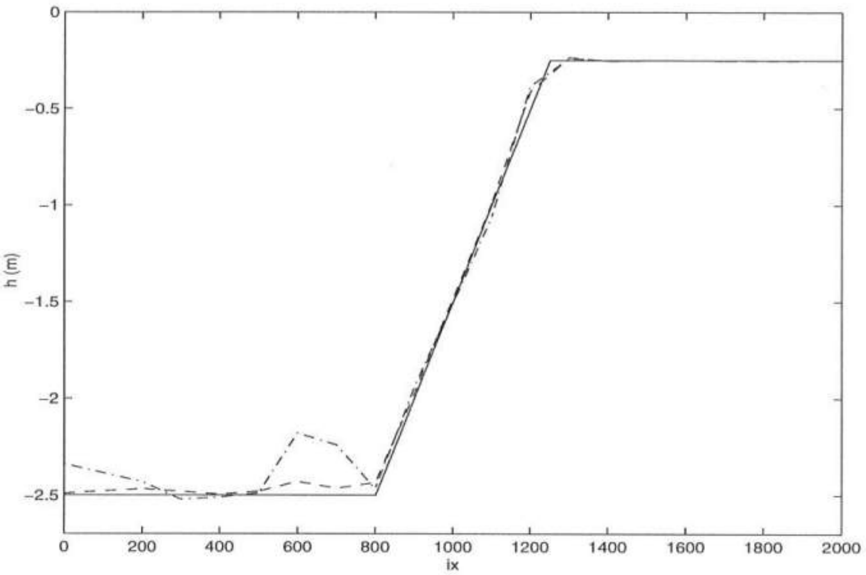

Figure 5.20: Actual(–) and estimated depths for a single image (-.) and averaged over a hundred images (- -)

at the shallowest depth. The mean water level variation is observed to be small (due to the weak current). Fully nonlinear extended equations were used to compute the wave images, all other model and depth parameters remaining the same as before for CASE IA. The surface images separated by $\delta t = 1.0s$ are shown in the top panel of Figure 5.24.

The effect of nonlinearity can be observed in the wave modulation over the shallower depth due to shoaling effects. The bottom panel shows the actual and starting inversion depth. The top panel in Figure 5.25 shows the analytic and estimated phase speed. Because of the following current, the phase speed is Doppler shifted and is everywhere larger than the true phase speed. The velocity estimates are also in error. This error translates to the inverted depth, shown in Figure 5.26. The error is seen to be larger in the shallower part because the current effect (magnitude) is also larger in that region of the depth. This error would thus increase

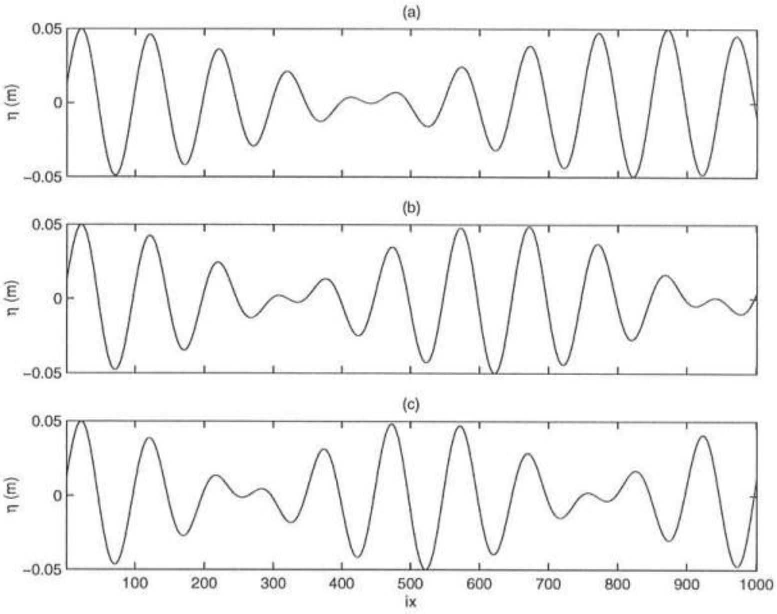

Figure 5.21: Wave envelopes in (a) $\mu = 0.797$ (b) $\mu = 1.693$ (c) $\mu = 3.698$

for stronger currents. Given only surface elevation data, it is not possible to obtain the current variation across the domain. The present inversion method thus cannot account for mean flows with only surface elevation data, and at present no unambiguous modifications can be suggested for CASE IB to improve depth predictions.

5.2 Inversion with velocity data (CASE II)

Similar to storing spatial maps of surface elevation generated in FUNWAVE at specified time steps, time lagged snapshots of particle velocity can also be used as inversion data. We distinguish two cases - CASE IIA, when there were no mean flows present in the data, and CASE IIB, when the velocity maps had prescribed mean flows in them. We first compare results for CASE IIA.

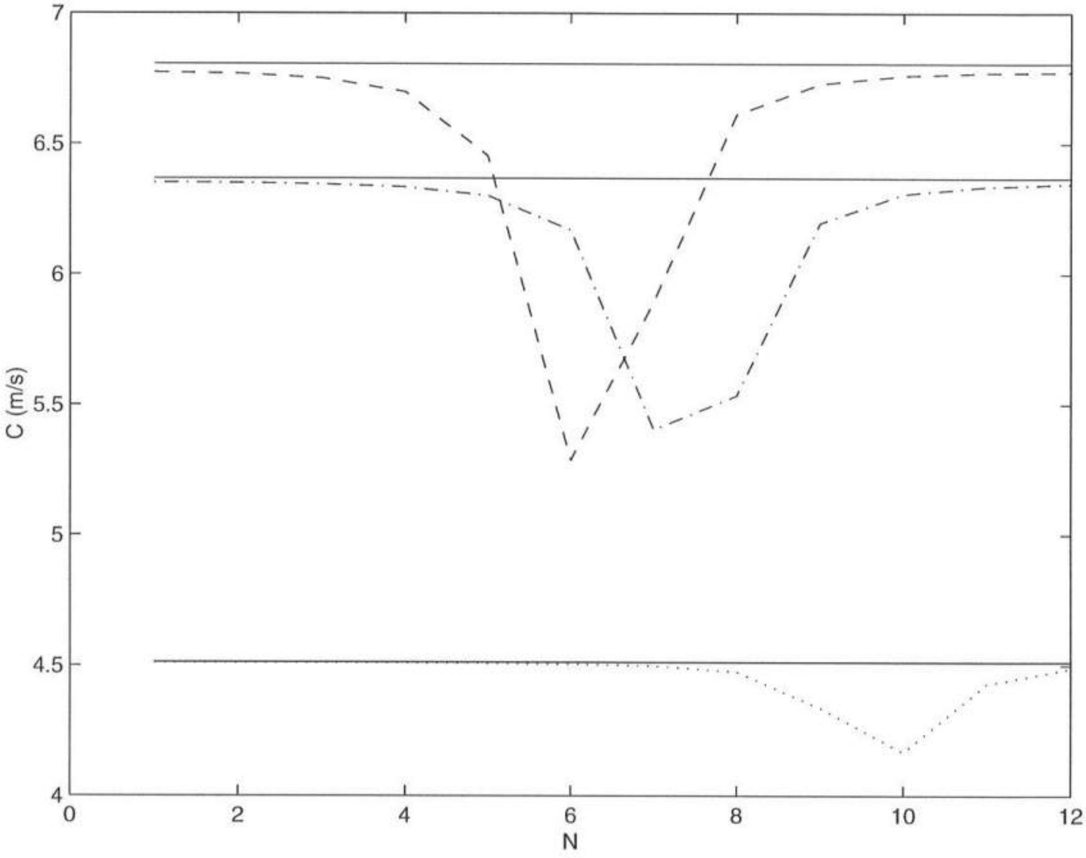

Figure 5.22: Carrier phase speed (-) and speed of crest movement for $\mu = 0.797$ (.) $\mu = 1.693$ (-.) $\mu = 3.698$ (- -)

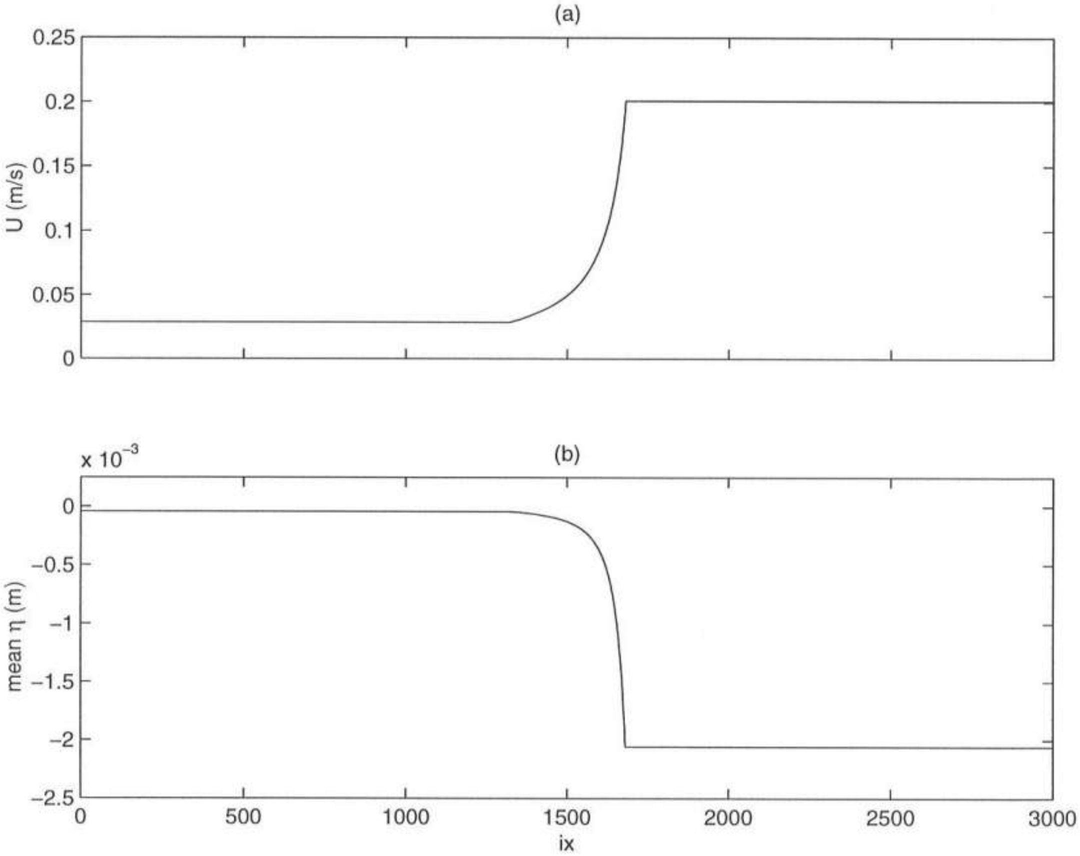

Figure 5.23: (a) Initial current profile specified in FUNWAVE, $\gamma = 1$ (b) Mean water level variation across the domain due to the current

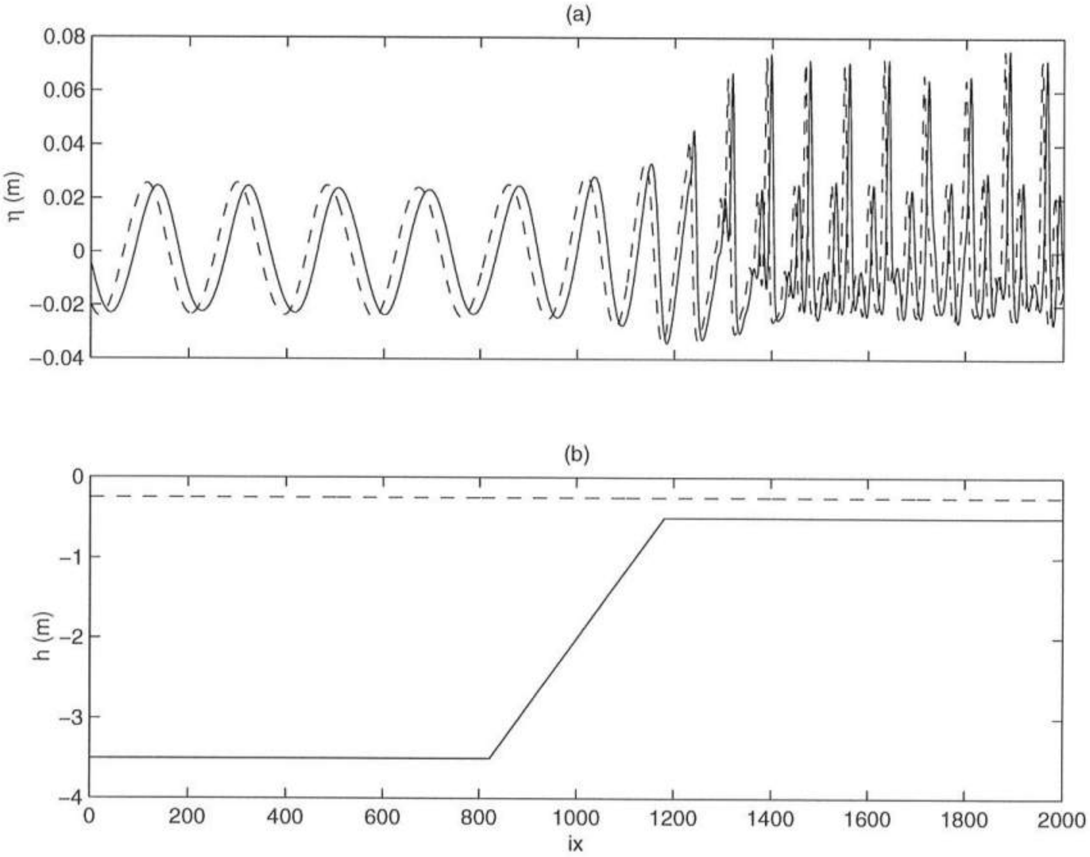

Figure 5.24: (a) Wave surface elevation snapshots for CASE IB generated in FUNWAVE with $q = 0.1m^3/s$ and $\gamma = 1$ (b) Actual (–) and assumed (- -) starting inversion depth

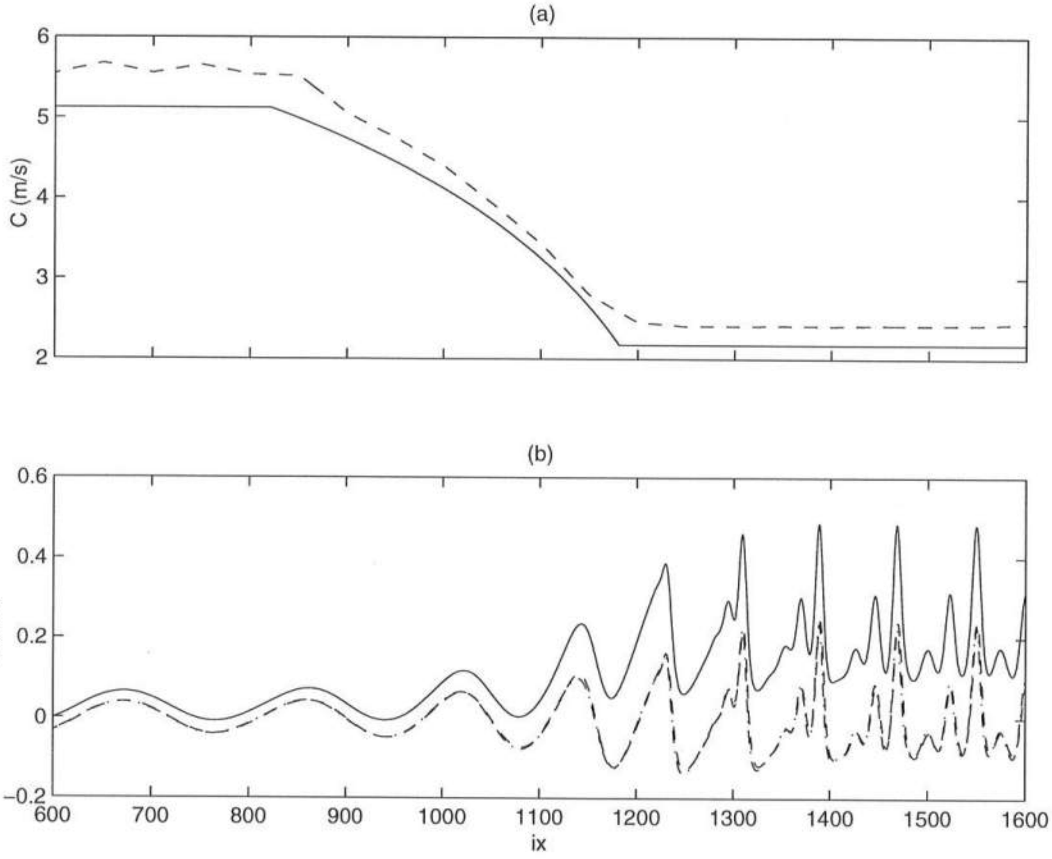

Figure 5.25: (a) Linear analytic (-) and estimated phase speed for CASE IB (b) Actual (–) and estimated velocities for CASE IB ($u_1(-.)$, $u_2(--)$)

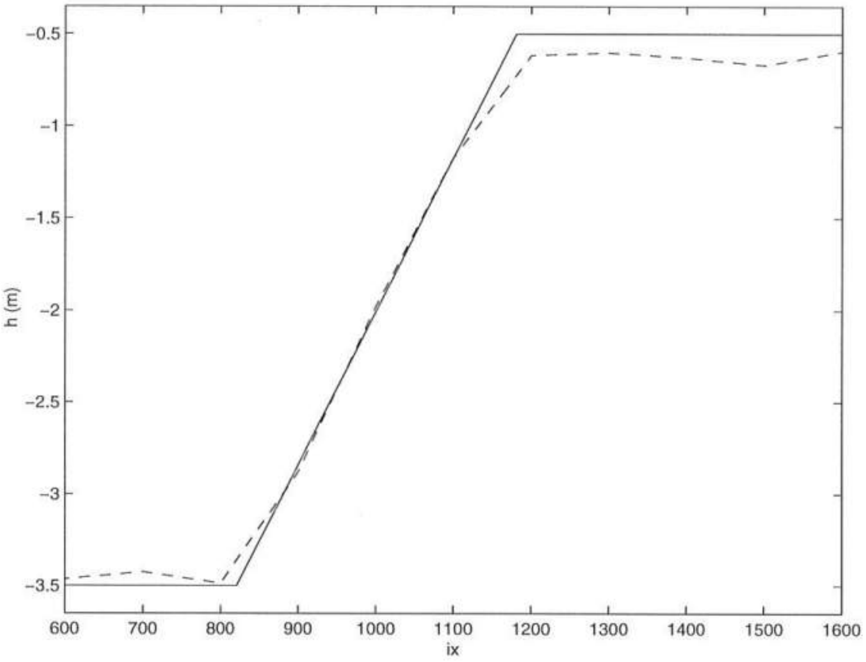

Figure 5.26: Actual (–) and inverted depth (- -) for CASE IB

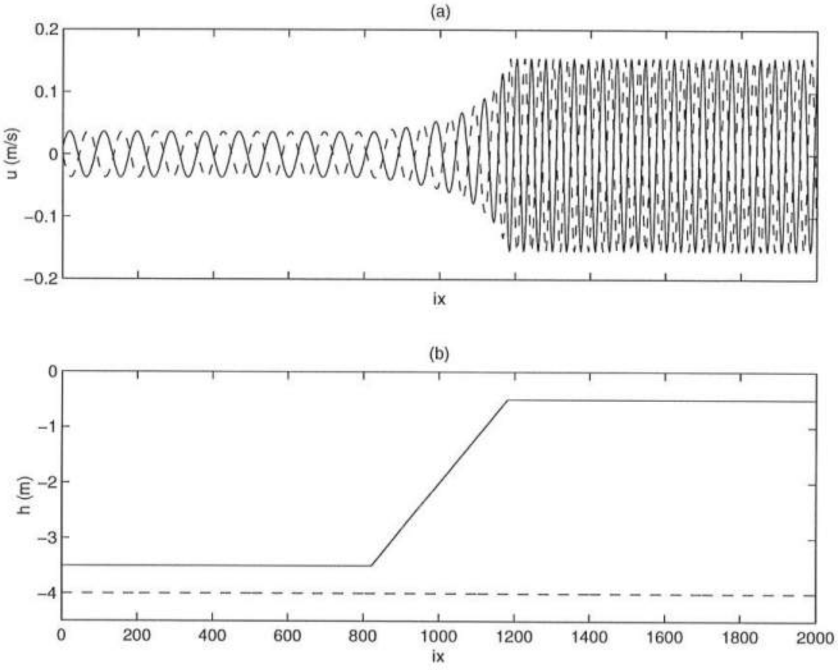

Figure 5.27: (a) Velocity maps generated in FUNWAVE ($\gamma = 0$ for CASE IIA (b)Actual (–) and assumed depth (- -)

5.2.1 No prescribed mean flows in particle velocity data (CASE IIA)

Using the linearized time dependent Nwogu's equations in FUNWAVE ($\gamma = 0$) velocity maps were saved at $it5 = 30000$ and $it6 = 30100$ which meant a time lag of $\delta t = 2.0s$. All the other wave, model and bottom parameters remained as in CASE IA ($H = 0.05m, T = 4.369s$). The velocity images are shown in Figure 5.27 (a), where the dashed line is the first image in time. The assumed and actual depths are shown in the bottom panel.

The linear analytic phase speed is compared to the least squares estimate in Figure 5.28 (b). The window size was $W = 25m$ and the spatial shift for the window was $ws = 12.5$. The estimate matches the analytic values accurately except at the seaward and onshore toes of the slope due to the large window size. The

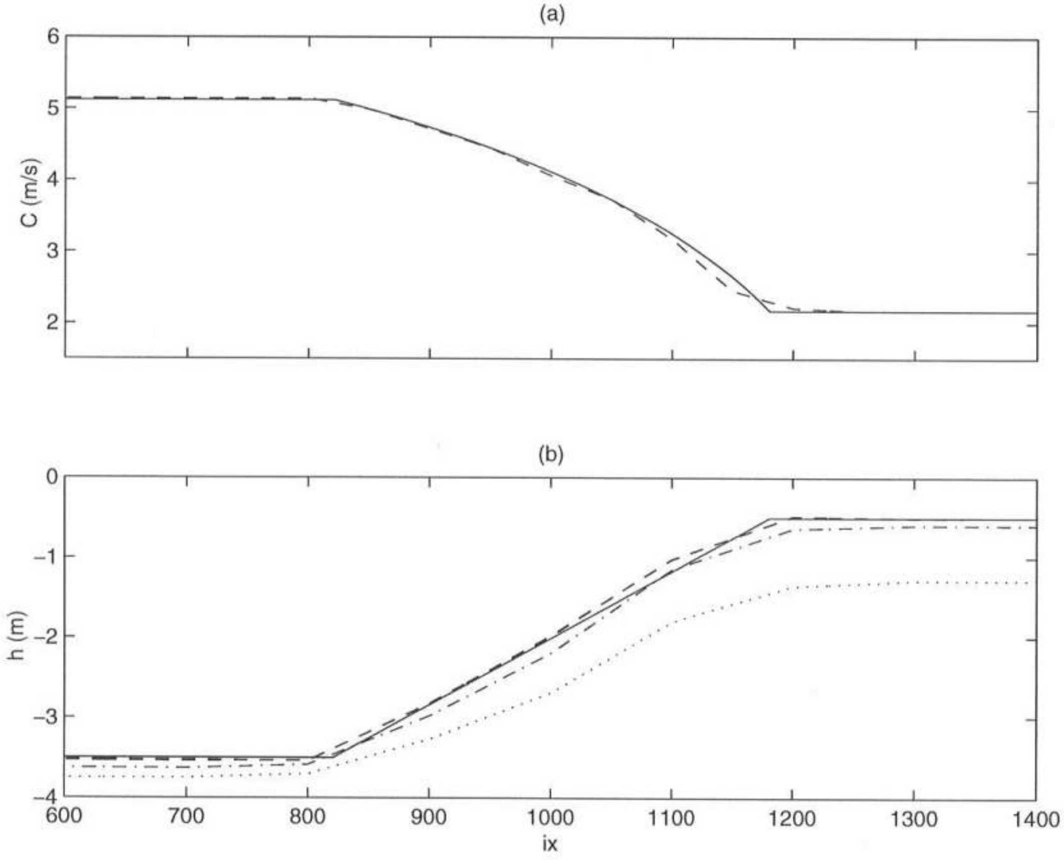

Figure 5.28: (a) Linear analytic (-) and estimated phase speed. (b) Actual (–) and inverted depths at $niter = 1$ (.), $niter = 3$ (-.), $niter = 5$ (- -)

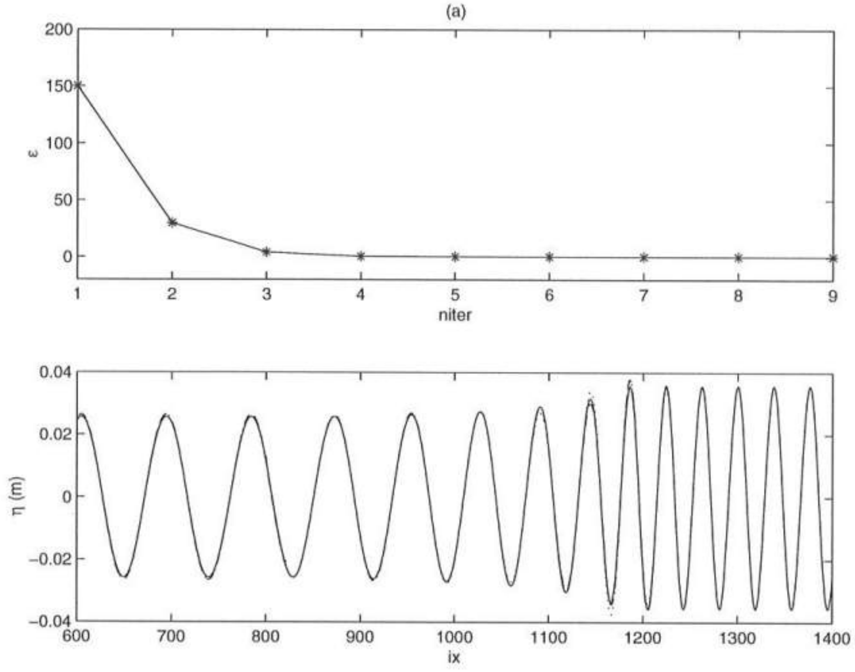

Figure 5.29: (a)Total surface elevation mismatch (ϵ) at different iterations (*niter*) for linearized inversion. (b)Actual (–) and estimated surface elevation $\{\eta_1(.), \eta_2(--)\}$

bottom panel shows the inverted depth estimates at different iterations, where the final converged inverted depth is shown as the dashed line. The dotted line is the shallow water estimate and the solid line is the true depth.

As can be seen from Figure 5.29 (a), convergence is uniform and fast, as the total surface elevation mismatch decreases to a constant minimum value in about five iterations. The maximum number of iterations here was also fixed arbitrarily as 9. The bottom panel shows the true surface elevation as obtained from FUNWAVE (solid line), plotted along with the estimates from the mass equation (η_1 (dotted line)) and the momentum equation (η_2 (dashed line)). Wherever the estimated phase speed is greater than the true celerity, $\eta_1 < \eta_2$ and vice versa. This is obvious

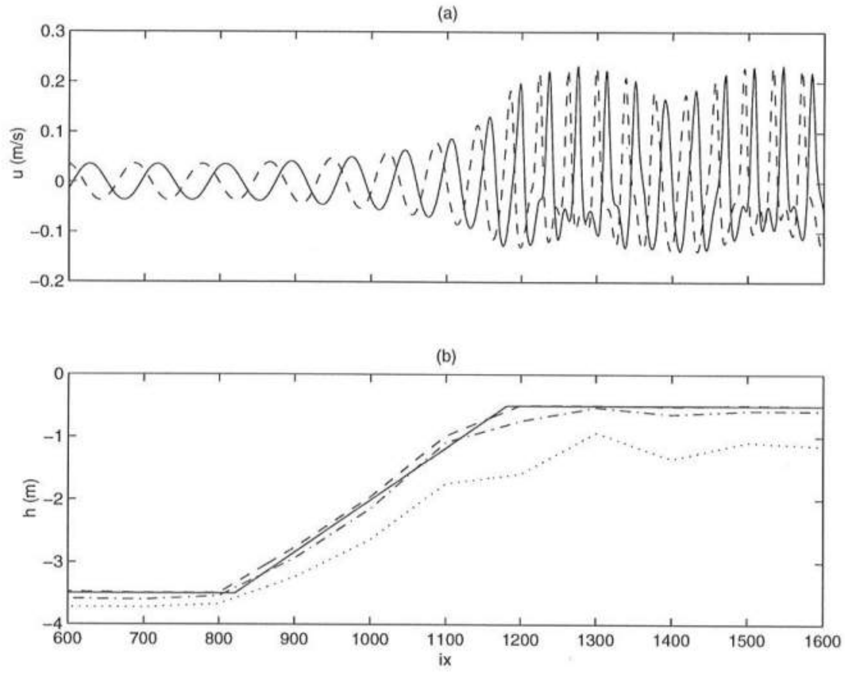

Figure 5.30: (a)Velocity data obtained from FUNWAVE ($\gamma = 1$ for CASE IIA. (b)Actual (–) and inverted depth estimates $niter = 1$ (.), $niter = 3$ (-.), $niter = 5$ (- -) using fully nonlinear inversion equations.

by looking at (4.1-4.2). Due to this error in the surface elevation estimates, the inverted depth is also smaller than the true depth in over the plane slope, which can be explained by looking at (4.7) where the estimated depth is seen to be directly proportional to η_2 and inversely proportional to η_1.

The same monochromatic wave form was simulated in FUNWAVE with the same depth but with the fully nonlinear time dependent extended Boussinesq equations ($\gamma = 1$). The velocity images saved at lagged time intervals are shown in the top panel of Figure 5.30. As the wave shoals up the slope, nonlinear interactions between the primary wave component and its harmonics modulates the wave, which can be seen in the velocity profile over the shallower flat part of the slope.

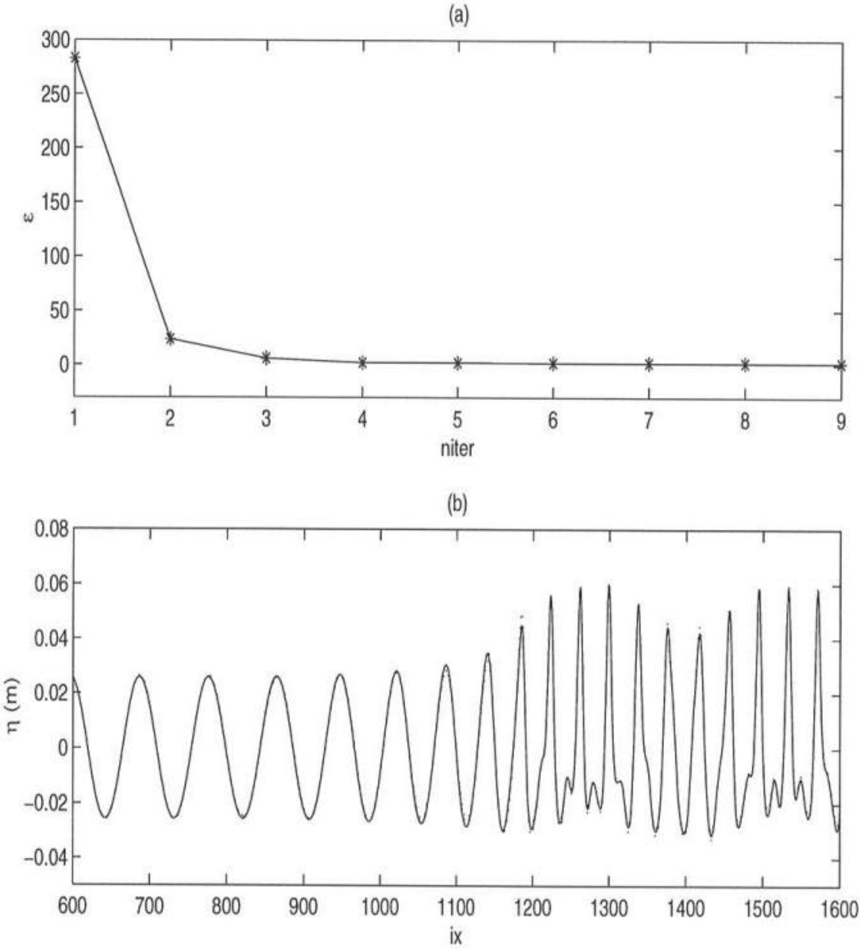

Figure 5.31: (a)Total surface elevation mismatch (ϵ) at different iterations ($niter$). (b)Actual (–) and estimated surface elevation $\{\eta_1(.), \eta_2(--)\}$ for fully nonlinear test

An assumed flat depth of $0.25m$ was fixed as a starting point for inversion with the fully nonlinear equations. The inversion estimates are shown in the bottom panel. The true depth is reasonably well recovered by the inversion, and the inverted depth is accurate over the shallower part of the bathymetry. Even with the fully nonlinear inversion equations, the depth iterates and estimated surface elevation converge quickly, within five to six iterations (See Figure 5.31). The estimated surface elevation matches well with the true values.

5.2.2 With mean flows present in particle velocity data (CASE IIB)

As before in CASE IIA, mean flows were prescribed in FUNWAVE by a constant volume flux ($q = 0.2m^3/s$) across the domain. The resulting current and mean water level variations are shown in Figure 5.32. The current is weak enough to neglect the mean water level variations in the fully nonlinear inversion equations. The current and mean water level depression increases as the depth becomes shallower, reaching a constant maximum over the flat shallow part of the depth.

Fully nonlinear equations were used in FUNWAVE to generate the velocity maps shown in Figure 5.33(a). The increased values of the velocity due to the following current can be seen by the positive shift in the entire velocity profile. The phase speed estimate (dashed line) is also Doppler shifted by the current and leads to an increase due to the following current.

The depth inversion can be done using this Doppler shifted phase speed estimate with both the linearized and fully nonlinear inversion equations. The inverted depth using the linearized equations is shown as the dash-dot line in Figure 5.34. The dashed line is the inverted depth from the fully nonlinear equations and the solid line is the true depth. As expected both estimates are in error because the integration constants were neglected.

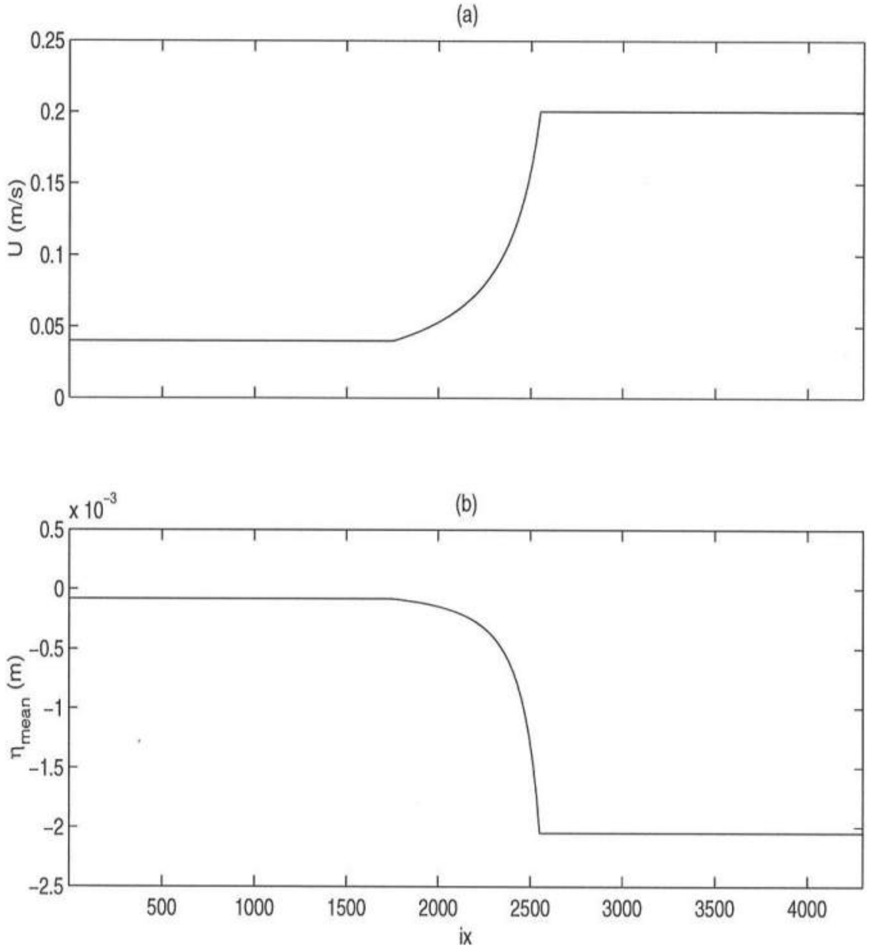

Figure 5.32: (a)Initial current variation specified in FUNWAVE ($\gamma = 1, q = 0.2m^3/s$) for CASE IIB. (b)Mean water level variation across the domain

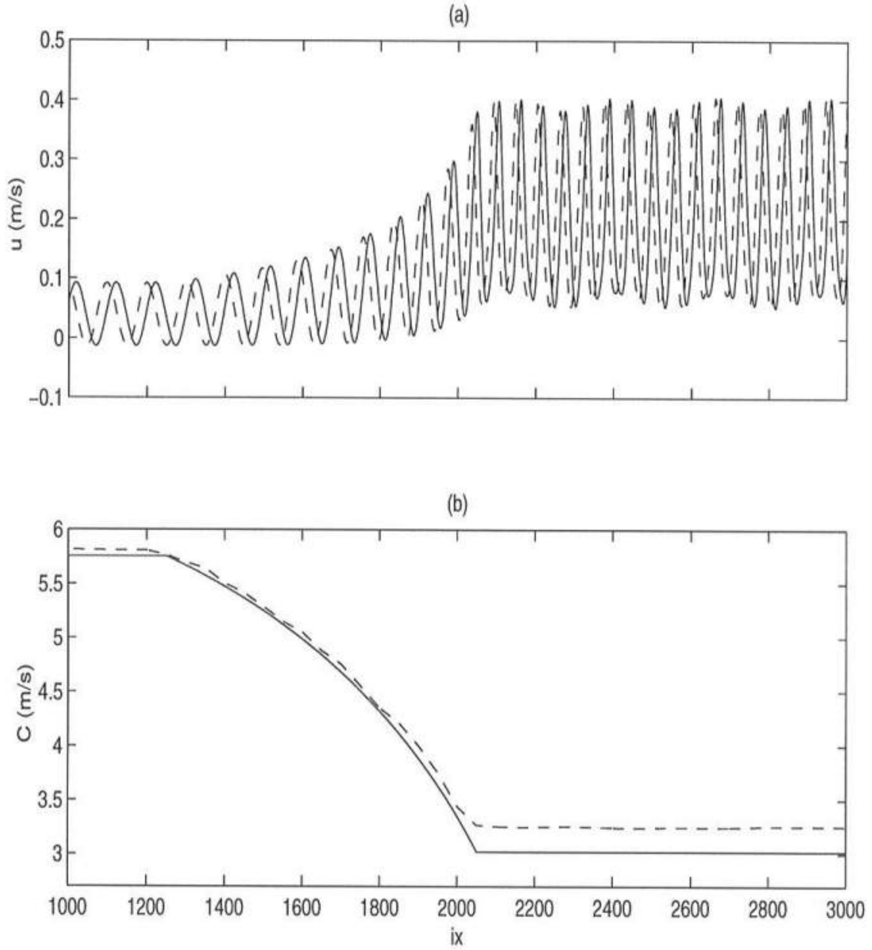

Figure 5.33: (a)Total velocity maps generated in FUNWAVE ($\gamma = 1, q = 0.2m^3/s$) (b)Linear analytic (–) and estimated (- -) phase speed.

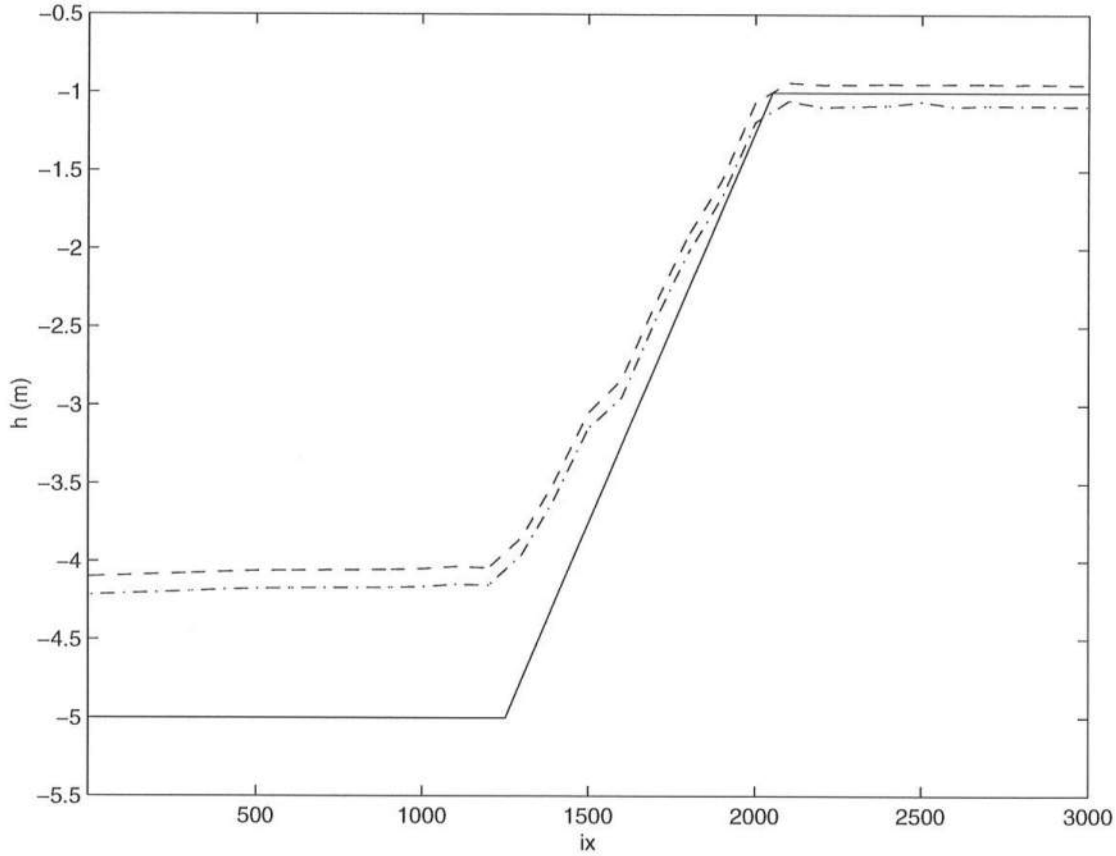

Figure 5.34: Actual (–) and estimated inverted depths with total velocity and Doppler shifted phase speed. Linearized inversion equations (-.), Fully nonlinear inversion equations (- -)

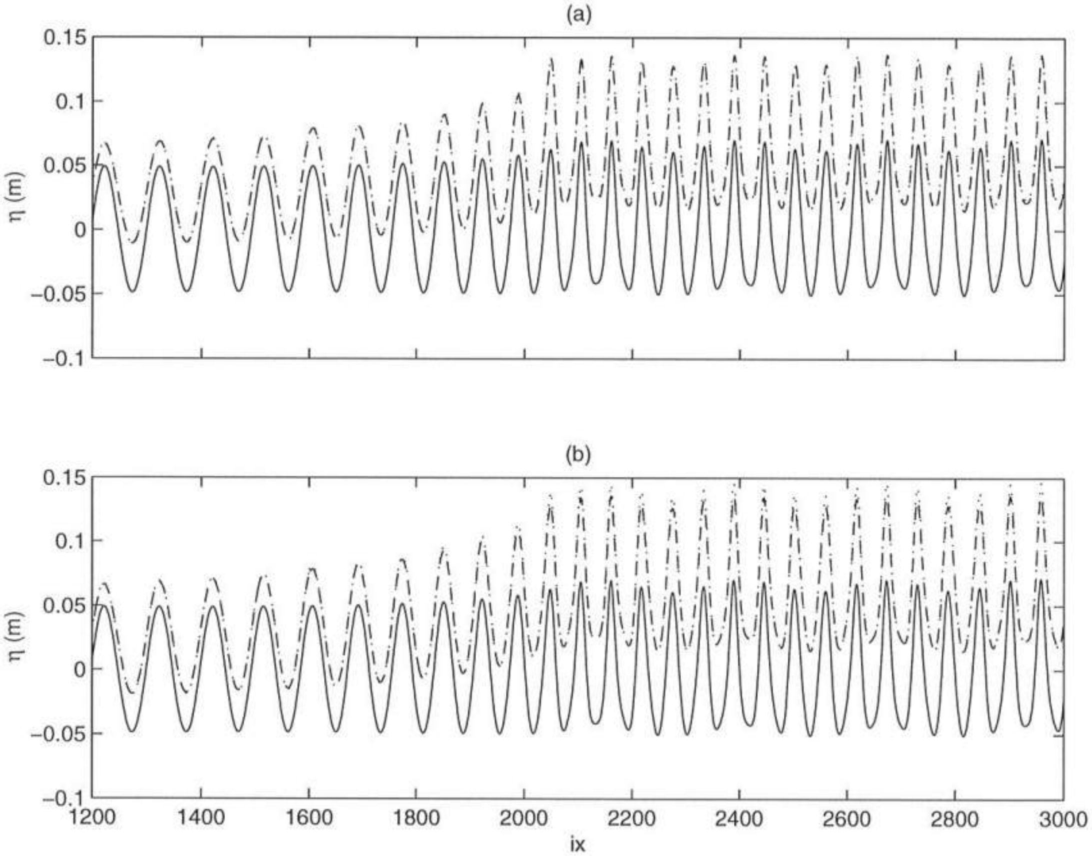

Figure 5.35: (a)Actual (–) and estimated surface elevation from the mass equation - Linearized inversion (.), Fully nonlinear inversion (- -). (b)Actual (–) and estimated surface elevation from the momentum equation - Linearized inversion (.), Fully nonlinear inversion (- -)

Figure 5.35 (a) shows the surface elevation estimate (η_1) from the linearized mass equation (dotted line) and fully nonlinear mass equation (dashed line). The solid line is the actual value. The bottom panel shows similar estimates from the linearized and fully nonlinear momentum inversion equations. All the estimates are in error due to the presence of mean flows. Because of the linear nature of the wave and since the fully nonlinear equations here do not take into account the effect of currents, both the estimates (from the linearized and fully nonlinear equations) are almost the same though consistently in error from the true value.

We now calculate the pure wave part of the velocity data to account for mean flows in the inversion. The current profile is obtained by locally averaging over the total velocity map and is compared to the prescribed current in Figure 5.36 (a). On subtracting this current from the total velocity (u) profile we get the pure wave part of the velocity (u_w), which is shown as the solid line in Figure 5.36(b). The dashed line is the total velocity with the mean flow in it. The Doppler shift in the phase speed is also corrected for by subtracting this current from the computed phase speed (C). The corrected phase speed is denoted as before as C_0.

Figure 5.37 shows the total surface elevation mismatch (ϵ) at each inversion iteration for three separate inversion cases. The first inversion is done with the total velocity (u) and computed Doppler shifted celerity (C), the second case is with the pure wave part of the velocity (u_w) and the computed Doppler shifted celerity and the third case is the inversion done with the pure wave part of the velocity and the corrected phase speed (C_0). The dotted line ($\circ$) shows the errors during the first inversion case. The dashed line ($+$) shows the errors during inversion with the pure wave part of the velocity and the Doppler shifted phase speed. The solid line shows convergence during the third inversion case. As is evident, the error decreases with each successive correction. The inversion thus has to take into account both the Doppler shifted velocity and the phase speed. The corresponding inverted depths

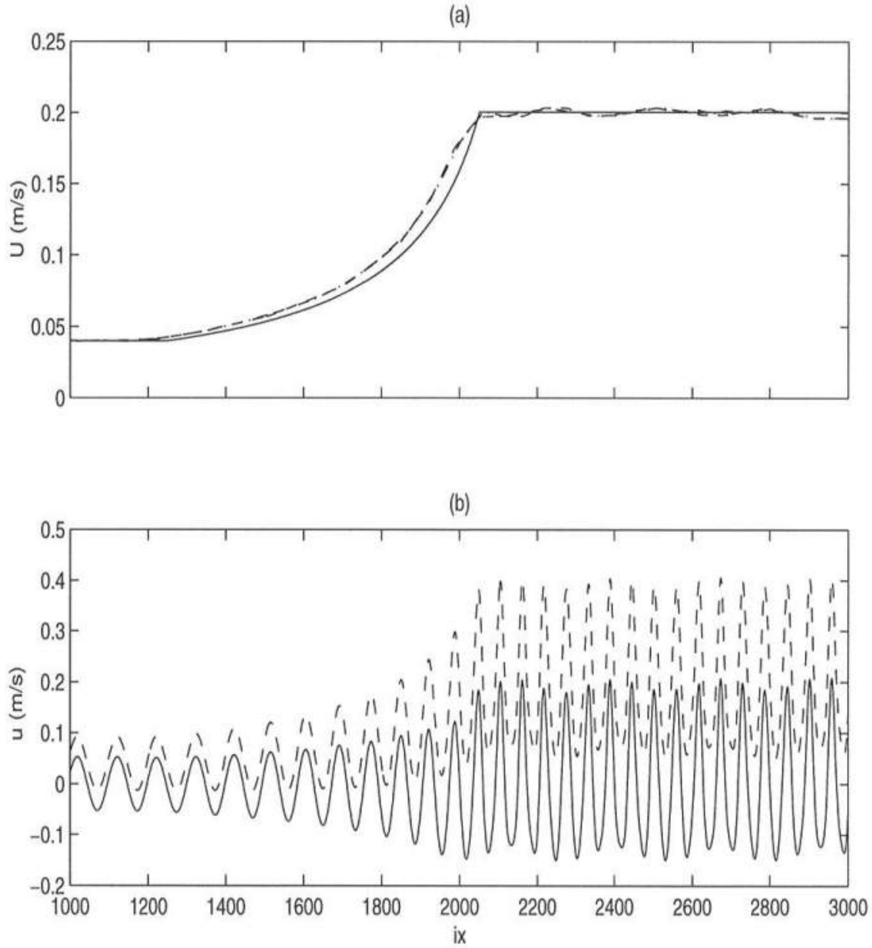

Figure 5.36: (a)Prescribed (-) and estimated (- -) current variation across the domain. (b)Total (- -) and pure wave part (-) of velocity data.

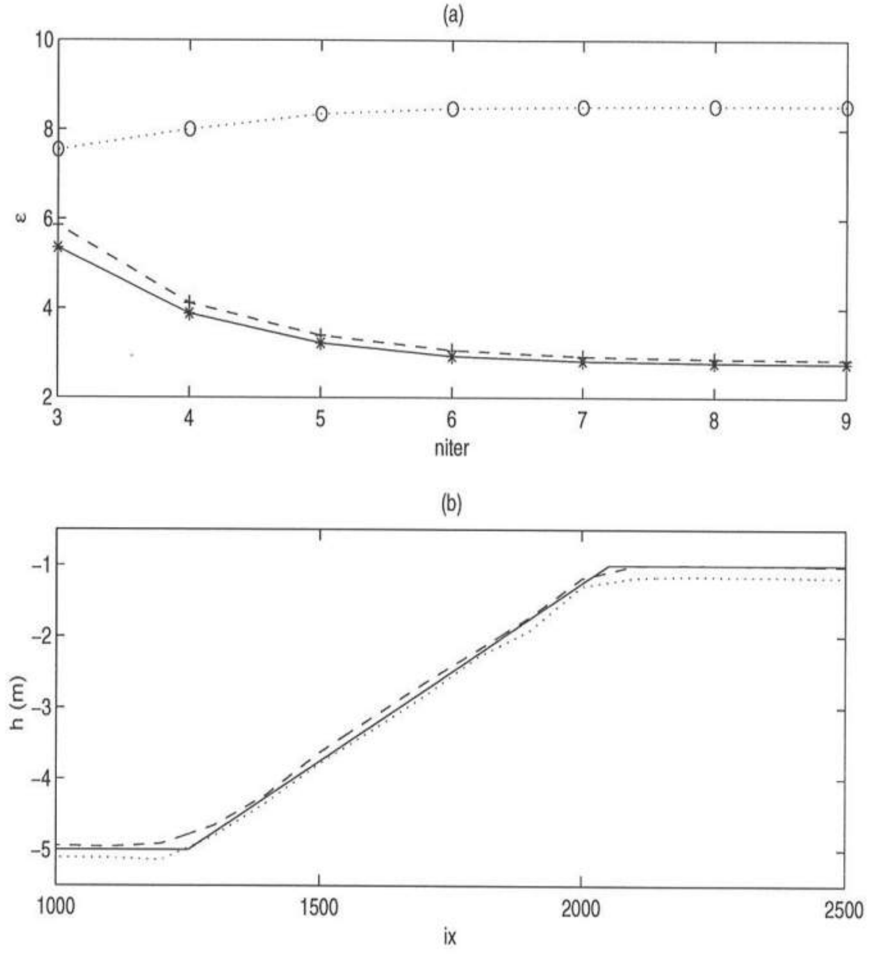

Figure 5.37: (a)Total surface elevation mismatch (ϵ) for inversion with u_t and C (o), u_w and C (+) and u_w and C_0 (*). (b)Actual (–) and estimated depths - Inverted depth with u_w and C (.), with u_w and C_0 (- -)

are compared to the actual depth in the bottom panel. By comparing this panel to the inverted depths obtained from uncorrected data in Figure 5.34, it can be seen that the modified algorithm makes remarkable improvements by accounting for mean flow effects and the inverted depth agrees with the true depth much better.

Figure 5.38 shows the estimated surface elevations from the mass (top panel) and momentum equations (bottom panel). The dotted line in each shows the result after inversion with the pure wave part of the velocity but Doppler shifted phase speed. The dashed line is the estimate with the corrected phase speed and the pure wave part of the velocity. The improvement in the surface elevation estimate by correcting for the phase speed can more clearly be seen in the shallower part of the depth (where the dashed line agrees much better with the solid line than the dotted line). With the existing modification in the inversion algorithm, mean flows can be accounted for only in monochromatic waves and weak currents.

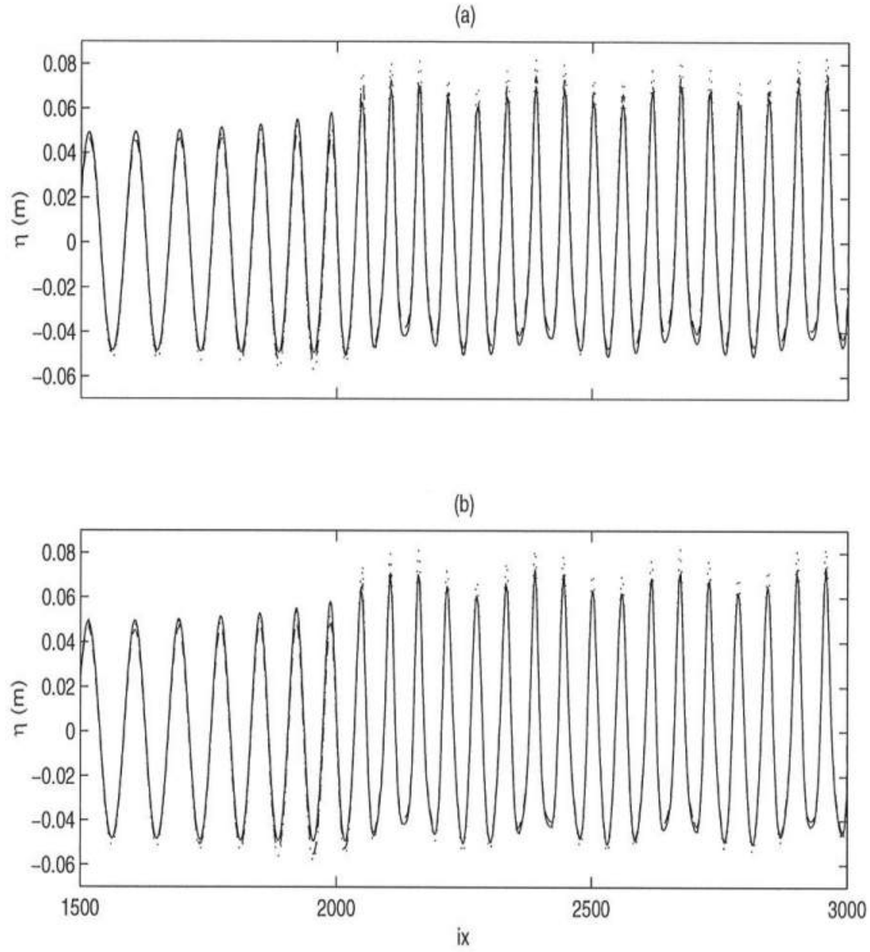

Figure 5.38: (a)Actual (–) and estimated surface elevation from mass equation - With u_w and C (.), with u_w and C_0 (- -). (b)Actual (–) and estimated surface elevation from the momentum equation - With u_w and C (.), with u_w and C_0 (- -)

Chapter 6

CONCLUSIONS AND FUTURE WORK

6.1 Conclusions

A depth inversion algorithm has been developed for one horizontal dimension and non-breaking waves. The inversion input data is assumed to be in the form of time lagged spatial maps of either surface elevation or particle velocity. Cross-correlation methods to estimate local phase speeds from the time lagged images, gives large errors for monochromatic wave conditions. They can be applied with increased and reasonable accuracy to irregular waves, when the errors are seen to cancel out due to superposition from the various individual wave components. Hilbert transforms, as another alternative to estimate phase speeds from such input data, can only be used for strictly periodic waves. It is thus not a very practical tool for evaluating phase speeds in random sea states. A least squares method has been developed to compute local phase speeds from time lagged spatial variations of either surface elevation or particle velocity. This method can be applied accurately to various wave conditions and the errors in the phase speed estimate are uniformly small compared to the cross-correlation estimates.

The inverted depths agree well with the actual depth used to generate the images. The depths studied here were analytically generated and were representative of monotonic beach slopes. Barred beaches were also constructed with realistic bar amplitudes, and the inverted depths agreed well with the analytic depths. In addition to estimating the bathymetry, the inversion algorithm can also compute particle kinematics, i.e, given surface elevation data, particle velocities can be calculated, and vice versa.

Linearized as well as fully nonlinear inversion equations were developed to take into account the nonlinear effects of wave propagation close to the coast. Mean flow effects due to weak currents have been included by modifying the inversion equations. The inversion for this case can only be done with velocity data. The resulting inverted depths and surface elevation estimates show remarkable improvements over the original formulation.

For groupy wave conditions, when inversion is done with a single pair of images, the computed phase speed, depth and particle kinematics show deviation from the true values, especially in the deeper part of the depth. The errors are related to the groupiness of the input data, and depend on the time instant at which the surface image was recorded. These errors can be minimized by averaging over randomly distributed (in time) images, with increased averaging leading to a decrease in the absolute errors.

6.2 Scope for future work

6.2.1 Including effects of strong currents

In the modifications to account for mean flow effects in the present inversion method, it was assumed that currents were weak in magnitude, so that mean water level changes could be neglected. The currents were also depth uniform and time invariant. Due to wave breaking, strong currents such as rip currents are often seen near the shore and which play their own role in modifying the bathymetry as well as the wave kinematics. Wave current interactions is an important nonlinear coastal phenomenon. To correctly estimate the bathymetry in such conditions, it is necessary to make further modifications to include the presence of strong currents.

It is to be noted that in its present form, the modified inversion method can only work for monochromatic wave conditions.

6.2.2 Including effects of wave breaking

Wave breaking is a common phenomenon close to the coast. Waves entering shallow water shoal and finally break due to the increasing wave height, dissipating a large portion of the wave energy and momentum, which while modifying the wave train, also affects the bathymetry. To accurately predict the depth in such a dynamically complex region, wave breaking has to be accounted for in any inversion method. The present method would work well to the point of wave breaking, since the inversion equations are fully nonlinear and can handle wave shoaling and other nonlinear interactions. Also, since no time history of the wave is available as input data to the inversion, wave breaking possibly has to be included by relating local changes in wave slope at breaking to momentum and energy dissipation. The inversion equations have to be conserving mass and momentum with wave breaking to accurately predict underlying depths.

6.2.3 Extension to two horizontal dimensions

Due to wave refraction, diffraction and other two dimensional effects of a changing bathymetry, the wave field near the shore is hardly ever purely one dimensional. There are situations however, where a principal direction of travel can be identified, and the wave field can be resolved along that dominant direction of travel, assuming that the variation perpendicular to that direction is weak or negligible. Since the present inversion method has been developed in only one horizontal dimension, further work needs to be done to extend it to both the horizontal coordinates. Most practical applications of depth inversion to changing nearshore bathymetries would require this extension. It is to be noted that the present assumption of data availability would also have to be extended. Among the three variables - surface elevation (as a function of both horizontal coordinates) and particle velocities along both horizontal coordinates, two would have to be available as input data. Local phase speeds can be calculated over the entire two dimensional domain using cross-correlation or least squares methods to spatial maps of surface elevation, but the determination of depth would require two of the three variables.

6.2.4 Validation with field data

The inversion methodology developed here assumes that time lagged, spatially dense yet discrete profiles of either surface elevation (half of the wave height) or particle velocity be available as input data. In this thesis, synthetic input data has been generated from a time dependent Boussinesq model. The inversion was also performed with the corresponding inversion equations, for e.g, when linearized time dependent equations in FUNWAVE were used to generate the images, linearized inversion equations were used to estimate depth and the particle kinematics. Remotely sensed data in physical variables such as wave height or particle velocity is as yet scarce in literature. The inversion algorithm has to be tested with field data either obtained from radar units or digital video cameras. At present, the possibility of translating either radar or optical backscatter to physical units of surface elevation and particle velocity is still very much incomplete. Ongoing research however seems promising enough to be capable of delivering data of the kind needed to perform inversions with the present method. The possibility of using time exposures of digital video data is at present being investigated in the Centre for Applied and Coastal Research.

Bibliography

Bell, P. S. (1999). Shallow water bathymetry derived from an analysis of X-band marine radar images of waves. *Coastal Engineering*, **37**, 513–527.

Chen, Q., Kirby, J. T., Dalrymple, R. A., Kennedy, A. B., and Chawla, A. (2000). Boussinesq modeling of wave transformation, breaking and runup.II: Two horizontal dimensions. *Journal of Waterway, Port, Coastal and Ocean Engineering*, **126**. In press.

Dalrymple, R. A., Kennedy, A. B., Kirby, J. T., and Chen, Q. (1998). Determining bathymetry from remotely sensed images. In *26th International Conference on Coastal Engineering*, pages 2395–2408, Copenhagen.

Dugan, J. P., Suzukawa, H. H., Forsyth, C. P., and Farber, M. S. (1996). Ocean wave dispersion surface measured with airborne IR imaging system. In *Proc. 1995 International Geoscience and Remote Sensing Symposium (IGARSS'95)*, pages 1282–1283, Florence, Italy.

Fuchs, R. A. (1953). Depth determination on beaches by wave velocity methods. Technical report, University of California, Berkeley.

Grilli, S. T. (1998). Depth inversion in shallow water based on nonlinear properties of shoaling periodic waves. *Coastal Engineering*, **35**, 185–209.

Kennedy, A. B., Dalrymple, R. A., Kirby, J. T., and Chen, Q. (1999). Determination of inverse depths using direct Boussinesq modeling. *Journal of Waterway, Port, Coastal and Ocean Engineering*. In press.

Kennedy, A. B., Chen, Q., Kirby, J. T., and Dalrymple, R. A. (2000). Boussinesq modeling of wave transformation, breaking and runup. I. One dimension. *Journal of Waterway, Port, Coastal and Ocean Engineering*, **126**.

Lippmann, T. C. and Holman, R. A. (1991). Phase speed and angle of breaking waves measured with video techniques. *Coastal Sediments*, pages 542–556. Edited by N. Kraus.

Madsen, P. A. and Sørensen, O. S. (1992). A new form of Boussinesq equations with improved linear dispersion characteristics. Part 2 A slowly varying bathymetry. *Coastal Engineering*, **18**, 183–204.

Madsen, P. A., Murray, R., and Sørensen, O. R. (1991). A new form of Boussinesq equations with improved linear dispersion characteristics. *Coastal Engineering*, **15**, 371–388.

Nwogu, O. (1993). An alternative form of the Boussinesq equations for nearshore wave propagation. *J. Waterway, Port, Coastal and Ocean Engineering*, **119**(6), 618–638.

Stockdon, H. F. (1998). *Estimation of wave phase speed and nearshore bathymetry using video techniques*. Master's thesis, Oregon State University.

Thornton, E. B. and Guza, R. T. (1982). Energy saturation and phase speeds measured on a natural beach. *J. Geophysical Research*, **87**(C12), 9499–9508.

Ursell, F. (1953). The long wave paradox in the theory of gravity waves. *Proc. Cambridge Phil. Soc.*, **49**, 685–694.

Wei, G., Kirby, J. T., Grilli, S. T., and Subramanya, S. (1995). A fully nonlinear Boussinesq model for surface waves. I Highly nonlinear unsteady waves. *Journal of Fluid Mechanics*, **294**, 71–92.